

# Northumbria Research Link

Citation: Li, Xue, Ren, Jianning, Sridhar, Deepak, Xu, Bin, Algadi, Hassan, El-Bahy, Zeinhom M., Ma, Yong, Li, Tingxi and Guo, Zhanhu (2023) Progress of layered double hydroxide-based materials for supercapacitors. *Materials Chemistry Frontiers*, 7 (8). pp. 1520-1561. ISSN 2052-1537

Published by: Royal Society of Chemistry

URL: <https://doi.org/10.1039/D2QM01346K> <<https://doi.org/10.1039/D2QM01346K>>

This version was downloaded from Northumbria Research Link:  
<https://nrl.northumbria.ac.uk/id/eprint/51217/>

Northumbria University has developed Northumbria Research Link (NRL) to enable users to access the University's research output. Copyright © and moral rights for items on NRL are retained by the individual author(s) and/or other copyright owners. Single copies of full items can be reproduced, displayed or performed, and given to third parties in any format or medium for personal research or study, educational, or not-for-profit purposes without prior permission or charge, provided the authors, title and full bibliographic details are given, as well as a hyperlink and/or URL to the original metadata page. The content must not be changed in any way. Full items must not be sold commercially in any format or medium without formal permission of the copyright holder. The full policy is available online: <http://nrl.northumbria.ac.uk/policies.html>

This document may differ from the final, published version of the research and has been made available online in accordance with publisher policies. To read and/or cite from the published version of the research, please visit the publisher's website (a subscription may be required.)



**Northumbria  
University**  
NEWCASTLE



**UniversityLibrary**

# Progress of layered double hydroxides-based materials for supercapacitors

Xue Li<sup>1</sup>, Jianning Ren<sup>1</sup>, Deepak Sridhar<sup>2</sup>, Ben Bin Xu<sup>3</sup>, Hassan Algadi<sup>4,5</sup>,

Zeinhom M. El-Bahy<sup>7</sup>, Yong Ma<sup>1,\*</sup>, Tingxi Li<sup>1,\*</sup>, Zhanhu Guo<sup>6,\*</sup>

<sup>1</sup> School of Material Science and Engineering, Shandong University of Science and Technology,  
Qingdao 266590, China

<sup>2</sup> Zentek Ltd. 24 Corporate Crt, Guelph, Ontario, N1G 5G5 Canada

<sup>3</sup> Mechanical and Construction Engineering, Faculty of Engineering and Environment,  
Northumbria University, Newcastle Upon Tyne, NE1 8ST, UK

<sup>4</sup> Department of Electrical Engineering, Faculty of Engineering, Najran University, Najran,  
11001, Saudi Arabia

<sup>5</sup> College of Materials Science and Engineering, Taiyuan University of Science and Technology,  
Taiyuan, 030024, China

<sup>6</sup> Integrated Composites Laboratory (ICL), Mechanical and Construction Engineering, Faculty of  
Engineering and Environment, Northumbria University, Newcastle Upon Tyne, NE1 8ST, UK

<sup>7</sup> Department of Chemistry, Faculty of Science, Al-Azhar University, Nasr City 11884, Cairo,  
Egypt ([zeinelbahy@azhar.edu.eg](mailto:zeinelbahy@azhar.edu.eg))

\*Correspondence author: E-mail: mayong@sdust.edu.cn (Yong Ma), litx@sdust.edu.cn (Tingxi  
Li), nanomaterials2000@gmail.com (Zhanhu Guo)

## **Abstract**

Nowadays, supercapacitors have been received widespread interests because of large specific capacitance, excellent cycle life, high power density and energy density, and wide operating temperature range. Electrode materials as an important component of supercapacitors directly decide the electrochemical performances. Layered double hydroxides (LDHs) are emerging in the field of electrode materials because of their unique 2D layer morphology, simple preparation method, large specific surface area and high theoretical specific capacitance. In this paper, the methods for the preparation of LDHs in recent years are reviewed, while different methods resulting in different properties are presented. In addition, some recent methods for the modification of LDHs are demonstrated, from content composition to structural changes giving rise to different properties. Furthermore, various types of LDHs used for supercapacitors are presented, the electrochemical performances are displayed, and their energy storage mechanism are meanwhile illuminated in detail. This article aims to elucidate the usage of LDHs for supercapacitors, as well as hopes to provide a reference for the further research based on these promising materials.

**Keywords:** Layered double hydroxides; Preparation methods; Modification methods; Electrode materials; Supercapacitor.

## 1 Introduction

With the development of society, the use of non-renewable fossil fuels such as coal, oil and natural gas are increasing, leading to more and more serious environmental pollution.<sup>1</sup> The development of new energy can effectively solve this problem.<sup>2</sup> Therefore, scientists have devoted themselves to the field of new energy, which is also a research hotspot today. Green renewable energy, mainly including solar energy,<sup>3</sup> tidal energy,<sup>4</sup> wind energy<sup>5, 6</sup> and hydrogen energy,<sup>7, 8</sup> etc., has the advantages of being sustainable, renewable<sup>9</sup> and easy to obtain. It has shown broad prospects in replacing one-time energy and has been developed rapidly.<sup>10-12</sup> However, these energy sources are unstable and have contingency and other shortcomings that limit their large-scale practical applications. For example, solar energy cannot work at night, and wind energy is affected by wind speed and is intermittent. Therefore, in the search for clean, efficient and renewable energy sources,<sup>13</sup> the development of energy conversion and storage must also keep in pace. The need to provide high-capacity and portable power supplies<sup>14-16</sup> for various technological products and equipment has attracted widespread attention, and for the above reasons, supercapacitors have emerged as the times require.<sup>17</sup>

So far, supercapacitors have been developed for more than forty years since their birth, but the history of development in China is only about twenty years.<sup>18</sup> At the beginning, supercapacitors are only applied to small devices like tape recorders and water heaters,<sup>19, 20</sup> but with the development of technology, supercapacitors can be applied to large devices such as tanks and electric starting systems of cars,<sup>21</sup> and their role has been increasingly highlighted. It can be

predicted that supercapacitors have great development and application potential in the future development of society,<sup>22-25</sup> therefore, the current research of supercapacitors attracts researchers in various fields.<sup>26-28</sup> Supercapacitors, as a type of energy storage device between traditional capacitor and rechargeable battery, have the characteristics of fast charging and discharging of capacitor and energy storage of battery at the same time.<sup>29, 30</sup> Because of non-pollution to the environment, long cycle life,<sup>31, 32</sup> high power density<sup>33</sup> and high safety,<sup>34-36</sup> they have received more and more attention from scientific researchers. At present, people are optimistic about supercapacitors and expect that they can provide services for more aspects of human life in the future.<sup>37-39</sup> The supercapacitor is mainly composed of several parts including current collector, electrode, electrolyte and diaphragm, where the diaphragm plays a role in separating the two electrodes, preventing a short circuit between the electrodes, and allowing ions to pass through.<sup>40-</sup>

<sup>43</sup> Electrolytes are homogeneous mixtures of acids, alkaline or salts with specific solvents and can be mainly classified as liquid electrolytes and solid electrolytes. Among them, solid electrolytes can be divided into all-solid electrolytes and quasi-solid electrolytes.<sup>44, 45</sup> The latter, also called gel-polyelectrolyte, consists of a polymer network dissolved in a solvent containing active ions, It has both high transport properties similar to liquid electrolytes and mechanical stability like solid electrolytes, which is essential for enhancing the flexibility, stretchability and temperature resistance of supercapacitors. During charging and discharging, the ions migrating at the interface originate from the electrolyte.<sup>46, 47</sup> Jin et al. obtained polyaniline by *in situ* growth on an organic hydrogel polymer electrolyte and acquired a low-temperature resistant, externally stretched

supercapacitor with excellent rate performance and cycling performance at  $-30\text{ }^{\circ}\text{C}$ .<sup>48</sup> In addition, they developed an aqueous phase freeze-proof and heat-resistant symmetric micro-supercapacitor with a 2.3 V voltage window, using an aqueous polyacrylamide polyelectrolytes and carbon nanotube electrodes, which has good cycling stability in both high and low temperature environments.<sup>49</sup> Not coincidentally, Song et al. developed high-performance carbon nanotubes-MnO<sub>2</sub> microelectrodes and excellent temperature-resistant aqueous polyacrylamide polyelectrolytes. The device reached a voltage window of 2 V at temperatures ranging from  $-15\text{ }^{\circ}\text{C}$  to  $100\text{ }^{\circ}\text{C}$  and had good cyclic stability.<sup>50</sup>

Due to the difference in energy storage mechanism, supercapacitors can be divided into double layer supercapacitors,<sup>51, 52</sup> Faraday pseudo supercapacitors and hybrid supercapacitors.<sup>53, 54</sup> Fig. 1 shows the Schematic diagram of storage mechanism and corresponding electrochemical characteristics of several capacitors. The electric double layer capacitor uses the electric double layer between the electrolyte and the electrode to store the charges.<sup>55</sup> In the working process, no charge transfer occurs between the electrode and the electrolyte.<sup>56</sup> The stored charge is a physical adsorption process without redox reaction. Carbon materials are mostly used as materials.<sup>57</sup> Faraday pseudo supercapacitors are electrochemically active substances that undergo rapid and reversible chemical adsorption or desorption on electrodes and electrochemical redox reactions for charge storage.<sup>58, 59</sup> The transfer of electrons in the energy storage process causes a change in the valence state of an element in the electrode material,<sup>60</sup> which is commonly used in conducting polymers,<sup>61-63</sup> metal oxides,<sup>64-66</sup> etc. Hybrid supercapacitors generally have both mechanisms,<sup>67, 68</sup>

but the proportion of double layer capacitance and Faraday pseudo capacitance in supercapacitors is different.<sup>69</sup> Hybrid supercapacitors can be divided into asymmetric supercapacitors and symmetric supercapacitors. The two electrodes of the asymmetric supercapacitor are different materials, which can make full use of the different voltage windows to maximize the operating voltage of the whole device to the extent of providing higher energy density. However, issues such as matching the capacitance of the two electrodes need to be considered. The two electrodes of symmetrical supercapacitors are the same material, which requires less consideration, and they are easy to assemble and less costly. The poor thing is that it can only rely on the conductivity of the electrode material and its own structure to provide electrochemical performances, so its usage performances is somewhat limited.

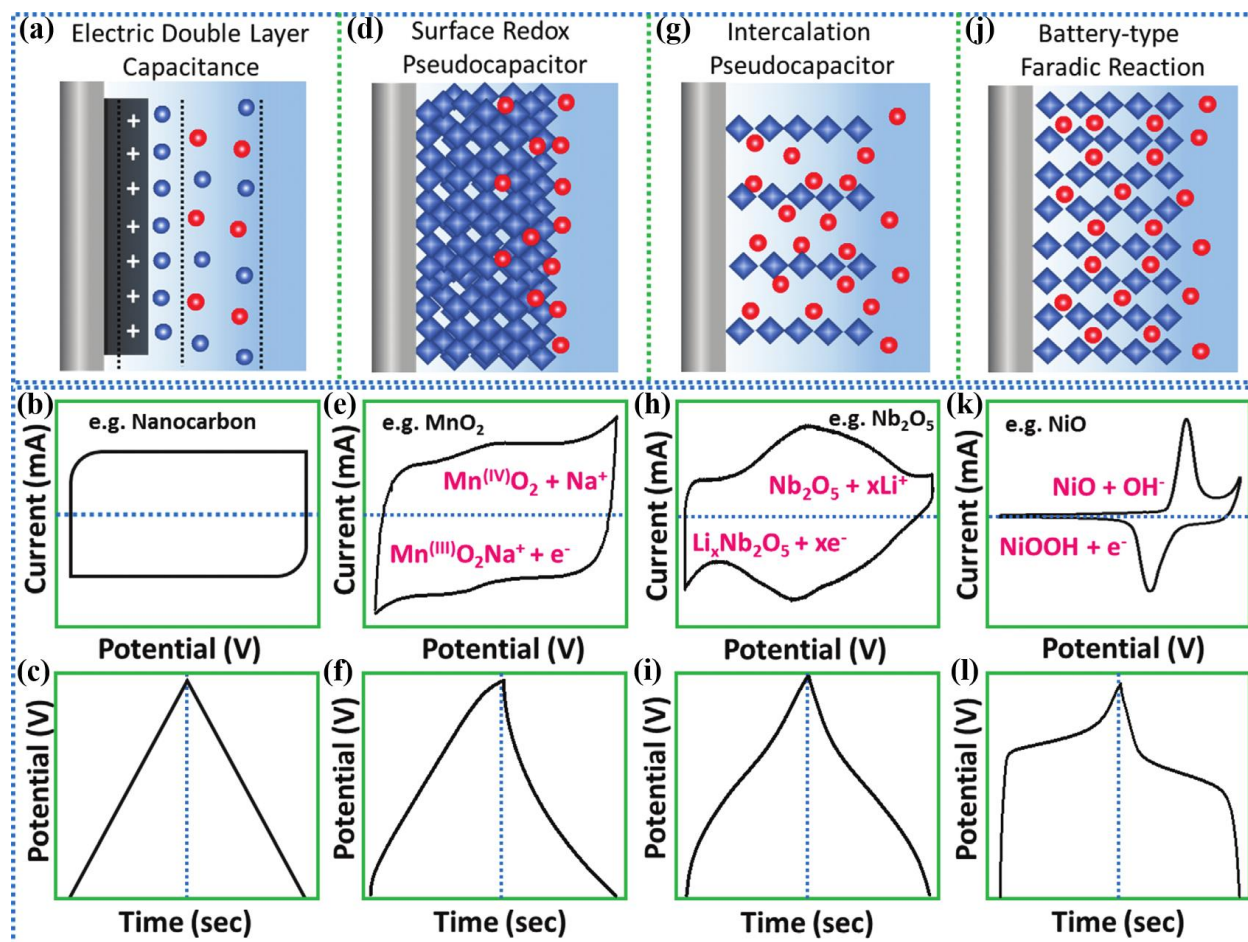


**Fig. 1** Schematic diagram of storage mechanism and corresponding electrochemical characteristics of several capacitors (representative shapes of CV and GCD curves): (a-c) electrical double layer capacitance, (d-f) surface redox pseudocapacitance, (g-i) intercalated pseudocapacitance, (j-l) battery-type.<sup>70</sup>

Copyright 2020 Wiley-VCH GmbH.

As the reaction proceeds, the electrode material undergoes a series of structural changes due to its own involvement in the reaction.<sup>71, 72</sup> Problems such as corrosion of the electrode surface and shrinkage of the material volume can lead to a serious degradation of the electrode material performances.<sup>73-75</sup> Most of the problems in supercapacitors can be attributed to the presence of significant material defects that prevent the electrochemical reaction.<sup>76</sup> Currently, the energy



storage devices with low energy density cannot meet the demand in many applications, limiting their commercial applications.<sup>77</sup> The energy density can be increased through designing and fabricating electrode materials.<sup>78-81</sup>

2D layered double hydroxides (LDHs)<sup>82, 83</sup> have a high specific surface area and abundant ion insertion sites and have received focus because of high theoretical specific capacitance,<sup>84-88</sup> showing good prospects for applications in supercapacitors. There are mainly metal cations ( $M^{2+}$ ,  $M^{3+}$ ) and interlayer anions ( $A^{n-}$ ) and solvent molecules ( $H_2O$ ) in the hydroxide layer. Metal cations are located in the center and hydroxide ions are six-coordinated through chemical bonds to form an octahedron to form the main layer of the layered structure<sup>89, 90</sup>, anions are filled in the interlayer gaps to balance charges, and solvent molecules fill the remaining gaps.<sup>91</sup> It can usually be expressed by the following chemical general formula:  $[M_{1-x}^{2+}M_x^{3+}(OH)_2]^{x+}[A^{n-}]_{x/n} \cdot zH_2O$ .  $M^{2+}$  ( $Fe^{2+}$ ,  $Ni^{2+}$ ,  $Zn^{2+}$ ,  $Mn^{2+}$ ,  $Co^{2+}$  and  $Mg^{2+}$ ) are the +2 valence cations in the main layer structure.  $M^{3+}$  ( $Co^{3+}$ ,  $Al^{3+}$ ,  $Fe^{3+}$ ,  $Mn^{3+}$ ,  $Cr^{3+}$  and  $Ga^{3+}$  etc.) are the +3 valence cations alternating with  $M^{2+}$ , and two metal cations are arranged alternately in the main layer in the laminar structure in addition to the more special monovalent  $Li^+$  and tetravalent  $Ti^{4+}$  ions can also constitute the LDH of the laminar structure.  $A^{n-}$  denotes the interlayer anions, mainly  $NO_3^-$ ,  $CO_3^{2-}$ ,  $SO_4^{2-}$  and  $Cl^-$ , etc. <sup>92</sup> In recent years, researchers have improved the level of research on LDHs and found that some +1-valent and +2-valent cations can exist in the molecule, and this discovery makes the structural composition of layered bimetallic hydroxides more complex and variable. The changes that can be brought about based on its structure are also more varied.<sup>93-95</sup> Fig. 2 shows the carbonate-

intercalated LDHs in various  $M^{2+}/M^{3+}$  molar ratios, declaring that the metal hydroxide octahedra stacks along the crystallographic c-axis. Due to the unique layer structure of LDHs, the composition and ratio of their metal cations can be adjusted, the type and number of interlayer anions can be controlled, and the number of layers and layer spacing can be easily changed, making them easy to be compounded with other materials to realize functionalization, etc.<sup>96-98</sup>

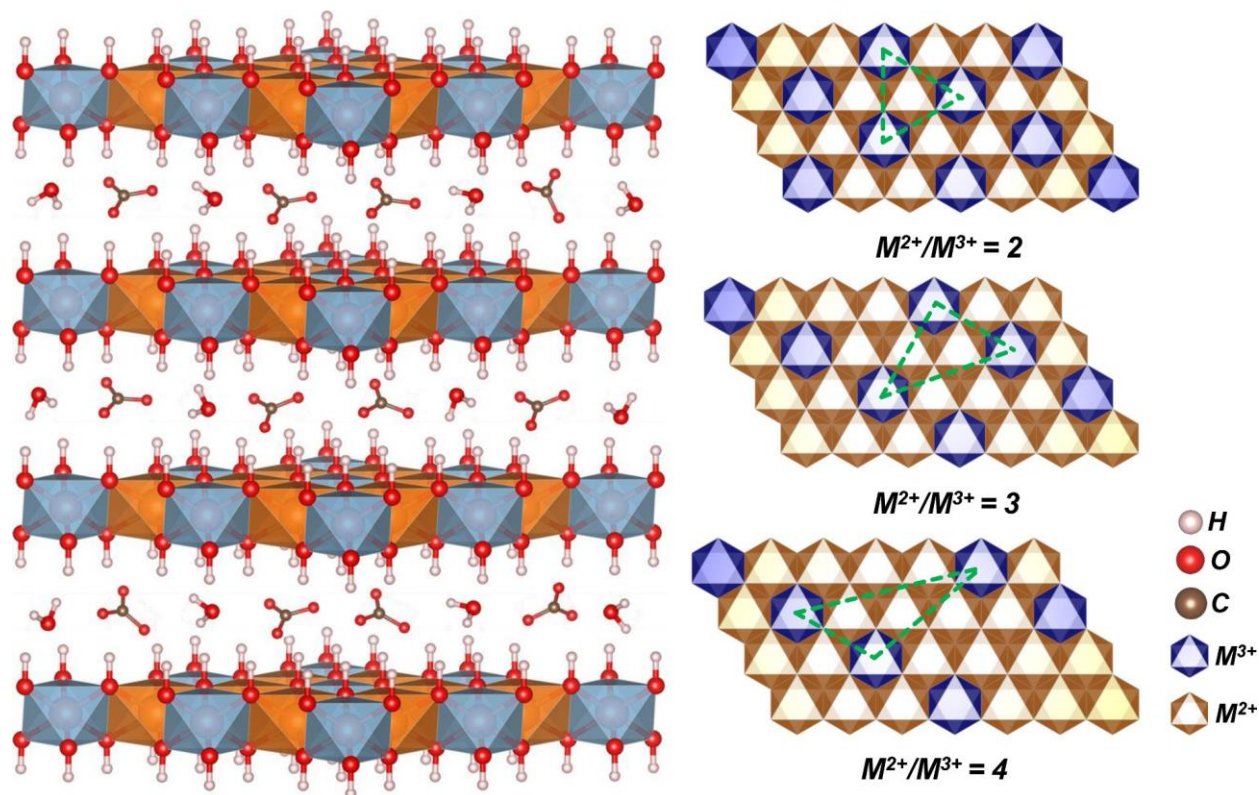


**Fig. 2** The idealized structure of carbonate-intercalated LDHs with different  $M^{2+}/M^{3+}$  molar ratios showing the metal hydroxide octahedra stacked along the crystallographic c-axis.<sup>99</sup> Copyright 2020, Zhengzhou University.

Pristine LDHs are also considered superior supercapacitor electrodes, thanks to their layered structure and adjustable interlayer spacing, providing large specific surface area and adequate ion

transport rates.<sup>100-102</sup> However, pristine LDHs suffer from severe refilling, which can reduce their overall exposed surface area and make electrolyte ion transport difficult.<sup>103-105</sup> Besides, the poor conductivity can affect transfer of electron and full utilization of active sites.<sup>106-108</sup> The ultrathin nanosheet structure of LDHs usually leads to rapid structural deterioration under harsh electrochemical conditions, which eventually affects the usage performance.<sup>109</sup> To overcome these limitations, hybridized LDHs-based nanostructures have been developed as potentially multifunctional nanomaterials, and the fabrication of these materials with large specific surface area and more active sites is the key to improve their electrical conductivity and multiplicative properties.<sup>110-113</sup> The use of LDHs materials as electrode materials for supercapacitors is mainly based on their special lamellar-pore structure, which can provide the large specific surface area and a large number of reactive sites required for supercapacitors. It has gradually developed into a new generation of environmentally friendly and efficient electrochemical functional materials.

Chen et al.<sup>114</sup> provided a systematic review of the synthesis methods of 2D LDH materials, focusing on the characteristics possessed by different synthesis methods. A comprehensive review of the properties and synthesis methods of LDHs, carbon nanomaterials and composite nanomaterials is presented by Khorshidi et al.<sup>115</sup> Kim et al.<sup>116</sup> reviewed the standard synthesis methods for LDHs, analyzed the design and improvement of typical exemplary LDHs and LDH composites, and focused on the performance of LDHs-based sensors for key biomarkers and contaminants, including glucose and metal ions. However, the systematic introduction of LDH material preparation and modification methods, as well as the application in the field of

supercapacitors are rarely reviewed. Herein, this paper focus on the preparation of heterogeneous LDHs including co-precipitation, hydrothermal and solvothermal methods, electrodeposition and some other methods, as well as the modification of heterogeneous LDHs including the addition of components, the construction of defects and the generation of heterostructures.<sup>19, 24, 54, 117, 118</sup> The prospects of the usage of LDHs for supercapacitors are foreseen, as well as it is hoped that they will provide assistance for the later research of this material.

## **2. Preparation methods**

There are various methods for the synthesis of pristine LDHs nanostructures, while the synthesis of hybrid LDHs is often more complex than that of pristine LDHs, usually requiring two or more steps to synthesize them. In this chapter, a variety of methods for the synthesis of LDHs nanostructures are reviewed, including co-precipitation, hydrothermal and solvothermal methods, electrodeposition, electrostatic interlayer interaction and some other methods. Different methods require different conditions, and the structure and the morphology of the synthesized materials also differ, but ultimately, they all aim to synthesize materials with better properties.<sup>119</sup>

### **2.1 Co-precipitation method**

Co-precipitation method is one of the most common preparation methods for LDHs, which mainly involves adding mixed salt solution and mixed base solution dropwise to distilled water at a certain temperature at a certain rate, then accelerating the reaction by stirring, and finally filtering and drying to obtain LDHs with uniform size and regular structure. Since strong alkali solutions cause rapid precipitation of metal ions and make it difficult to regulate and control the reaction

process, a certain concentration of sodium hydroxide and sodium carbonate is often formulated into a mixed alkali solution as a precipitant.<sup>120-123</sup> This method has been widely used in practice because of its simplicity, cheapness and stability of the product. However, the addition of precipitating agent during the preparation process may cause local concentration too high and lead to agglomeration of product. Selecting suitable precipitant, controlling the addition method of precipitant and reasonably controlling the reaction time in the synthesis process are beneficial to the LDHs materials with excellent performances. Wen et al.<sup>124</sup> prepared  $\text{Zn}_6\text{Al}_2(\text{OH})_{16}\text{CO}_3 \cdot 4\text{H}_2\text{O}$  LDH by co-precipitation method using NaOH and  $\text{Na}_2\text{CO}_3$  as the base alkaline sources. The obtained samples were nanosheet powders with a thickness of about 80 nm. Its specific capacitance was  $37.0 \text{ F g}^{-1}$  at  $1.0 \text{ A g}^{-1}$ . Besides, Wiston et al.<sup>125</sup> used a co-precipitation method to couple two highly electroactive metal ions together to form a nanoflower-like array in the presence of urea. The synthesis schematic is shown in Fig. 3 (a). At  $1 \text{ A g}^{-1}$ , the obtained NiFe-LDH has a specific capacitance of  $381 \text{ C g}^{-1}$  ( $1368 \text{ F g}^{-1}$ ) and retains 87.5% after 5000 consecutive cycles (Fig. 3 (b)). At a power density of  $1483 \text{ W kg}^{-1}$ , the prepared symmetric supercapacitor has an energy density of  $66.13 \text{ Wh kg}^{-1}$ , showing excellent application prospects.

Pure LDHs have poor electrical conductivity and structural instability. The introduction of other anions during the synthesis process can facilitate better performance. Xiao et al.<sup>126</sup> prepared NiCo-LDH/ $\text{CO}_3\text{-x}$  by a facile chemical co-precipitation method, and the flow chart is shown in Fig. 3 (c). The  $\text{CO}_3^{2-}$  was introduced into the LDH in a controlled manner by the addition of  $\text{NaHCO}_3$ . The doping of  $\text{CO}_3^{2-}$  can cause the original nanosheet structure to bend and interconnect,

increasing the contact between the electrolyte and the electrode. By analyzing TEM images of Fig. 3 (d) and (e), it is known that the carbonate-doped samples are more dispersed and the thickness of the nanosheets is smaller than that of the undoped samples. This case means that more active sites will be exposed to the electrolyte, enhancing the energy storage properties of the material and effectively increasing the specific capacitance. When the doping ratio of carbonate is 5% (Ni, Co-LDH/CO<sub>3</sub>-5%), 1970 F g<sup>-1</sup> specific capacitance realizes at 1 A g<sup>-1</sup> as well as still maintains 82.8% specific capacitance at 20 A g<sup>-1</sup>. At a power density of 374.9 W kg<sup>-1</sup>, the asymmetric supercapacitor assembled with NiCo-LDH/CO<sub>3</sub>-5% as the positive electrode has a energy density of 54.8 Wh kg<sup>-1</sup> and maintains 80.8% after 10000 cycles at 10 A g<sup>-1</sup>.

Inevitably, in a range of materials synthesized by co-precipitation, there will be instances of poor performances, in which the synthesized materials need to be further treated to achieve even better performance. Wang et al.<sup>127</sup> synthesized NiCo-LDHs and at 1 A g<sup>-1</sup> the specific capacitance was 285.8 C g<sup>-1</sup>, but the material has poor electrical conductivity and the obtained capacitance is lower than that of the theoretical value. Based on this, NiCo-LDHs were subsequently phosphorylated and P@NiCo-LDHs cabbage-like spheres were successfully synthesized, as shown in Fig. 3 (f). At 1 A g<sup>-1</sup>, its specific capacitance reached 536 C g<sup>-1</sup> due to the generation of metal phosphide having good electron conduction ability (Fig. 3 (g) and (h)). In addition, the prepared electrodes have good cycling performance, and at 10 A g<sup>-1</sup> the capacitance after 5000 cycles is almost constant. The prepared symmetric supercapacitor devices have 7.83 Wh kg<sup>-1</sup> energy density at 300 W kg<sup>-1</sup>, as well as has excellent cycle performance (Fig. 3 (i)), which



indicates that phosphorylation can be as an effective route to enhance the performance of LDH-based supercapacitor composites.

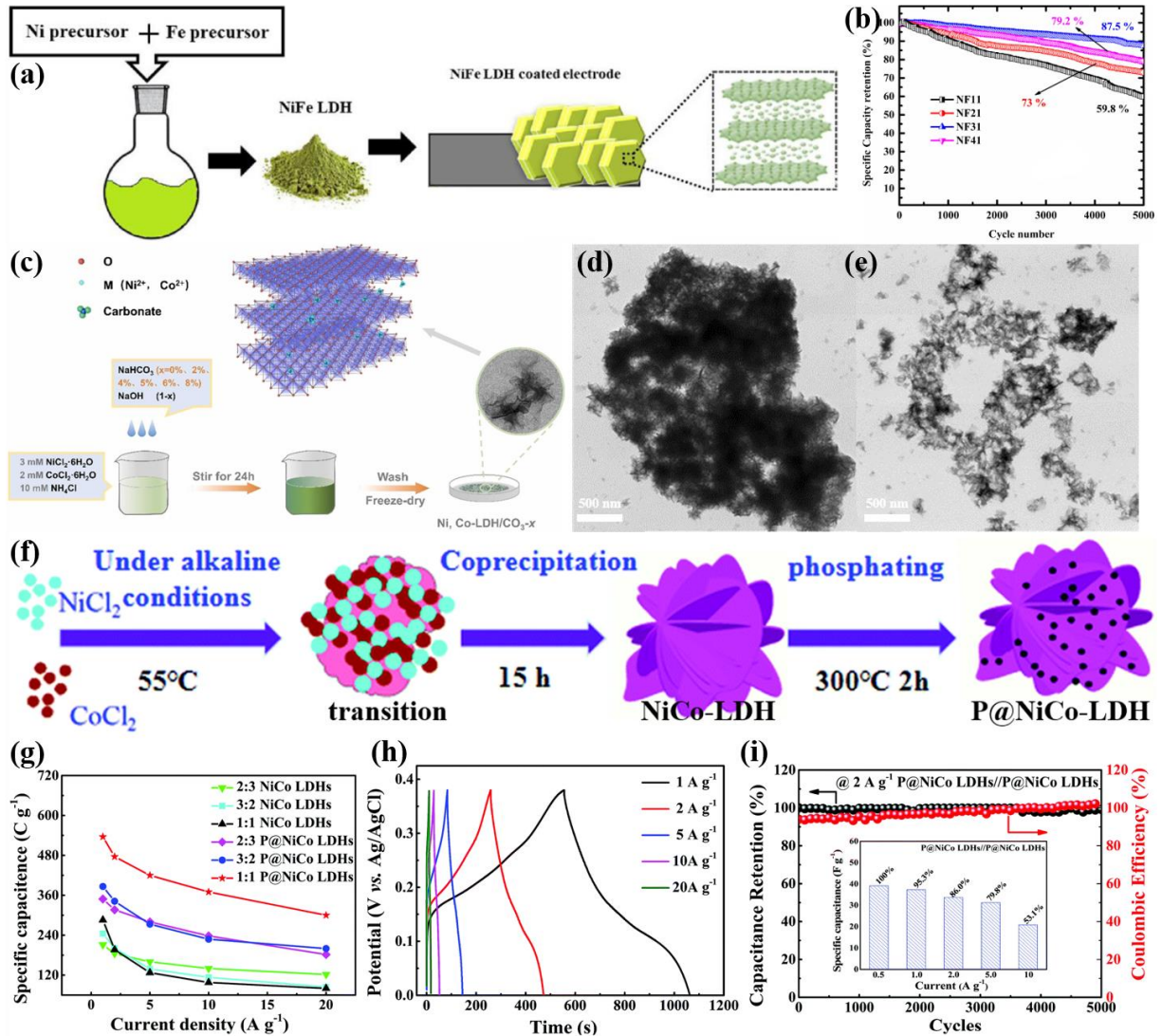


Fig. 3 (a) Schematic diagram of the synthesis of NiFe-LDH, (b) cycling stability of NF11, NF21, NF31 and NF41.<sup>125</sup> Copyright 2022, Elsevier Ltd. (c) low chart of Ni, Co-LDH/CO<sub>3-x</sub>, (d, e) TEM images of Ni, Co-LDH/CO<sub>3-x</sub> when (e) x = 0% and (f) x = 5%.<sup>126</sup> Copyright 2022, Elsevier B.V. (f) Schematic illustration of fabrication procedures for P@NiCo LDHs, (g) charge results of the 1:1 P@NiCo LDHs under various current specific capacitance of different obtained electrodes at various current densities, (h) GCD results

of the 1:1 P@NiCo LDHs under various current densities, (i) capacitance retention and coulombic efficiency at 2 A g<sup>-1</sup> and the specific capacitance of the device.<sup>127</sup> Copyright 2021, Royal Society of Chemistry.

The properties of materials are inextricably linked to factors such as structure, and variations in synthesis methods can affect the structure of materials, and therefore their properties.<sup>128</sup> Further modifications can be made to the material based on co-precipitation to give it superior properties. Li et al.<sup>129</sup> synthesized Zn<sub>0.25</sub>Ni<sub>0.75</sub>Co-LDH-BA<sup>-</sup> inserted with benzoate anion by zeolitic imidazolate framework-L (ZIF-L) assisted co-precipitation process, as displayed in Fig. 4 (a). The specific capacitance was 1378 mAh g<sup>-1</sup> at 1 A g<sup>-1</sup>, presenting good capacitance performance (Fig. 4 (b) and (c)). This electrode can maintain 91.2% value experiencing 10000 cycles at 10 A g<sup>-1</sup> (Fig. 4 (d)). The asymmetric supercapacitor has a high energy density of 51.8 Wh kg<sup>-1</sup> at a power density of 789 W kg<sup>-1</sup> and a 94.6% capacitance retention experiencing 10000 cycles. Wang et al.<sup>130</sup> prepared S-NiCoAl-LDH electrode materials by surface sulfidation. From TEM image in Fig. 4 (e), it could be found that S-NiCoAl-LDH exhibited tiny flake morphology and aggregated in micron size. It had a 727.1 C g<sup>-1</sup> specific capacitance at 1 A g<sup>-1</sup> and still reached 556 C g<sup>-1</sup> at 20 A g<sup>-1</sup> (Fig. 4 (f) and (g)). The surface sulfide enhances conductivity and improves multiplicative performance. The capacity retention rate was 95.1% after 10000 cycles (Fig. 4 (h)). The Al doping stabilizes the crystal form of S-NiCoAl-LDH and make it have high cycling performance. The assembled S-NiCoAl-LDH// AC device has a specific capacitance of 182.6 F g<sup>-1</sup> at 0.5 A g<sup>-1</sup> and a high energy density of 82.2 Wh kg<sup>-1</sup> at 450 W kg<sup>-1</sup>.



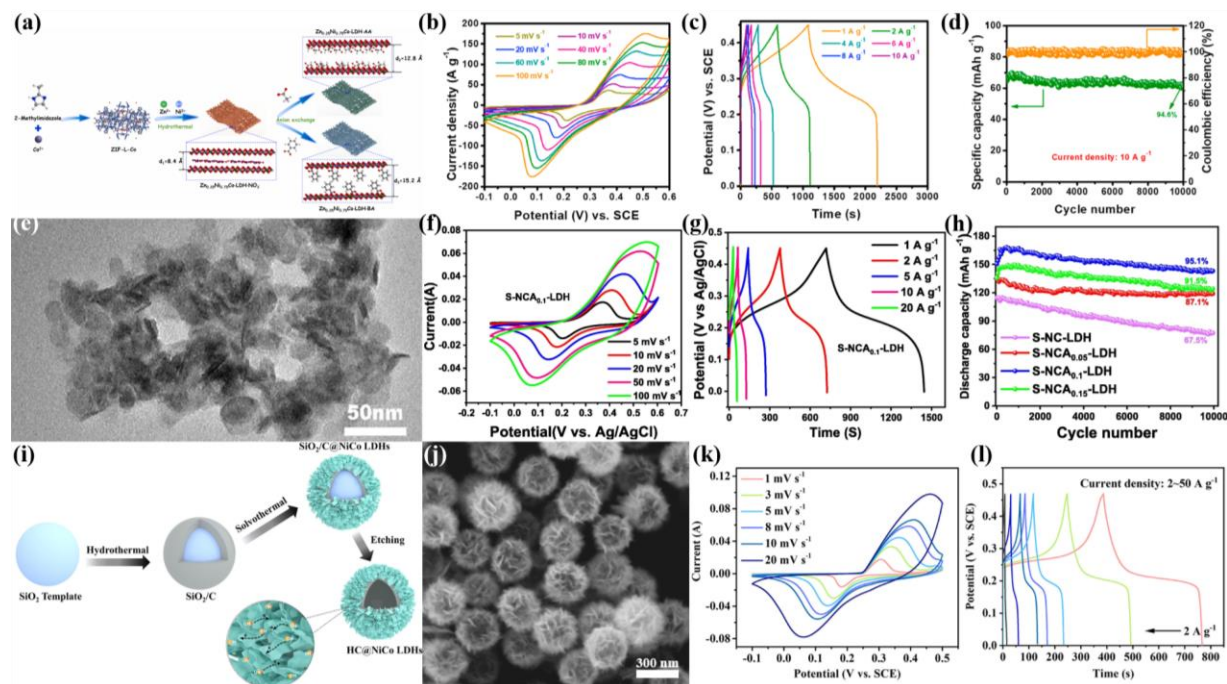


Fig. 4 (a) Schematic illustration of formation processes for  $\text{Zn}_{0.25}\text{Ni}_{0.75}\text{Co-LDH-BA}^-$ , (b) CV curves of  $\text{Zn}_{0.25}\text{Ni}_{0.75}\text{Co-LDH-BA}^-$  with the potential sweep rate varied from 5 to  $100 \text{ mV s}^{-1}$ , (c) fraction of the capacitive contribution of  $\text{Zn}_{0.25}\text{Ni}_{0.75}\text{Co-LDH-BA}^-/\text{AA}^-/\text{NO}_3^-$  at different scan rates, (d) cycling life property and coulombic efficiency of  $\text{Zn}_{0.25}\text{Ni}_{0.75}\text{Co-LDH-BA}^-$  at  $10 \text{ A g}^{-1}$ .<sup>129</sup> Copyright 2022 Elsevier B.V.

(e) TEM image of the S-NiCoAl<sub>0.1</sub>-LDH, (f, g) CV and GCD curves of the S-NiCoAl<sub>0.1</sub>-LDH at different scan rates and current densities, respectively, (h) cycling stability of after 10000 cycles at  $10 \text{ A g}^{-1}$ .<sup>130</sup> Copyright 2022 Elsevier Inc. (i) Diagram of the synthesis of HC@NiCo LDHs microspheres, (j) SEM image of HC@NiCo LDHs spheres, (k, l) CV and GCD curves of the optimized HC@NiCo LDHs (with the initial ratio of Ni/Co = 4:1) at different scan rates and current densities.<sup>131</sup> Copyright 2021 Elsevier Ltd.

The co-precipitation method also allows the synthesis of composites of LDHs with other materials, resulting in unique structures with excellent properties. The hydrangea-like HC@NiCo-

LDHs were prepared by applying a chemical co-precipitation without the addition of additional alkaline reagents.<sup>131</sup> The synthesis processes are shown in Fig. 4 (i). The high Ni concentration allows the less crystalline NiCo-LDHs to grow uniformly and contact closely on the hollow carbon shell, forming an embroidered spherical structure (Fig. 4 (j)). This unique structure and crystalline phase expose abundant active sites and promote diffusion of ions. At 2 A g<sup>-1</sup>, its specific capacitance was 758 C g<sup>-1</sup>, and the capacity retention was 79% at 20 A g<sup>-1</sup>, demonstrating good multiplicative properties (Fig. 4 (k, l)). The assembled HC@NiCo-LDHs//AC asymmetric supercapacitor maintained 70.2% capacitance after 4000 cycles.

## 2.2 Hydrothermal and solvothermal methods

The hydrothermal and the solvothermal methods involve confining the reactants in a reactor where the reaction process is accomplished by chemical transfer.<sup>132</sup> Liquid or gaseous water is the medium for transferring pressure at high temperatures and pressures, and most of the reactants can be partially dissolved in water,<sup>133</sup> allowing the reaction to take place at a critical level (coexistence of gas and liquid phases).<sup>134</sup> Hydrothermal method is to first mix a certain proportion and concentration of mixed metal salt solution and alkali solution quickly, and immediately transfer it to stainless-steel high-pressure reaction kettle, reaction at a certain temperature for 6~24 h, finally through washing, drying, grinding can get powder products. The reaction environment is closed and stable with strong controllability, and the prepared product has crystal integrity and narrow particle size distribution.<sup>135</sup> It is found that the concentration of solution can affect the resulting morphology and properties of the synthesized material. When the concentration is too low, the

thickness of the nanosheet is uneven, while when the concentration is too high, the impurity phase is generated<sup>136</sup> Solvothermal method is developed on the basis of hydrothermal method<sup>137</sup>, in which the water is replaced by organic solvents or non-aqueous solvents (organic amines, alcohols, ammonia, carbon tetrachloride or benzene, etc.). Using the principle similar to hydrothermal method, in aqueous solution cannot grow, easy oxidation, easy hydrolysis or water sensitive materials are synthesized, such as III-V group semiconductor compounds, nitride, chalcogenide, new phosphorus (arsenic) molecular sieve 3D framework structure, etc.<sup>138, 139</sup> In the process of preparation, products with different sizes and morphologies can be obtained by adjusting the reaction temperature, reaction time, concentration of metal ions and surfactants. However, the high-pressure reactor can only adjust the external environment temperature, and the internal temperature and pressure are difficult to monitor. The reasonable control of reaction temperature and reaction time is beneficial for the synthesis of high performance LDHs materials. Through using ethanol as solvent, the NiCoAl-LDHNs were prepared with the aid of a one-step solvothermal method (Fig. 5(a)) by Meng et al.<sup>140</sup> As can be seen in Fig. 5 (b), the sample exhibits 3D nanoflower clusters. NiCoAl-LDHN-9 had a specific capacitance of 1228.5 F g<sup>-1</sup> at 1 A g<sup>-1</sup>. In the case of 20 A g<sup>-1</sup>, the value was 1001.8 F g<sup>-1</sup>, which still had a 81.6% capacitance retention (Fig. 5 (c)). The specific capacitance of NiCoAl-LDHN-9//AC device was 102.1 F g<sup>-1</sup> at 0.5 A g<sup>-1</sup> (Fig. 5 (d)). The energy density was 35.9 Wh kg<sup>-1</sup> at 225.8 W kg<sup>-1</sup>, and the capacitance retention rate was 87.1% undergoing 10000 cycles.

LDHs are produced on the surface of different substrates by hydrothermal and solvothermal

methods, and after reasonable regulation of the reaction time and other factors it is possible to obtain electrode materials with more satisfactory properties.<sup>141</sup> Li et al.<sup>142</sup> prepared a layered hybrid structure of NiCo<sub>2</sub>S<sub>4</sub> and NiCoAl-LDHs on binder less carbon cloth (CC) by a series of hydrothermal reactions (Fig. 5 (e)). Fig. 5 (f) shows the regular and uniformly grown nanosheet structure. The NiCoAl-LDHs@NiCo<sub>2</sub>S<sub>4</sub>@CC electrode exhibited 1775 F g<sup>-1</sup> at 1 A g<sup>-1</sup> (Fig. 5 (g)). At 10 A g<sup>-1</sup>, the value was 79.6% when the number of cycles reached 10000. Flexible solid-state asymmetric supercapacitors were assembled using NiCoAl-LDHs@ NiCo<sub>2</sub>S<sub>4</sub>@CC as the positive electrodes, with an energy density of 33.13 Wh kg<sup>-1</sup> at 750 W kg<sup>-1</sup> and a cycle performance of 71.4% after 10000 cycles (Fig. 5 (h)). By using a solvothermal way, Nguyen et al.<sup>143</sup> grew NiCo-LDHs in layers on nickel foam (NF) without using any binder to obtain NF@NiCo-LDHs material in Fig. 5 (i). The SEM image in Fig. 5 (j) shows that the nanosheets are interwoven with 25 nm thickness. This material achieved a 4392 F g<sup>-1</sup> specific capacitance at 0.44 A g<sup>-1</sup> (Fig. 5 (k)). The energy density of the prepared NF@NiCo-LDHs//AC device was 51.1 Wh kg<sup>-1</sup> at 777 W kg<sup>-1</sup>. The electrochemical stability was 72.2% undergoing 10,000 cycles at 10 mA cm<sup>-2</sup> (Fig. 5 (l)), demonstrating its potential for energy storage applications. Xue et al.<sup>144</sup> successfully synthesized core-shell NiCo<sub>2</sub>S<sub>4</sub>@NiMn-LDHs nanosheets hybrid on the surface of NF by a controlled three-step hydrothermal method, and NiMn-LDHs nanosheets of different thicknesses were attached to the outer layer of NiCo<sub>2</sub>S<sub>4</sub> nanotubes by adjusting the heating time of the hydrothermal reaction in Fig. 5 (m). NiMn-LDHs nanosheets are uniformly grown on NiCo<sub>2</sub>S<sub>4</sub> hollow nanotubes with complete connection and moderate thickness forming a stable core-shell system, which can

provide more porous channels. The SEM image is shown in Fig. 5 (n). The optimized  $\text{NiCo}_2\text{S}_4@\text{NiMn-LDHs}$  electrode transferred a specific capacitance of  $822.64 \text{ C g}^{-1}$  at  $50 \text{ mA cm}^{-2}$  (Fig. 5 (o)), and the specific capacitance was maintained at 92.7% experiencing 5000 cycles. In addition, the asymmetric supercapacitor prepared with  $\text{NiCo}_2\text{S}_4@\text{NiMn-LDHs}$  has a maximum energy density of  $53.10 \text{ Wh kg}^{-1}$  at  $370.82 \text{ W kg}^{-1}$  and an 94.3% capacitance retention under 10000 cycles at  $20 \text{ mA cm}^{-2}$ .

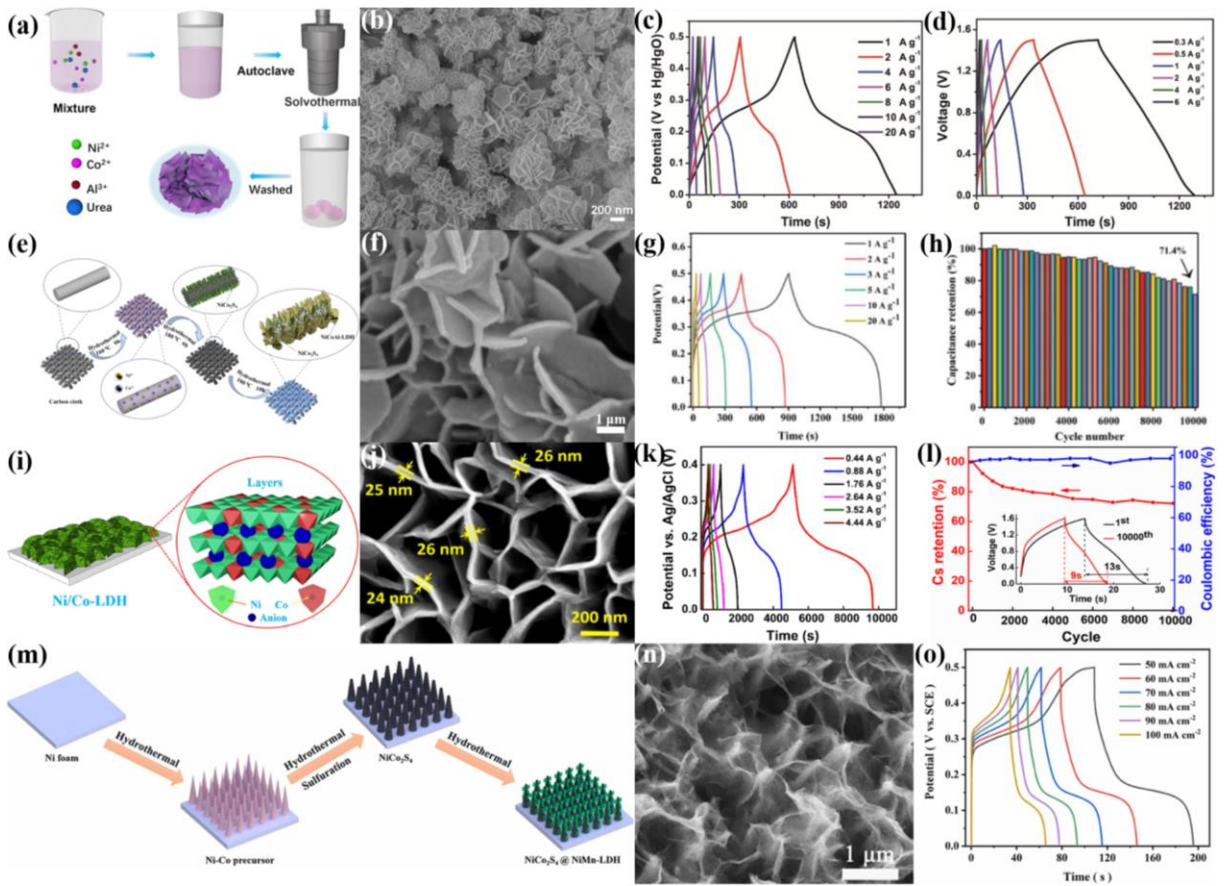


**Fig. 5** (a) Schematic representation of the synthesis of  $\text{NiCoAl}$  LDHs nanosheets, (b) SEM image of  $\text{NiCoAl-LDHN-9}$ , (c) GCD curves of the  $\text{NiCoAl-LDHN-9}$  electrode at various current densities, (d) GCD curves of the device at different current densities.<sup>140</sup> Copyright 2021, Elsevier B.V. (e) Schematic

illustration of the synthesis processes of hierarchical NiCoAl-LDHs@NiCo<sub>2</sub>S<sub>4</sub>@CC, (f) SEM image of NiCoAl-LDHs@NiCo<sub>2</sub>S<sub>4</sub>@CC, (g) GCD curves of NiCoAl-LDHs@NiCo<sub>2</sub>S<sub>4</sub>@CC at various current densities, (h) cycling stability performance of device at 1 A g<sup>-1</sup>.<sup>142</sup> Copyright 2021 Elsevier B.V. (i) Schematic diagram of the structural growth of NiCo LDHs on NF substrate, (j) SEM image of NiCo LDHs, (k) GCD curves at different current densities, (l) cycling stability and coulombic efficiency of the NiCo LDHs//AC, the inset showing the first and 10000th GCD curves.<sup>143</sup> Copyright 2020, Elsevier Ltd. (m) Schematic illustration of the synthesis processes of NiCo<sub>2</sub>S<sub>4</sub>@NiMn-LDHs core-shell hybrid arrays on NF, (n) SEM image of NiCo<sub>2</sub>S<sub>4</sub>-NM-6, (o) GCD curves at different current densities.<sup>144</sup> Copyright 2021, Elsevier B.V.

A number of hybrids based on LDHs with superior properties can also be obtained by hydrothermal and solvothermal methods. NiMn-LDHs/hrGO hybrids were fabricated by a solvothermal route by Yan et al.<sup>145</sup> The incorporation of hrGO improved the conductivity and specific surface area. At 1 A g<sup>-1</sup>, the capacitance was up to 302.0 C g<sup>-1</sup>. The asymmetric supercapacitor achieved a specific capacitance of 237.6 C g<sup>-1</sup> at 1 A g<sup>-1</sup>, a cycling stability of 80.5% after 2000 cycles, and an energy density of 59.9 Wh kg<sup>-1</sup> 901.5 W kg<sup>-1</sup>. Wang et al.<sup>146</sup> fabricated uniformly NiCo-LDHs nanosheet arrays on Cu<sub>0.92</sub>Co<sub>2.08</sub>O<sub>4</sub> (CCO) nanowires using a two-step solvothermal method in Fig. 6 (a). The non-homogeneous core-shell structure consists of a highly conductive core layer and a highly capacitive shell layer, and CCO can slow down the agglomeration of NiCo-LDHs nanosheets. The CCO@NiCo-LDHs electrode provided a specific capacitance of 1652 F g<sup>-1</sup> at 1 A g<sup>-1</sup>. The flexible asymmetric supercapacitor has an energy density



of 42.38 Wh kg<sup>-1</sup> at 1350 W kg<sup>-1</sup>.

LDHs have certain drawbacks in terms of performances and still need to be used in conjunction with other methods to prepare the ideal electrode materials. Fu et al.<sup>147</sup> fabricated a NiCeCo LDHs on copper bromide nanowire arrays (CuBr<sub>2</sub>@NiCeCo-LDHs) by hydrothermal and calcination methods, and a visual representation of the preparation is illustrated in Fig. 6 (c). The CuBr<sub>2</sub>@NiCeCo-LDHs electrode exhibited excellent electrochemical performances with a 5460 mF cm<sup>-2</sup> area capacitance at 2 mA cm<sup>-2</sup> and 88% capacitance retention at 50 mA cm<sup>-2</sup> due to unique top entangled structure (Fig. 6 (d)) and the complex assembly of different active components. The asymmetric supercapacitor with CuBr<sub>2</sub>@NiCeCo-LDHs and AC electrodes has an energy density of 118 Wh kg<sup>-1</sup> at 1013 W kg<sup>-1</sup>. Besides, Wang et al.<sup>148</sup> synthesized a hydrophobic-like NiCo-LDHs precursor (Fig. 6 (e)) by a hydrothermal method. Based on this precursor, highly conductive sulfide nanoparticles were constructed on NiCo-LDHs nanosheets (Fig. 6 (f)) by ion-exchange strategy. The newly formed heterojunction between NiCo-LDHs and sulfide nanoparticles enabled them to provide ion or electron transfer paths to each other, significantly improving the conductivity. Through the adjustment of thioacetamide amount, the optimized NiCo-LDHs/S-15 material has a 267.8 mAh g<sup>-1</sup> specific capacitance at 1 A g<sup>-1</sup>. The assembled supercapacitor has a specific capacitance of 126.76 F g<sup>-1</sup> at 1 A g<sup>-1</sup>, a reasonable energy density and power density (43.6 Wh kg<sup>-1</sup>, 375 W kg<sup>-1</sup>), and a 83% capacitance retention undergoing 5000 cycles.

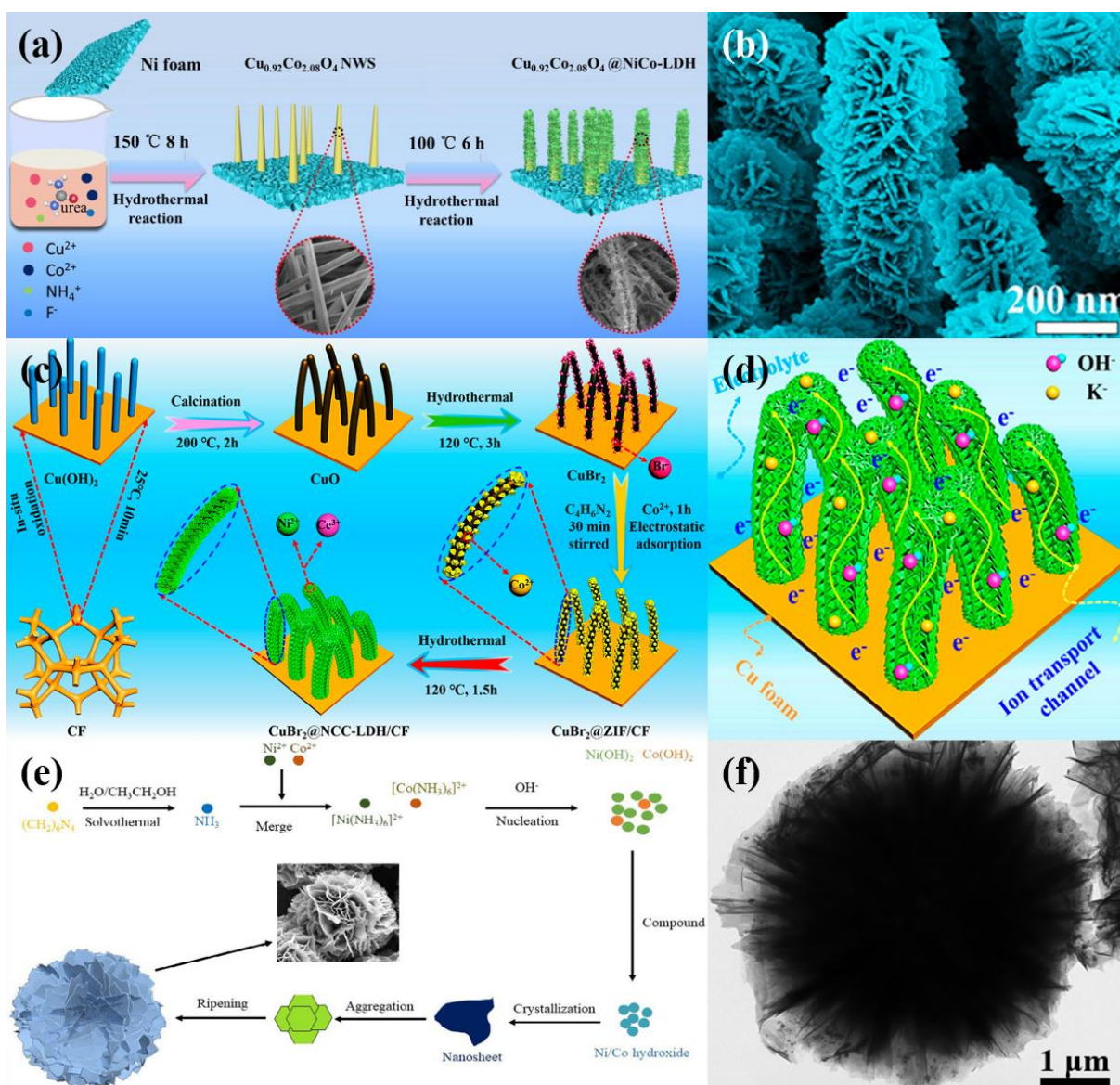


Fig. 6 (a) Synthetic schematic of  $\text{Cu}_{0.92}\text{Co}_{2.08}\text{O}_4@\text{NiCo-LDHs}$ ,<sup>146</sup> Copyright 2021, Elsevier Ltd. (b) SEM images of the  $\text{CuBr}_2@\text{NiCeCo-LDHs}$  core-shell nanorod, (c) schematic illustration of the  $\text{CuBr}_2@\text{NiCeCo-LDHs}$  core-shell nanorod, (d) schematic diagram of electron and ion transfer across the surface of the active component.<sup>147</sup> Copyright 2022, American Chemical Society. (e) Synthetic schematic of NiCo-LDHs synthesis, (f) TEM image of  $\text{NiCo-LDHs/S-15}$ .<sup>148</sup> Copyright 2022, Elsevier Ltd.

Liu et al.<sup>149</sup> successfully synthesized a nano-flowery  $\text{NiAl-LDHs-S}$  electrode material by a



pre-synthetic solvothermal reaction using a sulfide modification procedure, as shown in Fig. 7 (a). The obtained NiAl-LDHs-S electrode material has a  $1680 \text{ F g}^{-1}$  specific capacitance at  $1 \text{ A g}^{-1}$  because of the generation of sulfide on the surface of LDHs. The energy density of the assembled NiAl-LDHs-S//AC asymmetric supercapacitor reaches  $35.78 \text{ Wh kg}^{-1}$  at  $1127.03 \text{ W kg}^{-1}$ . In Fig. 7 (b), Liu et al.<sup>150</sup> synthesized a Se-NiAl-LDHs electrode material by pre-synthetic solvothermal reaction and selenide modification. It is worth noting that some new selenide crystals were generated, and the obtained material has a  $1098 \text{ F g}^{-1}$  specific capacitance at  $1 \text{ A g}^{-1}$ . The energy density of the Se-NiAl-LDHs//AC device is  $29 \text{ Wh kg}^{-1}$  at  $1593.17 \text{ W kg}^{-1}$ . Besides, Liu et al.<sup>151</sup> decorated Ag nanoparticles on CoAl-LDHs flower-like hollow microspheres in Fig. 7 (c) by a simple one-step solvothermal reaction and chemical plating solution deposition reaction. The modification of Ag nanoparticles can promote the fast diffusion kinetics and electrochemical reactivity of electrolyte ions. The prepared Ag/CoAl-2 LDHs had a  $1214 \text{ C g}^{-1}$  specific capacitance at  $3 \text{ A g}^{-1}$  and a 91% capacity retention at  $10 \text{ A g}^{-1}$  for 10000 cycles. Moreover, the assembled device using Ag/CoAl-LDHs and N-doped carbon nanotubes (N-CNTs) separately as electrodes, exhibited an energy density of  $61.2 \text{ Wh kg}^{-1}$  at  $800 \text{ W kg}^{-1}$ , declaring the great promise of engineered conductive nanoparticle modified LDHs-based active materials for high-performance supercapacitors.

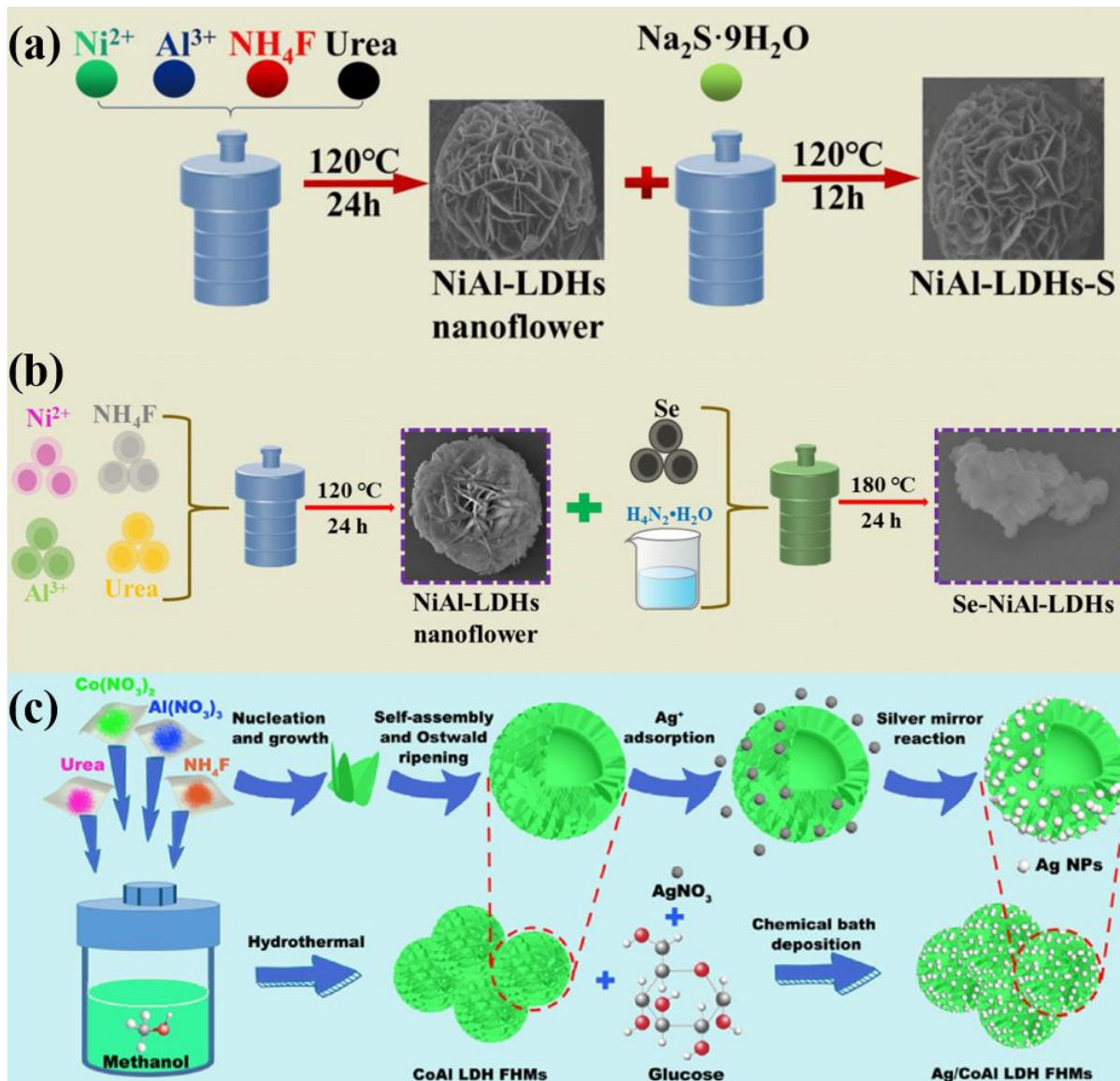


Fig. 7 (a) The preparation process route of the NiAl-LDHs and NiAl-LDHs-S.<sup>149</sup> Copyright 2022, Elsevier

B.V. (b) Roadmap for the synthesis of NiAl-LDHs and Se-NiAl-LDHs materials.<sup>150</sup> Copyright 2022,

Elsevier Ltd. (c) Schematic illustration of the preparation of Ag/CoAl-LDHs.<sup>151</sup> Copyright 2020, Elsevier

Inc.

## 2.3 Electrodeposition method

Electrodeposition method is a technique in which an electric current is passed through the

electrolyte solution and a redox reaction takes place at the electrode to fabricate a coating.<sup>152, 153</sup>

The reduction of metal ions at the cathode to produce a metallic coating is called electroplating.<sup>154,</sup>

<sup>155</sup> It requires the use of a conductive substrate as the working electrode. Typically, a three-electrode system is worked in an electrolyte containing a metal precursor, and then LDHs nanostructures are synthesized on the working electrode at or within a certain potential range.<sup>156</sup>

The advantage of this method is that, in most cases, no additional reagents are required to induce the formation of hydroxides other than the metal precursors.<sup>157</sup> During the electrodeposition process, water molecules are electrolyzed to produce oxygen and hydroxide ions, which facilitate the formation of metal hydroxides.<sup>158, 159</sup> The main difference between electrochemical deposition and chemical plating is that although both redox reactions are carried out in solution, the former occurs at the electrode through the migration of ions in the presence of an electric field, while the latter is formed directly on the surface of the workpiece through the autocatalytic action of the chemical plating solution.<sup>160</sup>

The method can be applied to obtain LDHs materials with various grain sizes. However, the generation and growth rate of nuclei on the substrate surface cannot be controlled. The LDHs materials with excellent performances can be obtained by selecting suitable electrodeposition conditions and choosing reasonable electrolyte and matrix.

Huang et al.<sup>161</sup> obtained a unique array of LDHs nanosheets with intercalated pseudocapacitive properties and battery-type electrode materials by a simple and pollution-free two-step electrodeposition technique. The electrode material consists of MoO<sub>3</sub> and NiCo-LDHs grown directly on a 3D conductive NF substrate to form a binder-free 2D ultrathin cross-layered heterostructure (NiCo-

LDHs@MoO<sub>3</sub>/NF) (Fig. 8 (a)). At 1 A g<sup>-1</sup>, the specific capacitance of this heterogeneous nanomaterial was 952.2 C g<sup>-1</sup> at 1 A g<sup>-1</sup>, Fig. 8 (b) clearly shows that this composite outperforms the other two individual materials produced directly on the substrate, and the capacity retention was 86.42% after 10000 cycles. The NiCo-LDHs@MoO<sub>3</sub>/NF//AC device (Fig. 8 (c)) has an energy density of 58.06 Wh kg<sup>-1</sup> at 800 W kg<sup>-1</sup>, as well as a 84.57% capacity retention after 10000 cycles. Zhang et al.<sup>162</sup> used MoO<sub>3</sub> nanorod arrays as a matrix to encapsulate NiCo-LDHs by electrodeposition to obtain a layered MoO<sub>3-x</sub>@NiCo LDHs containing oxygen vacancies. The MoO<sub>3-x</sub>@NiCo-LDHs-15 electrode exhibited a capacitance of 3.49 F cm<sup>-2</sup> at 5 mA cm<sup>-2</sup> (Fig. 8 (e)), and the capacitance retention was 94.9% after 3000 cycles in neutral electrolyte (Fig. 8 (d)). The corresponding symmetric flexible solid-state supercapacitor exhibits good flexibility and an energy density of 0.047 mWh cm<sup>-2</sup> at 0.865 mW cm<sup>-2</sup>. In this work, the layered structure changes the microenvironment of the electrode surface, shortening the ion transport path and accelerating the reaction kinetics. Moreover, the NiCo-LDHs nanosheets tightly packed on the surface of the MoO<sub>3</sub> nanorod arrays slow down the structural collapse during potassium ion removal. In addition, the formation of oxygen vacancies enhances structural stability and electrical conductivity of MoO<sub>3</sub>. Therefore, this study provides a new strategy for constructing flexible electrode materials with high electrochemical performance, which is of great value in subsequent applications. Amin et al.<sup>163</sup> used the electrodeposition method to directly grow NiCo layered double hydroxide nanosheets on Ni nanotube (Ni-NTNW) networks to obtain a 3D self-supporting layered electrode. The electrode utilizes the large interface and high redox activity of the 2D coated nanosheets, and

the highly porous network structure of the 1D Ni-NTNW support enhances its performance, enables fast mass transfer, and acts as a "highway for fast electron transfer". At  $0.2 \text{ mA cm}^{-2}$  the as-prepared NiCo-LDHs@Ni-NTNW structure exhibits an ultrahigh capacity of  $126.4 \text{ C cm}^{-3}$ . Furthermore, the assembled NiCo-LDHs@Ni-NTNW//AC asymmetric supercapacitor (Fig. 8 (g)) can provide a  $76.7 \text{ F cm}^{-3}$  capacitance at  $1 \text{ mA cm}^{-2}$ . Meanwhile, its energy density of  $14.7 \text{ mWh cm}^{-2}$  at  $4769 \text{ mW cm}^{-2}$  exceeds most state-of-the-art supercapacitors. Thus, hybrid core-shell nanotube networks represent an emerging design paradigm for high-performance devices in portable devices.

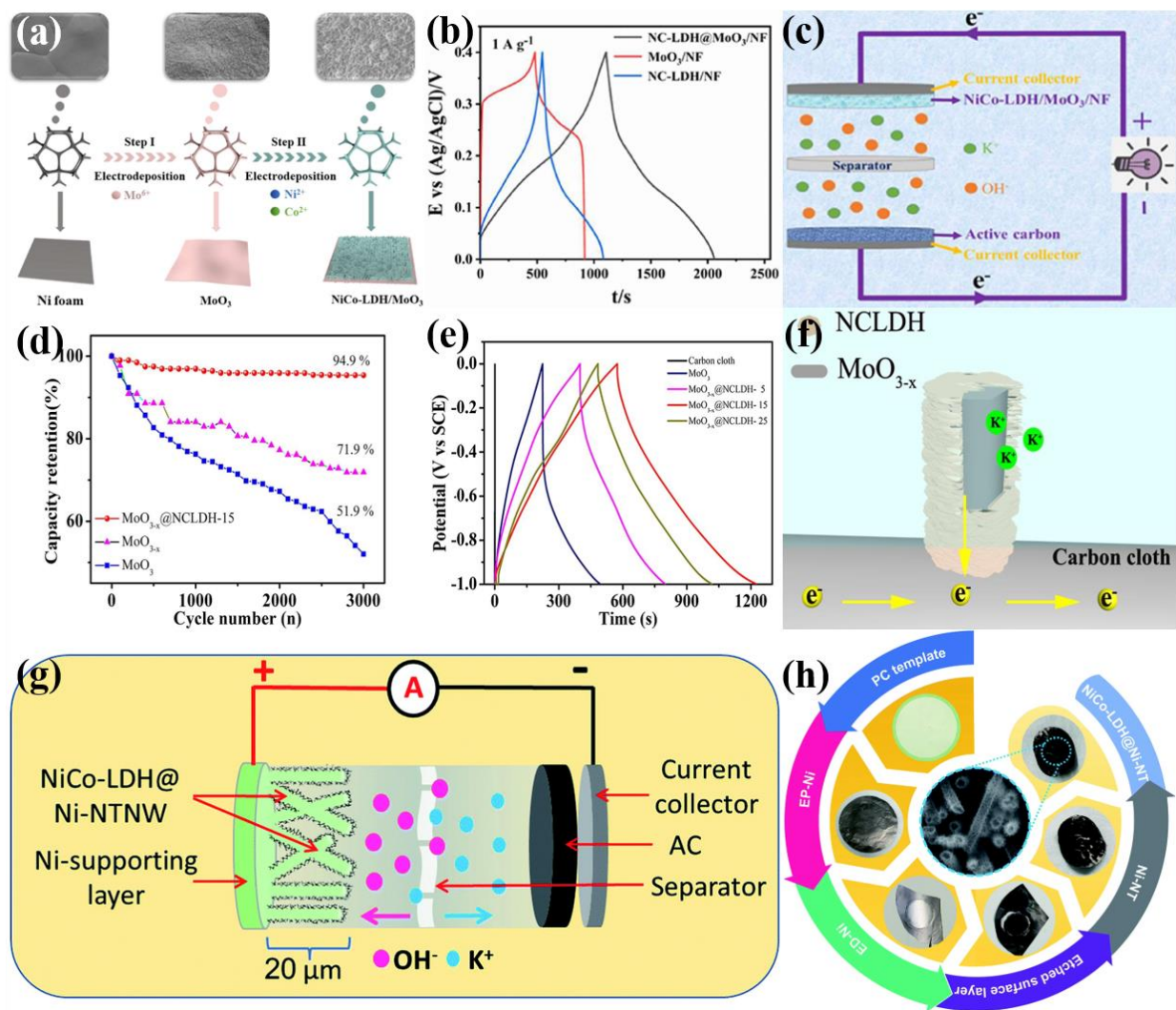


Fig. 8 (a) Schematic illustration of the preparation procedures for NiCo-LDHs@MoO<sub>3</sub>/NF, (b) GCD curves of MoO<sub>3</sub>/NF, NiCo-LDHs/NF and NiCo-LDHs@MoO<sub>3</sub>/NF electrodes, (c) schematic diagram of the assembled device.<sup>161</sup> Copyright 2021, Elsevier Ltd. (d) Cycle performance of MoO<sub>3</sub>, MoO<sub>3-x</sub> and MoO<sub>3-x</sub>@NiCo-LDHs-15 at 10 mA cm<sup>-2</sup>, (e) GCD curves at 5 mA cm<sup>-2</sup>, (f) schematic transportation process of electrons and ions in MoO<sub>3-x</sub>@NiCo-LDHs.<sup>162</sup> Copyright 2021, Elsevier B.V. (g) Schematic illustration of the assembled NiCo-LDHs@Ni-NTNW//AC device, (h) Schematic illustration presenting photographs of the self-supported NiCo-LDHs@Ni-NTNW electrode through the fabrication process.<sup>163</sup> Copyright 2022,



In Fig. 9 (a), Zhao et al.<sup>164</sup> successfully prepared NiCoFe-LDHs nanosheet electrodes with high specific capacitance and electrical conductivity by electrodeposition on CC. More importantly, the multiplicative performance and the cycling stability were better compared with the NiCo-LDHs electrode, which reached 145% stability after 4000 cycles. Moreover, the NiCoFe-LDHs//AC device has a 207 F g<sup>-1</sup> specific capacitance at 1 mA cm<sup>-2</sup> and an energy density of 65 Wh kg<sup>-1</sup> at 83 W kg<sup>-1</sup>. Moreover, the device has a very excellent cycling stability of 126% undergoing 5000 cycles. Wang et al.<sup>165</sup> used electrochemical deposition to synthesize NiCo-LDHs on a graphite paper-derived 3D electrode substrate (called EGP, with partially exfoliated graphite sheets and expanded lateral graphite layers on the surface), resulting in EGP@NiCo-LDHs electrode material (Fig. 9 (b)). Due to the simultaneous 3D electrode structure and the high capacitance of NiCo-LDHs, EGP@NiCo-LDHs exhibit ultrahigh capacitance (1650 F g<sup>-1</sup> at 1 A g<sup>-1</sup>) and excellent rate capability. In addition, the asymmetric device achieves an energy density of 44.31 Wh kg<sup>-1</sup> at 799.98 W kg<sup>-1</sup> and a 92.8% retention rate experiencing 5000 cycles.

The use of electrodeposition in conjunction with other methods results in improved electrode materials with better performances. Wang et al.<sup>166</sup> prepared oxygen-rich NiCo-LDHs with excellent supercapacitor performance on NF substrates by electrodeposition and in situ oxidation. The oxygen vacancies can be adjusted by hydrogen peroxide treatment to remarkably enhance electrical conductivity and electrochemical properties of the materials. The NiCo-LDHs containing oxygen vacancies (O<sub>v</sub>-NiCo-LDHs) reached a 1160 C g<sup>-1</sup> specific capacitance at 1 A g<sup>-1</sup> as well as

showed 61% retention at 20 A g<sup>-1</sup>. The symmetrical device has an energy density of 216.19 Wh kg<sup>-1</sup> at 1.75 kW kg<sup>-1</sup>. Wang et al.<sup>167</sup> prepared a core-sheath heterostructure (MnCo<sub>2</sub>O<sub>4</sub>@NiCo-LDHs/NF) (Fig. 9 (c)) consisting of MnCo<sub>2</sub>O<sub>4</sub> nanowires encapsulated by NiCo-LDHs nanosheets using a combination of hydrothermal preparation and electrochemical deposition. The material achieved a 4555.0 F g<sup>-1</sup> specific capacitance at 1 A g<sup>-1</sup>. Furthermore, the MnCo<sub>2</sub>O<sub>4</sub>@NiCo-LDHs/NF//AC asymmetric device has an energy density of 21.3 Wh kg<sup>-1</sup> at 160.0 W kg<sup>-1</sup> and can be able to light up a green LED indicator for more than 30 min. Wan et al.<sup>168</sup> in situ modified highly porous FeCoSe<sub>2</sub>@NiCo-LDHs core-shell nanosheet arrays on the surface of CC by electrodeposition method and salinization treatment, as displayed in Fig. 9 (d). Hierarchical heterostructures composed of two vertically aligned interconnected 2D nanosheets not only provide a huge surface area and efficient diffusion pathways for fast electron/ion transport, but also generate abundant electronically altered heterointerfaces, resulting in a synergistic effect between the two components. The obtained FeCoSe<sub>2</sub>@NiCo-LDHs electrode achieves a 220.9 mAh g<sup>-1</sup> specific capacitance at 1 A g<sup>-1</sup>, as well as the cycle is better than that of the single component. Furthermore, the device assembled using FeCoSe<sub>2</sub>@NiCo-LDH electrode and layered porous carbon electrode exhibits an energy density of 1.248 kW kg<sup>-1</sup> at 65.9 Wh kg<sup>-1</sup>, and the capacity retention of 10000 cycles is 87.6%.



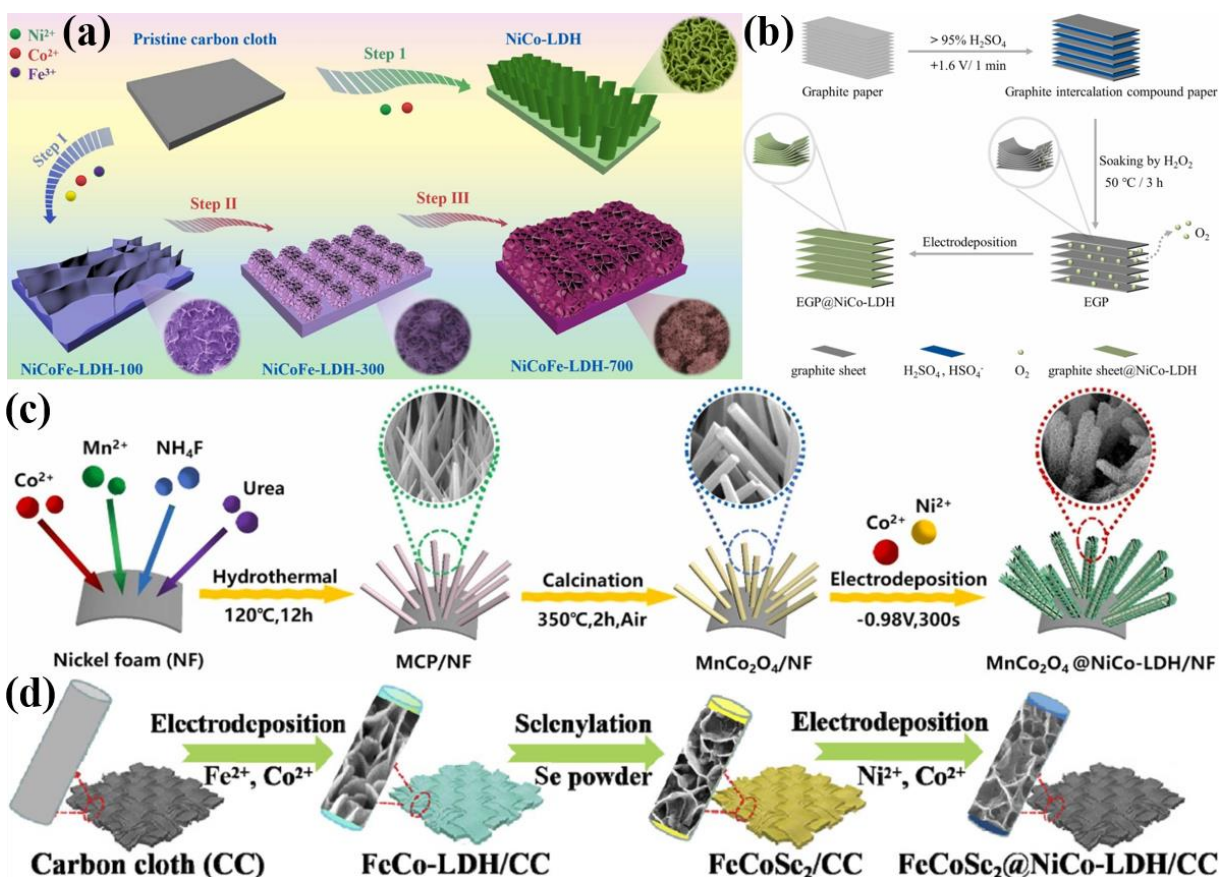


Fig. 9 (a) Schematic illustration of the synthesis processes of the as-made NiCoFe-LDHs electrode.<sup>164</sup>

Copyright 2021, Elsevier B.V. (b) Schematic illustration of the fabrication processed of EGP@NiCo-LDHs

electrode.<sup>165</sup> Copyright 2022, Elsevier B.V. (c) Schematic illustration for the fabrication of

$\text{MnCo}_2\text{O}_4$ @NiCo-LDHs/NF core-sheath heterostructure.<sup>167</sup> Copyright 2022, Elsevier B.V. (d) Schematic

illustration for the fabrication steps of  $\text{FeCoSe}_2$ @NiCo-LDHs nanosheet arrays on CC.<sup>168</sup> Copyright 2022,

Elsevier B.V.

## 2.4 Electrostatic interstratification

Because the big distance between the layers of LDHs, the inserted anions are difficult to contact to increase the electrical conductivity, lowering the electrochemical properties. In order to solve this problem, various methods have been tried to spin out the LDHs into thin layers, such as

mechanical agitation and with larger anion exchange reaction.<sup>169, 170</sup> However, the re-stacking of these shed layers is a thermodynamically driven process to stabilize the high surface area of these layers. To this end, sandwiching the positively charged LDHs with the negatively charged 2D thin material between the layers is an effective method to obtain better electrical conductivity and higher electrochemical performances.<sup>171-174</sup> MXene is a 2D layered material with excellent properties<sup>175</sup> and has a wide range of applications<sup>176</sup> in the synthesis of LDHs using electrostatic interlayer interaction.<sup>10, 177-179</sup> The method can generate a sandwich-like electrostatic layer between LDHs with positive charge and 2D thin materials with negative charge, which can achieve better conductivity and superior electrochemical properties. However, two materials with different charges need to be carefully searched. If the properties of various materials are widely understood, suitable materials are selected, and suitable intercalators are introduced in the synthesis process, the performances of the materials can be obviously enhanced. Zhao et al.<sup>180</sup> prepared a surface covalently functionalized MXene based  $\text{Ti}_3\text{C}_2\text{Cl}_2$  nanodot-dotted MXene@NiAl-LDHs (QD- $\text{Ti}_3\text{C}_2\text{Cl}_2$ @NiAl-LDHs) composite electrode (Fig. 10 (a)) and SEM image is shown in Fig. 10 (b). The QD- $\text{Ti}_3\text{C}_2\text{Cl}_2$ @NiAl-LDHs electrode displayed a 2010.8 F g<sup>-1</sup> specific capacitance at 1.0 A g<sup>-1</sup> (Fig. 10 (c)). The capacitance retention reached 94.1% after 10000 cycles at 1.0 A g<sup>-1</sup> (Fig. 10 (d)). Wu et al.<sup>181</sup> used an electrostatic assembly method to establish a 2D structure between MXene modified with cetyltrimethylammonium bromide cation (CTAB) and NiCo-LDHs modified with dodecyl benzenesulfonic acid anion. Composite electrodes are assembled with each other (Fig. 10 (e)). In this case, the self-stacking of MXene and NiCo-LDHs nanosheets is effectively prevented,

resulting in a regular interlayer structure and large interlayer spacing, accelerating the movement of electrolyte ions. Fig. 10 (f) shows SEM image of the MXene/NiCo-LDHs. At  $0.5 \text{ A g}^{-1}$ , the specific capacitance of the electrode is  $1207 \text{ F g}^{-1}$  (Fig. 10 (g)), and the capacitance retention is 93% after 5000 cycles. In addition, its maximum energy density is  $107.3 \text{ Wh kg}^{-1}$  ( $98.5 \text{ mWh cm}^{-3}$ ), and its power density is  $571 \text{ W kg}^{-1}$  ( $524 \text{ mW cm}^{-3}$ ). This remarkable electrochemical performances are mainly attributed to the hydration of 2D electrodes and the exchange or adsorption of anions between layers.

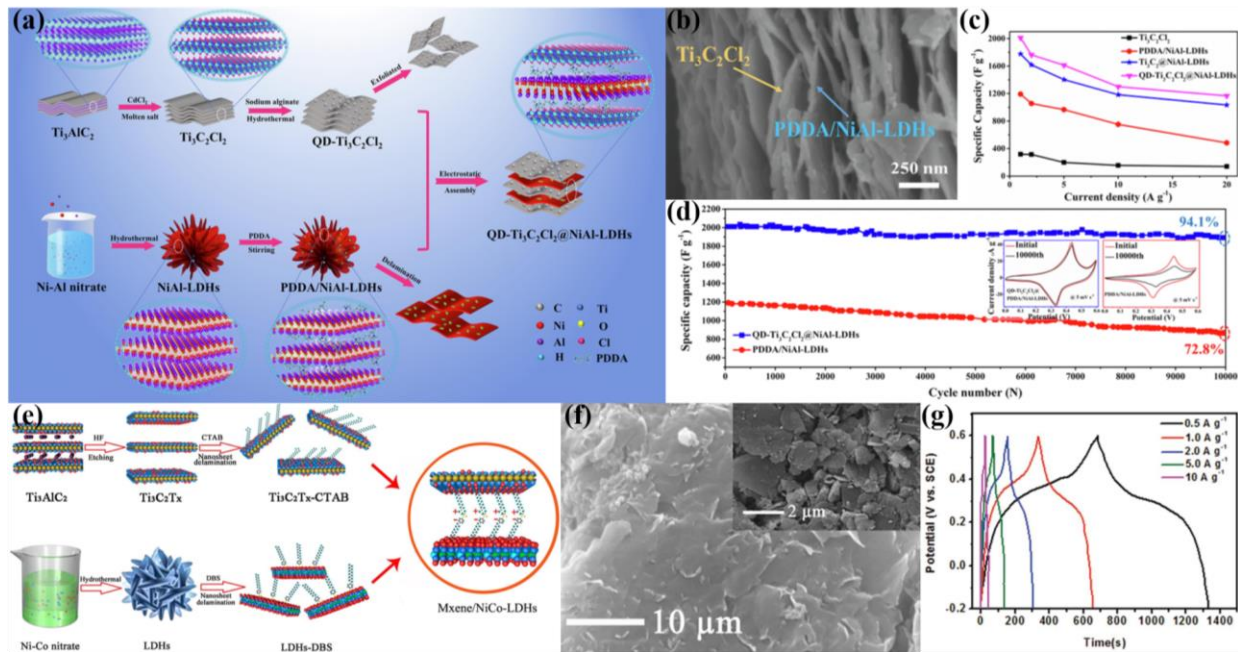


**Fig. 10** (a) Schematic diagram of the processes for synthesizing  $\text{QD-Ti}_3\text{C}_2\text{Cl}_2@\text{NiAl-LDHs}$  electrode by electrostatic attraction and self-assembly and (b) the corresponding cross-sectional SEM image, (c) specific capacitances of the  $\text{Ti}_3\text{C}_2\text{Cl}_2$  MXene,  $\text{PDDA/NiAl-LDHs}$ ,  $\text{Ti}_3\text{C}_2@\text{NiAl-LDHs}$  and  $\text{QD-Ti}_3\text{C}_2\text{Cl}_2@\text{PDDA/NiAl-LDHs}$  at different current densities, (d) the cycling stability of the  $\text{PDDA/NiAl-LDHs}$  and  $\text{QD-Ti}_3\text{C}_2\text{Cl}_2@\text{PDDA/NiAl-LDHs}$  at  $1.0 \text{ A g}^{-1}$ , the inset of the CV curves of the above electrodes

before and after 10000 cycles.<sup>180</sup> Copyright 2021, Elsevier Inc. (e) Schematic illustration for the fabrication of 2D MXene/NiCo-LDHs by electrostatic adsorption of anion-cation, and (f) the corresponding cross-sectional SEM images, (g) specific capacitance of MXene, NiCo-LDHs and MXene/NiCo-LDHs at different current densities.<sup>181</sup> Copyright 2019, Elsevier B.V.

## 2.5 Miscellaneous methods

In addition to the conventional methods, there are a variety of other methods used to synthesize LDHs. Exfoliative recombination method has the advantages of it is a simple process with mild conditions and the disadvantage of its parameters are very hard to control. The LDHs with better performances can be obtained by regulating the experimental parameters reasonably.

NiCr LDHs and polyoxotungstate nanoclusters (NiCr-LDHs-POW) were fabricated by Padalkar et al.<sup>182</sup> using an exfoliative recombination method, as shown in Fig. 11 (a). The intercalation of POW nanoclusters forms a stacked framework layer by layer, obtaining a high specific surface area interconnected lamellar morphology, increasing ion transport channels and facilitating the diffusion of electrolyte ions between the layers. Alkaline etching is another simple and efficient method to increase the porosity of aluminum-containing layered double hydroxyl talc. Wang et al.<sup>183</sup> synthesized NiTiAl-LDHs by adding a trace amount of Al to the NiTi-LDHs substrate layer and then etching some Al with a sodium hydroxide solution, resulting in higher specific surface area, specific capacitance and rate performance of supercapacitor electrodes. Microwave synthesis method has the advantages of high heating rate, high thermal energy utilization, and good crystallinity and dispersion of the synthesized materials. However, this method has high

requirements for equipment. Considering the condition of using this method fully, it can be combined with other methods. Wang et al.<sup>184</sup> synthesized 3D hollow NiCo-LDHs with interlaced nanosheets in the shell layer using ZIF-67 as a template by microwave treatment (Fig. 11 (b)). As an electrode material, NiCo-LDHs has a 2369.0 F g<sup>-1</sup> specific capacitance at 0.5 A g<sup>-1</sup>, as well as multiplicative performance, more exposed active sites and synergistic interaction between the Ni-Co ions facilitating ion transport and diffusion. In addition, the assembled NiCo LDHs//AC device has 83.6% capacitance retention experiencing 10000 cycles. Besides, Chu et al.<sup>185</sup> integrated CuCo-LDHs nanoarrays onto NF by in situ hydrolysis approach (Fig. 11 (c)). The resulting CuCo-LDHs//AC asymmetric supercapacitor exhibits an energy density of 22 Wh kg<sup>-1</sup>. This approach provides a new idea for the preparation of superior supercapacitor electrode materials in the future. In order to show the performances of the LDHs and their corresponding composites more intuitively, the properties of LDHs and its composite electrodes mentioned in this chapter are exhibited in Table 1. Concurrently, the properties of devices consisting of LDHs and its composites mentioned in this chapter are show in Table 2.

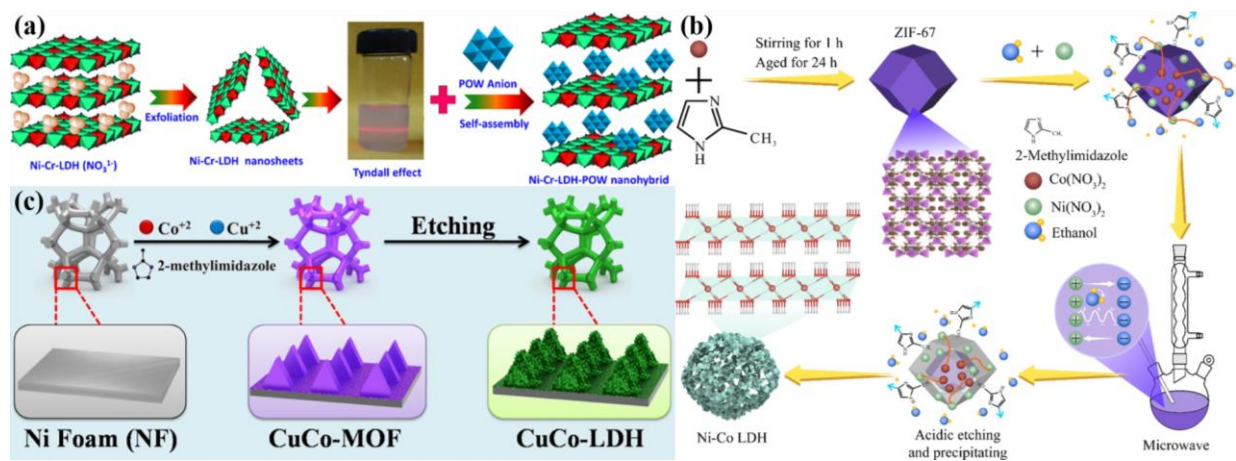


Fig. 11 (a) Schematic diagram of the exfoliation-reassembling route to NiCr-LDHs nanohybrids.<sup>182</sup>

Copyright 2022, Elsevier Inc (b) Schematic illustration for the synthesis procedures of NiCo-LDHs nanocages.<sup>184</sup> Copyright 2022, Elsevier B.V. (c) Schematic illustration of the synthesis strategy and morphological characterization of CuCo-LDHs.<sup>185</sup> Copyright 2022, American Chemical Society.



**Table.1 The properties of LDHs and its composite electrodes mentioned in this chapter.**

Method	Electrode	Electrolyte	Capacitance	Condition	Cycles	Ref.
Co-precipitation	Zn Al-LDHs	6 M KOH	37.0 F g <sup>-1</sup>	1 A g <sup>-1</sup>	—	124
Co-precipitation	Ni Fe-LDHs	2 M KOH	1368 F g <sup>-1</sup>	1 A g <sup>-1</sup>	5000, 87.5%	125
Co-precipitation	Ni Co-LDHs	2 M KOH	1970 F g <sup>-1</sup>	1 A g <sup>-1</sup>	—	126
Co-precipitation	P@NiCo-LDHs	6 M KOH	536 C g <sup>-1</sup>	1 A g <sup>-1</sup>	5000, Rarely decrease	127
Co-precipitation	Zn <sub>0.25</sub> Ni <sub>0.75</sub> Co-LDHs-BA <sup>-</sup>	2 M KOH	1378 mAh g <sup>-1</sup>	1 A g <sup>-1</sup>	10000, 91.2%	129
Co-precipitation	S-NiCoAl-LDHs	1 M KOH	727.1 C g <sup>-1</sup>	1 A g <sup>-1</sup>	10000, 95.1%	130
Co-precipitation	HC@NiCo-LDHs	2 M KOH	758 C g <sup>-1</sup>	2 A g <sup>-1</sup>	—	131
Hydrothermal	NiCoAl-LDHs@NiCo <sub>2</sub> S <sub>4</sub> @CC	6 M KOH	1775 F g <sup>-1</sup>	1 A g <sup>-1</sup>	10000, 79.6%	142
Solvothermal	CuBr <sub>2</sub> @NCC-LDHs/CF	6 M KOH	5460 mF cm <sup>-2</sup>	2 mA cm <sup>-2</sup>	5000, 88%	147
Hydrothermal	NC/S-15	2 M KOH	267.8 mAh g <sup>-1</sup>	1 A g <sup>-1</sup>	2000, 70.4%	148
Hydrothermal	NiCo <sub>2</sub> S <sub>4</sub> @NiMn-LDHs	2 M KOH	822.64 C g <sup>-1</sup>	50 mA cm <sup>-2</sup>	5000, 92.7%	144

Solvothermal	NiAl-LDHs-S	6 M KOH	1680 F g <sup>-1</sup>	1 A g <sup>-1</sup>	—	149
Solvothermal	NiMn-LDHs/hrGO	2 M KOH	302 C g <sup>-1</sup>	1 A g <sup>-1</sup>	2000, 89.6%	145
Solvothermal	CCO@NiCo-LDHs	3 M KOH	1652 F g <sup>-1</sup>	1 A g <sup>-1</sup>	10000, 72.5%	146
Solvothermal	Se-NiAl-LDHs	6 M KOH	1098 F g <sup>-1</sup>	1 A g <sup>-1</sup>	—	150
Solvothermal	NiCoAl-LDHN-9	6 M KOH	1228.5 F g <sup>-1</sup>	1 A g <sup>-1</sup>	—	140
Solvothermal	NF@NiCo-LDHs	3 M KOH	4392 F g <sup>-1</sup>	0.44 A g <sup>-1</sup>	10000, 64.2%	143
Solvothermal	Ag/CoAl-LDHs	2 M KOH	1214 C g <sup>-1</sup>	3 A g <sup>-1</sup>	10000, 91%	151
Electrodeposition	NiCo-LDHs@MoO <sub>3</sub> /NF	2 M KOH	952.2 C g <sup>-1</sup>	1 A g <sup>-1</sup>	10000, 86.42%	161
Electrodeposition	NiCoFe-LDHs	3 M KOH	3800 mC cm <sup>-2</sup>	4 mA cm <sup>-2</sup>	4000, 149%	164
Electrodeposition	EGP@NiCo-LDHs	2 M KOH	1650 F g <sup>-1</sup>	1 A g <sup>-1</sup>	—	165
Electrodeposition	O <sub>v</sub> -NiCo-LDHs	3 M KOH	1160 C g <sup>-1</sup>	1 A g <sup>-1</sup>	5000, 73.5%	166
Electrodeposition	MoO <sub>3-x</sub> @NiCo-LDHs	0.5 M K <sub>2</sub> SO <sub>4</sub>	3.49 F cm <sup>-2</sup>	5 mA cm <sup>-2</sup>	3000, 94.5%	162
Electrodeposition	MnCo <sub>2</sub> O <sub>4</sub> @NiCo-LDHs/NF	6 M KOH	4555 F g <sup>-1</sup>	1 A g <sup>-1</sup>	5000, 78.7%	167



Electrodeposition	NiCo-LDHs@Ni-NTNW	1 M KOH	1202.2 F g <sup>-1</sup>	0.2 mA cm <sup>-2</sup>	4000, 106%	163
Electrodeposition	FeCoSe <sub>2</sub> @NiCo-LDHs	2 M KOH	220.9 mAh g <sup>-1</sup>	1 A g <sup>-1</sup>	5000, 82.8%	168
Electrostatic interstratification	QD-Ti <sub>3</sub> C <sub>2</sub> Cl <sub>2</sub> @NiAl-LDHs	1 M KOH	2010.8 F g <sup>-1</sup>	1 A g <sup>-1</sup>	10000, 94.1%	180
Electrostatic interstratification	MXene/NiCo-LDHs	1 M (NH <sub>4</sub> ) <sub>2</sub> SO <sub>4</sub>	1207 F g <sup>-1</sup>	0.5 A g <sup>-1</sup>	5000, 93%	181
Exfoliative recombination	NCW-2	2 M KOH	736 C g <sup>-1</sup>	1 A g <sup>-1</sup>	5000, 86%	182
Alkaline etching	NTA18	1 M KOH	3483 mF cm <sup>-2</sup>	5 mA cm <sup>-2</sup>	3000, 37.9%	183
Microwave treatment	Ni-Co LDHs	1 M KOH	2369.0 F g <sup>-1</sup>	0.5 A g <sup>-1</sup>	—	184
In situ hydrolysis	CuCo-LDHs	1 M KOH	433 C g <sup>-1</sup>	1 A g <sup>-1</sup>	10000, 82.46%	185

---

**Table. 2 Properties of devices consisting of LDHs and its composites mentioned in this chapter.**

Devices	Electrolyte	Capacitance	Energy density at power density	Cycles	Ref.
NiFe-LDHs//NiFe-LDHs	2 M KOH	186 F g <sup>-1</sup> , 1 A g <sup>-1</sup>	66.13 Wh kg <sup>-1</sup> at 1483 W kg <sup>-1</sup>	—	125
NiCo-LDHs//AC	2 M KOH	186 F g <sup>-1</sup> , 1 A g <sup>-1</sup>	54.8 Wh kg <sup>-1</sup> at 374.9 W kg <sup>-1</sup>	10000, 80.8%	126
P@NiCo-LDHs//P@NiCo-LDHs	PBI-KOH	—	7.83 Wh kg <sup>-1</sup> at 300 W kg <sup>-1</sup>	10000, 80%	127
Zn <sub>0.25</sub> Ni <sub>0.75</sub> Co-LDHs-BA//AC	2 M KOH	65 mAh g <sup>-1</sup> , 1 A g <sup>-1</sup>	51.8 Wh kg <sup>-1</sup> at 789 W kg <sup>-1</sup>	10000, 94.6%	129
S-NiCoAl-LDHs//AC	PBI-KOH	182.6 F g <sup>-1</sup> , 0.5 A g <sup>-1</sup>	82.2 Wh kg <sup>-1</sup> at 450 W kg <sup>-1</sup>	10000, 92.5%	130
HC@NiCo-LDHs//AC	2 M KOH	148 C g <sup>-1</sup> , 0.4 A g <sup>-1</sup>	32.8 Wh kg <sup>-1</sup> at 320 W kg <sup>-1</sup>	4000, 70.2%	131
NiCoAl-LDHs@NiCo <sub>2</sub> S <sub>4</sub> @CC//AC	PVA-KOH	106 F g <sup>-1</sup> , 1 A g <sup>-1</sup>	33.13 Wh kg <sup>-1</sup> at 750 W kg <sup>-1</sup>	10000, 71.4%	142
CuBr <sub>2</sub> @NCC-LDHs/CF//AC	6 M KOH	118 F g <sup>-1</sup> , 0.4 A g <sup>-1</sup>	118 Wh kg <sup>-1</sup> at 1013 W kg <sup>-1</sup>	5000, 86.7%	147
NC/S-15//AC	2 M KOH	126.76 F g <sup>-1</sup> , 1 A g <sup>-1</sup>	43.6 Wh kg <sup>-1</sup> at 375 W kg <sup>-1</sup>	5000, 83%	148
NiCo <sub>2</sub> S <sub>4</sub> @NiMn-LDHs//AC	2 M KOH	96.23 F g <sup>-1</sup> , 50 mA cm <sup>-2</sup>	53.10 Wh kg <sup>-1</sup> at 370.82 W kg <sup>-1</sup>	10000, 94.3%	144

NiAl-LDHs-S//AC	6 M KOH	100.64 F g <sup>-1</sup> , 2 A g <sup>-1</sup>	35.78 Wh kg <sup>-1</sup> at 1127.03 W kg <sup>-1</sup>	10000, 104.37%	149
NiMn-LDHs/hrGO//Bi(OH) <sub>3</sub> /hrGO	2 M KOH	237.6 C g <sup>-1</sup> , 1 A g <sup>-1</sup>	59.9 Wh kg <sup>-1</sup> at 901.5 W kg <sup>-1</sup>	2000, 80.51%	145
CCO@NiCo-LDHs//AC	3 M KOH	37.67 F g <sup>-1</sup> , 0.5 A g <sup>-1</sup>	42.38 Wh kg <sup>-1</sup> at 1350 W kg <sup>-1</sup>	10000, 80%	146
Se-NiAl-LDHs//AC	6 M KOH	80 F g <sup>-1</sup> , 2 A g <sup>-1</sup>	29 Wh kg <sup>-1</sup> at 1593.17 W kg <sup>-1</sup>	5000, 95.24%	150
NiCoAl-LDHsN-9//AC	PVA-KOH	102.1 F g <sup>-1</sup> , 0.5 A g <sup>-1</sup>	35.9 Wh kg <sup>-1</sup> at 225.8 W kg <sup>-1</sup>	10000, 87.1%	140
NF@NiCo-LDHs//AC	3 M KOH	152.3 F g <sup>-1</sup> , 1 A g <sup>-1</sup>	51.1 Wh kg <sup>-1</sup> at 777 W kg <sup>-1</sup>	10000, 72.2%	143
Ag/CoAl-LDHs//N-CNTs	2 M KOH	275 C g <sup>-1</sup> , 1 A g <sup>-1</sup>	61.2 Wh kg <sup>-1</sup> at 800 W kg <sup>-1</sup>	10000, 92%	151
NiCo-LDHs@MoO <sub>3</sub> /NF//AC	2 M KOH	261.3 C g <sup>-1</sup> , 1 A g <sup>-1</sup>	58.06 Wh kg <sup>-1</sup> at 800 W kg <sup>-1</sup>	10000, 85.57%	161
NiCoFe-LDHs//AC	3 M KOH	207 F g <sup>-1</sup> , 1 mA cm <sup>-2</sup>	65 Wh kg <sup>-1</sup> at 83 W kg <sup>-1</sup>	5000, 126%	164
EGP@NiCo-LDHs//AC	2 M KOH	124.63 F g <sup>-1</sup> , 1 A g <sup>-1</sup>	44.31 Wh kg <sup>-1</sup> at 799.98 W kg <sup>-1</sup>	5000, 92.8%	165
O <sub>v</sub> -NiCo-LDHs//O <sub>v</sub> -NiCo-LDHs	3 M KOH	168.9 F g <sup>-1</sup> , 2 A g <sup>-1</sup>	216.19 Wh kg <sup>-1</sup> at 1.75 kW kg <sup>-1</sup>	2000, 71.45%	166

MoO <sub>3-x</sub> @NiCo-LDHs//MoO <sub>3-x</sub> @NiCo-LDHs	0.5 M K <sub>2</sub> SO <sub>4</sub>	0.45 F cm <sup>-2</sup> , 2 mA cm <sup>-2</sup>	0.047 mWh cm <sup>-2</sup> at 0.865 mW cm <sup>-2</sup>	—	162
MnCo <sub>2</sub> O <sub>4</sub> @NiCo-LDHs/NF//AC	6 M KOH	60 F g <sup>-1</sup> , 0.2 A g <sup>-1</sup>	21.3 Wh kg <sup>-1</sup> at 160.0 W kg <sup>-1</sup>	5000, 86.6%	167
NiCo-LDHs@Ni-NTNW//AC	1 M KOH	64.9 F g <sup>-1</sup> , 1 mA cm <sup>-2</sup>	14.7 mWh cm <sup>-2</sup> at 4769 mW cm <sup>-2</sup>	20000, 120%	163
FeCoSe <sub>2</sub> @NiCo-LDHs//PPC-2	2 M KOH	95.2 mAh g <sup>-1</sup> , 1 A g <sup>-1</sup>	1.248 kW kg <sup>-1</sup> at 65.9 Wh kg <sup>-1</sup>	10000, 87.6%	168
NCW-2//rGO	2 M KOH	120 F g <sup>-1</sup> , 2 A g <sup>-1</sup>	43 Wh kg <sup>-1</sup> at 1.3 kW kg <sup>-1</sup>	10000, 89%	182
NTA18//AC	1 M KOH	126 F g <sup>-1</sup> , 1 A g <sup>-1</sup>	45.1 Wh kg <sup>-1</sup> at 16000 W kg <sup>-1</sup>	5000, 59%	183
Ni-Co LDHs//AC	1 M KOH	68.1 F g <sup>-1</sup> , 0.5 A g <sup>-1</sup>	21.28 Wh kg <sup>-1</sup> at 375.09 W kg <sup>-1</sup>	10000, 83.6%	184
CuCo-LDHs//AC	1 M KOH	76 F g <sup>-1</sup> , 1 A g <sup>-1</sup>	22 Wh kg <sup>-1</sup> at 23200 W kg <sup>-1</sup>	10000, 91.3%	185

### 3. Modification method of hybrid LDHs

The modification of LDHs is particularly important for solving disadvantages including low specific capacitance and poor cycling stability, which can be carried out based on the various synthetic methods described earlier, starting from the basic properties of the material and modifying it compositionally and structurally to improve its performances in electrochemical applications.<sup>186-189</sup> Since LDHs have a 2D layered structure, compounding with various 1D and 2D nanomaterials such as carbon nanotubes, graphene and MoS<sub>2</sub> is highly feasible, and the addition of polymerase also enhances the conductivity.<sup>190-192</sup> In hybridized LDHs nanostructures, the construction of ionic vacancy defects<sup>193, 194</sup> and porous structures can alter crystalline shape and increase active sites, allowing for a superior level of electrochemical performances. In addition, metal sapphire and phosphides have higher metallic properties than LDHs, and LDHs can be modified with them to form composites.<sup>195, 196</sup> In general, the improved performances of hybrid nanostructures result from the synergistic effect of heterogeneous interface formed between LDHs and other objects. In this chapter the modification methods for hybridized LDHs nanostructures are divided into four categories: addition of components, construction of defects, generation of heterogeneous structures and direct generation on the substrate.<sup>197, 198</sup> All these methods provide a larger surface area and expose a greater number of active sites. It is important to note, however, that each method provides different structural effects, which have a different impact on the electrochemical properties of the hybridized LDHs.

### 3.1 Addition of components

The addition of other components to the original LDHs can change the composition and structure of the material.<sup>199</sup> This behavior during the synthesis processes can increase the synergy between the substances and can also modify the structure of materials, and some intercalation substances can also improve the electrochemical properties.<sup>200-204</sup> However, the application of this modification method needs to consider the force between raw materials. A certain theoretical study for this method can have an unexpected effect.

The preparation of composites with different components is a meaningful route to obtain new and efficient electrode materials. Ma et al.<sup>205</sup> prepared Ni-embedded carbon nanofibers/NiAl-LDHs hybrids. Firstly, Ni-containing carbon nanofibers were skillfully fabricated via electrostatic spinning and thermal treatment, which provided many active sites and increased the space for ion transport. Subsequently, Ni-embedded carbon nanofibers were combined with nanostructured NiAl-LDHs by hydrothermal method (Fig. 12 (a)). The results showed that the former could optimize the microstructure of NiAl-LDHs, alleviate their aggregation and improve the multiplicative performances of NiAl-LDHs. 3% Ni-embedded carbon nanofibers/NiAl-LDHs (3%-Ni-C/NiAl-LDHs) achieved a 1228.2 C g<sup>-1</sup> specific capacitance at 1 A g<sup>-1</sup> (Fig. 12 (b)). The lifetime achieved an initial capacity retention of 88.6%. Besides, an asymmetric supercapacitor device was assembled with an energy density of 74.9 Wh kg<sup>-1</sup> at 800 W kg<sup>-1</sup>. Notably, the device achieved a 91.4% capacity after 10000 cycles at 6 A g<sup>-1</sup> (Fig. 12 (c)).

NiCo-LDHs have layer spacing and a high ion exchange capacity, but poor electrical conductivity, severe agglomeration and structural defects limit their energy storage capacity. Wu et al.<sup>87</sup> prepared zeolite imidazole framework-67 (ZIF-67) sulfur-doped NiCo-LDHs and polypyrrole nanotube composites (NiCo-LDHs-S/PNTs) for the first time by electrospinning and hydrothermal methods (Fig. 12 (d)). The 1D hollow polypyrrole with high aspect ratio provides straight charge-transfer routes and abundant contacts with electrolyte. When the sulfur content is 7%, the specific capacitance of NiCo-LDH-S/PNTs is 1936.3 F g<sup>-1</sup>. The device assembled by graphene anode and NiCo-LDH-S/PNT cathode achieves an energy density of 16.28 Wh kg<sup>-1</sup> at 650 W kg<sup>-1</sup>. And the capacity retention rate reaches 74% after 8000 cycles.

Changes in the anions between the layers also influence the resulting performances. The layer spacing of different anion intercalated LDHs can vary, while a larger layer spacing facilitates contact between the active atoms on the LDHs plate layer and OH<sup>-</sup>, resulting in improved electrochemical properties. A spherical NiAl-Cl LDHs with chloride ions as interlayer anions was prepared by Lv et al.<sup>206</sup> with a specific capacitance of 2512 F g<sup>-1</sup> at 1 A g<sup>-1</sup>. NiAl-Cl LDHs has a wider interlayer spacing, which promotes contact between the active atoms of the hydro magnesite-like layers and OH<sup>-</sup>, improves electron transport kinetics, increase the utilization of the active material and have better multiplicative performance (the specific capacitance at 20 A g<sup>-1</sup> is 77.5% of that at 1 A g<sup>-1</sup>). At the same time, the gaps between the interlaced hierarchical structures facilitate the



buffering of volume changes during the reaction, ensuring the structural stability of NiAl-Cl LDHs during the redox reaction. They were also compared to materials with carbonate ions as interlayer anions, and the results showed superior performances of NiAl-Cl LDHs (Fig. 12 (g)). The energy density of the prepared NiAl-Cl LDHs//AC asymmetric supercapacitor was  $53.9 \text{ Wh kg}^{-1}$  at  $1540 \text{ W kg}^{-1}$  and maintained 94.1% specific capacitance experiencing 1000 cycles.

Deng et al.<sup>207</sup> used hydrothermal method to prepare benzoate anion intercalated nickel-doped inorganic organic cobalt hydroxide ultrathin nanoribbons Ni-Co(OH)(BA) without the use of binders and surfactants, and the electrochemical performance was effectively improved due to the large interlayer distance and enhanced ion flow efficiency. The results show a  $1664 \text{ F g}^{-1}$  specific capacitance at  $5 \text{ A g}^{-1}$  (Fig. 12 (h)) and a 83% capacity retention undergoing 8000 cycles. At the same time, the composed Ni-Co(OH)(BA)//AC asymmetric supercapacitor device was able to provide a  $47.5 \text{ Wh kg}^{-1}$  energy density at  $850 \text{ W kg}^{-1}$  and a 91% capacity retention after 8000 cycles. Saber et al.<sup>208</sup> inserted silicon into Co-LDHs nanospheres to form Si/Co-LDHs nanofibers by inserting cyanate anions as the backbone for building the nanospheres. The structure can be tuned through controlling the preparation conditions and Si content to further improve the properties. The results show that morphological changes from nanoparticles or flat plates to nanofibers enhance the specific capacitive performances of Si/Co-LDHs. The specific capacitance was increased to  $621.5 \text{ F g}^{-1}$  and the cycling stability was 84.5%. The outcomes

can be explained by the properties of the nanofibers morphology and the cooperation effect from capacitive properties of Si and pseudocapacitive properties of C.

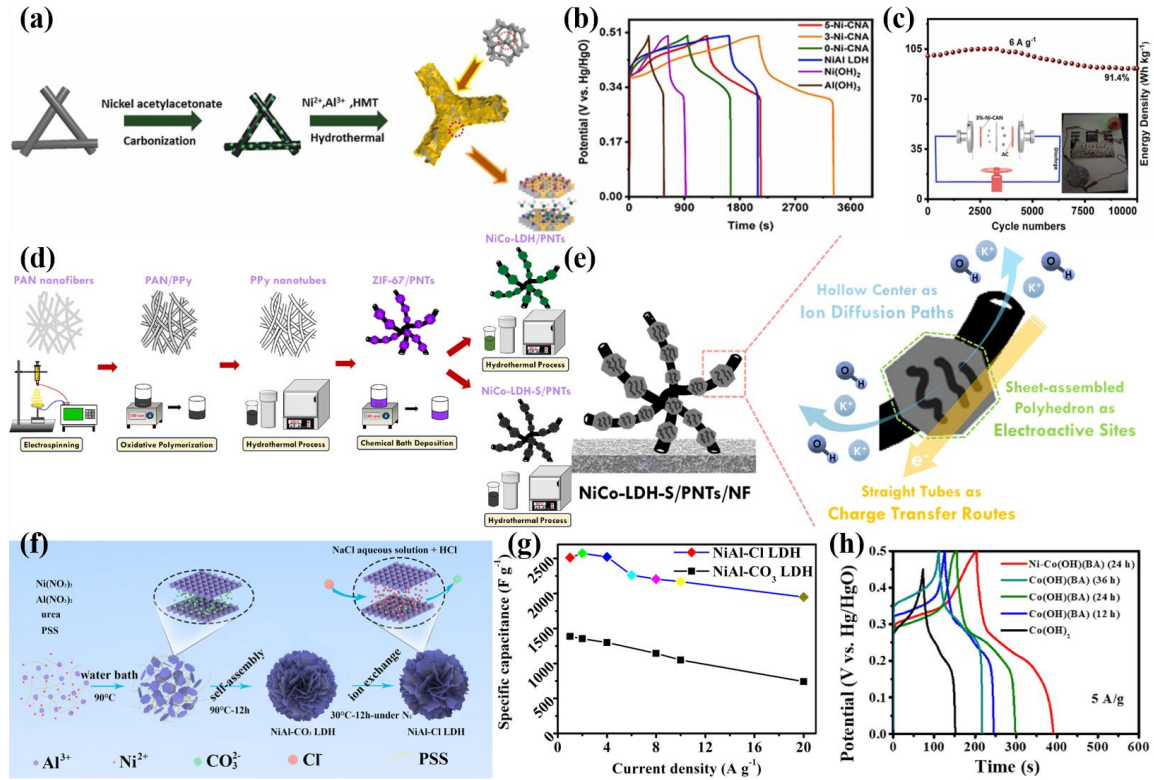


**Fig. 12** (a) Detailed preparation strategy for obtaining hierarchical structure Ni-CAN, (b) the GCD curves of the as-obtained samples at  $1 \text{ A g}^{-1}$  with the potential window of 0-0.5 V, (c) cycling performance of 3%-Ni-C/NiAl-LDHs//AC at  $10 \text{ A g}^{-1}$ .<sup>205</sup> Copyright 2022, Elsevier B.V. (d) Illustration of synthesizing processes for NiCo-LDHs/PNTs and NiCo-LDHs-S/PNTs, (e) illustration of morphology features for NiCo-LDHs-S/PNTs/NF.<sup>87</sup> Copyright 2022, Elsevier Inc. (f) Specific capacitance of NiAl- $\text{CO}_3$  LDHs and NiAl-Cl LDHs electrodes at a variety of current densities. (g) Specific capacitance of two electrodes at different current densities<sup>206</sup> Copyright 2022, Elsevier Ltd. (h) GCD curves of those electrodes at a current density of  $5 \text{ A g}^{-1}$ .<sup>207</sup> Copyright 2022, Elsevier Ltd.

The size of the layer spacing of LDHs is one of the key factors affecting their electrochemical properties, and increasing the layer spacing by suitable methods can greatly improve the performances. The composites based on Ni-Cr-LDHs and polyoxotungstate nanoclusters (Ni-Cr-LDHs-POW) were fabricated by Padalkar et al.<sup>182</sup> using exfoliative recombination. The interlayer intercalation hybridization of POW nanoclusters in Ni-Cr-LDHs forms the cumulate frame (Fig. 13 (a)) and significantly enlarges the spacing between layers. An NCW-2//rGO AHSC device (Fig. 13 (b)) was assembled with Ni-Cr-LDHs-POW nanohybrid material as the positive electrode. The energy density at 1.32 kW kg<sup>-1</sup> is 34 Wh kg<sup>-1</sup>, and the capacitance retention after 10000 charge-discharge cycles is 86%. Mahmood et al.<sup>209</sup> designed a unique synthesis strategy based on polyaniline-doped 2D cobalt-iron LDHs (CoFe-LDHs/P) nanomaterial. The results show that, among all polymers, the optimal concentration of polyaniline forms nanopores on the CoFe-LDHs nanoflakes. The ordered pores increase redox sites and promote the efficient movement of ions. The optimized CoFe-LDHs/P2 displays a 1686 F g<sup>-1</sup> specific capacitance at 1 A g<sup>-1</sup> (Fig. 13 (d)) and exhibits excellent cycle (98% over 10000 cycles). Furthermore, an asymmetric aqueous device (CoFe-LDHs/P2//AC) was prepared with an energy density of 75.9 Wh kg<sup>-1</sup> at 1124 W kg<sup>-1</sup>, as well as 97.5% stability in 10000 cycles.

Deng et al.<sup>210</sup> have synthesized a hierarchical array of scaled trimetallic hydroxides (CuCoNi-OH) under a moderate alkaline hydrolysis strategy through rational

nanostructure design using a bimetallic 2D zeolite imidazole framework (CuCo-ZIF-L) as a template (Fig. 13 (g)). The hierarchical porous structure provides large active site exposure and rapid ion diffusion, and the synergistic multi-metal effect provides high electrical conductivity and favors redox conversion, facilitating the electrochemical kinetics of the supercapacitor. As a battery-type electrode, the CuCoNi-OH electrode possesses a specific capacitance of  $821.6 \text{ C g}^{-1}$  at  $1 \text{ A g}^{-1}$  and a capacity retention of 89.8% at  $20 \text{ A g}^{-1}$  (Fig. 13 (e)). The assembled device has a remarkable energy density and power density. The strategy is universal in the preparation of bimetallic ZIF-L and the corresponding metal hydroxides and provides an effective approach to rationally design electrochemical storage and conversion materials. Wang et al.<sup>183</sup> synthesized NiTiAl-LDHs by adding a trace amount of Al to the NiTi-LDHs substrate layer and then etching some Al with sodium hydroxide solution, resulting in higher specific surface area, specific capacitance and rate property. The specific surface area of the samples after 18 h etching reached  $203 \text{ m}^2 \text{ g}^{-1}$  and the specific capacitance at  $5 \text{ mA cm}^{-2}$  was up to  $3483 \text{ mF cm}^{-2}$  (Fig. 13 (f)), and better structural stability than that of the NiTi-LDHs. The hybrid devices assembled from the etched samples exhibited an energy density of  $45.1 \text{ Wh kg}^{-1}$  at  $16000 \text{ W kg}^{-1}$ . This alkaline etching method can improve the porosity of aluminum-containing layered dihydroxy talc, promote the specific capacitance and rate performance, and has a more promising application.

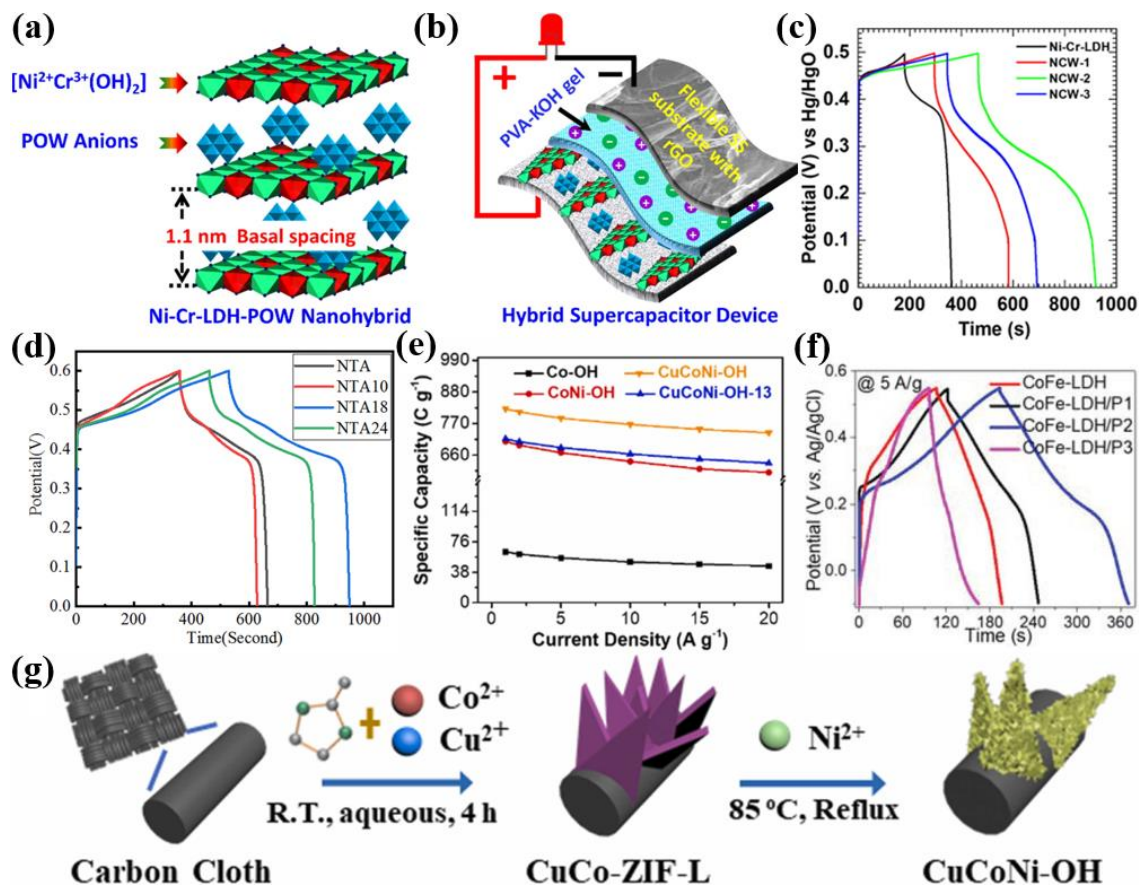


Fig. 13 (a) Structural schematic model of the NCW nanohybrid, (b) NCW-2//rGO AHSC assembly diagram, (c) GCD curves of pristine Ni-Cr-LDHs and NCW nanohybrids at 1 A g<sup>-1</sup>.<sup>182</sup> Copyright 2022, Elsevier Inc. (d) GCD curves for different materials at 5 mA cm<sup>-2</sup>.<sup>183</sup> Copyright 2021, Elsevier B.V. (e) Corresponding specific capacitance of hydroxide electrodes at 1-20 A g<sup>-1</sup>.<sup>209</sup> Copyright 2022, Elsevier B.V. (f) GCD curves of CoFe-LDHs/P2 electrode.<sup>210</sup> Copyright 2022, Wiley-VCH GmbH. (g) schematic of the synthesis procedures of CuCo-ZIF-L and CuCoNi-OH.<sup>209</sup> Copyright 2022, Elsevier B.V.

The rational design of highly porous structures with large specific surface areas to facilitate ion/electron transport and insertion/de-insertion is an effective route to improve

electrochemical redox reactions in materials. However, challenges are existed such as unsatisfactory energy storage due to the simplicity of the porous structure and severe performance degradation during long-term electrochemical cycling remain. Inspired by the natural geographical structure of forests, Liu et al.<sup>211</sup> designed a Ni/Co-LDHs on a metal-organic framework of ZnO nanotubes grown on transparent conducting substrates with different porous structures to simulate a “rock-soil-tree-leaf” system (Fig. 14 (a)). Due to the high specific surface area of 3D ZnO@Ni/Co-LDHs, the enhanced OH<sup>-</sup> trapping ability of ZnO, the enhanced electrochemical activity due to Ni/Co doping, and the hybrid charge storage behavior, excellent specific capacitance and durability are achieved. Of the five ZnO@Ni/Co-LDH films, LDH-3 exhibits remarkable conductivity and energy storage performances, with a charge capacity of 507.2 C g<sup>-1</sup> at 0.1 mA cm<sup>-2</sup> and a capacity retention of 72.1% after 10000 cycles, and LDH-3-based devices have excellent durability, with an energy density of 7.7 uWh cm<sup>-2</sup> at 375.0 pW cm<sup>-2</sup>. The prepared ZnO@Ni/Co-LDHs device allows for automatic optical switching through solar energy harvesting and charge storage/release. These new insights will pave the way for the next generation of smart technologies towards a sustainable and habitable future.

Zhou et al.<sup>212</sup> synthesized ultrathin cobalt-nickel-magnesium LDHs (CoNiMg-LDHs) nanosheets with abundant oxygen vacancies at room temperature through a sacrificial magnesium-based replacement reaction (Fig. 14 (b)). The self-doping and the mild reduction of magnesium improve the concentration of oxygen vacancies, improve the

electrochemical charge transfer efficiency, and enhance the adsorption capacity of the electrolyte. Density functional theory (DFT) calculations indicate the  $\text{Mg}^{2+}$  doping reduces the generation energy of oxygen vacancies, thereby increasing the concentration of oxygen vacancies. Moreover, the CoNiMg-LDH//AC device exhibits a specific capacitance of 333  $\text{C g}^{-1}$  at 1  $\text{A g}^{-1}$  and an energy density of 73.9  $\text{Wh kg}^{-1}$  at 0.8  $\text{kW kg}^{-1}$ . After 5000 cycles, there is only 13% capacity loss. This finding highlights the positive role of Mg in regulating oxygen vacancies for enhanced supercapacitor performances, which is beneficial to expand the range of high-quality supercapacitors active materials. Wang et al.<sup>213</sup> achieved high loading and high capacitance performance by one-step hydrothermal loading of NiMn-LDHs on NF using sodium dodecyl sulfate (SDS) as an intercalator and soft template. The electrode added with 4 mM SDS had an area capacitance of up to 6311  $\text{mF cm}^{-2}$  at 5  $\text{mA cm}^{-2}$ . The hybrid supercapacitor assembled with this electrode had an energy density of 34.61  $\text{Wh kg}^{-1}$  at 831  $\text{W kg}^{-1}$  and a capacitance retention of 129% at 4  $\text{A g}^{-1}$  for 5000 cycles and 85% for 10000 cycles at 10  $\text{A g}^{-1}$ . Li et al.<sup>214</sup> successfully fabricated soluble graphite nitride (SCN) nanosheets NiFe-LDHs by electrostatic self-assembly (Fig. 14 (d)) as a one-layer high performance electrode (NiFe-LDHs@SCN) for supercapacitors. The optimized structure has a specific capacitance of 1060.4  $\text{F g}^{-1}$  at 1  $\text{A g}^{-1}$ . The prepared hybrid supercapacitor has an energy density of 68.7  $\text{Wh kg}^{-1}$  at 827.5  $\text{W kg}^{-1}$  and has a 83.3% capacitance after 8000 cycles.



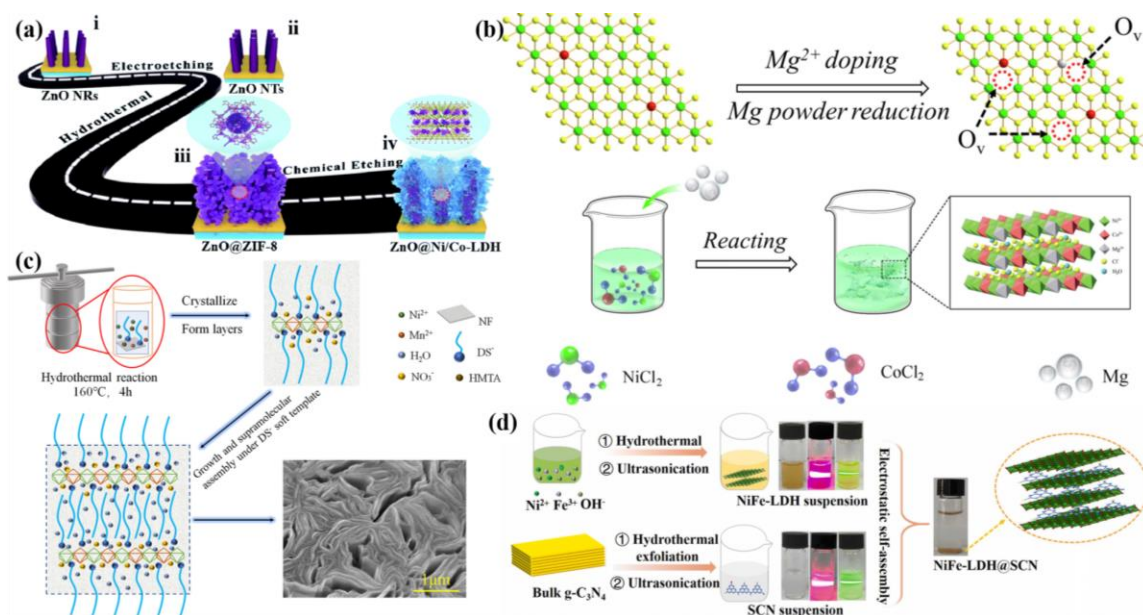


Fig. 14 (a) Synthesis scheme of the ZnO@Ni/Co-LDHs film.<sup>211</sup> Copyright 2022, Royal Society of Chemistry. (b) Schematic illustration of the fabrication strategy of oxygen-vacancies abundant CoNiMg-LDHs.<sup>212</sup> Copyright 2021, Elsevier Inc. (c) Growth mechanism of LDH with SDS as a soft template.<sup>213</sup> Copyright 2022, Elsevier Ltd. (d) The synthetic process of the NiFe-LDH@SCN.<sup>214</sup> Copyright 2022, Elsevier B.V.

### 3.2 Manufacturing defects in materials

Constructing defects is another promising approach to improve the electrochemical properties of LDHs as it modulates the electronic structure and increases the active sites.

<sup>215</sup> The method can endow the materials more hole structure, facilitating the electrolyte to enter the electrode materials. However, the condition of this method is difficult to control, and it is prone to form excessive defects. Hence, it is used to construct material defects by selecting suitable raw materials and controlling conditions. Chu et al.<sup>185</sup> chose Cu element as a dopant to prepare CuCo-LDHs. The prepare structure was grown onto NF by in situ

hydrolysis. Electron images of CuCo-LDHs are shown in Fig. 15 (a, b). The addition of Cu obviously increases the density of local electron density, thereby improving electronic conductivity and facilitating charge transfer. CuCo-LDHs electrodes provide excellent capacitive performance (Fig. 15 (c, d)). The CuCo-LDHs//AC device showed a  $22 \text{ Wh kg}^{-1}$  energy density of  $22 \text{ Wh kg}^{-1}$  and a 91.3% stability after 10000 cycles. This study has structurally tuned the LDHs material to construct lattice defects to modify their performances, which have a very positive effect on the preparation of superior supercapacitor electrode materials in the future.

Lei et al.<sup>216</sup> have synthesized NiCo-LDHs/NF (D-NiCo-LDHs/NF) based on the memory effect (Fig. 15 (e)). DFT calculations reveal that Co vacancies induce more electrons to approach Fermi energy level, thereby improving conductivity and favoring transfer of charge. SEM image in Fig. 15 (f) shows the microscopic morphology of D-NiCo-LDHs/NF, and the surface of NF is uniformly covered by vertically aligned NiCo-LDHs nanosheets. The synthesized D-NiCo-LDHw/NF has a  $3200 \text{ F g}^{-1}$  specific capacitance at  $1 \text{ A g}^{-1}$  (Fig. 15 (g, h)). The asymmetric supercapacitor achieved an energy density of  $53 \text{ Wh kg}^{-1}$  at  $752 \text{ W kg}^{-1}$  and a retention rate of 94.7% experiencing 5000 cycles. Yang et al.<sup>217</sup> firstly transformed 2D dense CoAl-LDHs to 3D loosely stacked CoZnAl-LDHs using  $\text{Zn}^{2+}$  doping to induce LDHs morphological changes (Fig. 15 (i, j)). In addition, the partial dissolution of Zn/Al double ions between the LDHs lamellae in alkaline solution resulted in a large change in the electronic environment of the Co surface and the

generation of a certain concentration of oxygen defects in CoZnAl-LDHs. This case improves multiplicative performance and cycling stability of CoZnAl-LDHs nanosheets. Compared to unetched CoZnAl-LDHs, E-CoZnAl-LDHs-8 h has a  $946 \text{ F g}^{-1}$  specific capacitance at  $1 \text{ A g}^{-1}$  (Fig. 15 (k)) and a 92.3% cycle life undergoing 4000 cycles) The E-CoZnAl-LDHs-8 h//AC asymmetric supercapacitor was prepared with an energy density of  $36.75 \text{ Wh kg}^{-1}$  at  $400 \text{ W kg}^{-1}$  and a 72.7% cycle life experiencing 8000 cycles. The "doping" and "double ion etching" strategies proposed in this study provide theoretical guidance and experimental basis to develop supercapacitors with excellent properties.

Porous structures and surface defects are important factors in improving the performance of supercapacitors. Zhong et al.<sup>218</sup> prepared NiCo-SDBS-LDHs by a one-step hydrothermal method using sodium dodecylbenzene sulfonate (SDBS) as the anionic surfactant. Then, 3D connected porous flower-like 3D-NiCo-SDBS-LDH microspheres were designed and synthesized using the gas-phase hydrazine hydrate reduction method (Fig. 15 (l)). The results show that hydrazine hydrate reduction not only introduces many pores, giving rise to the formation of oxygen vacancies, but also roughs up the surface of the microspheres (Fig. 15 (m)). All these changes contribute to the electrochemical activity of 3D-NiCo-SDBS-LDHs, the specific capacitance is  $1148 \text{ F g}^{-1}$  at  $1 \text{ A g}^{-1}$  (Fig. 15 (n)) (about 1.46 times than that of NiCo-SDBS-LDH), and the retention rate after 4000 cycles is 94%. In addition, the assembled 3D-NiCo-SDBS-LDHs//AC device has an energy density of  $800 \text{ W kg}^{-1}$  at  $73.14 \text{ Wh kg}^{-1}$  and a cycle life of 95.5% undergoing 10000 cycles.

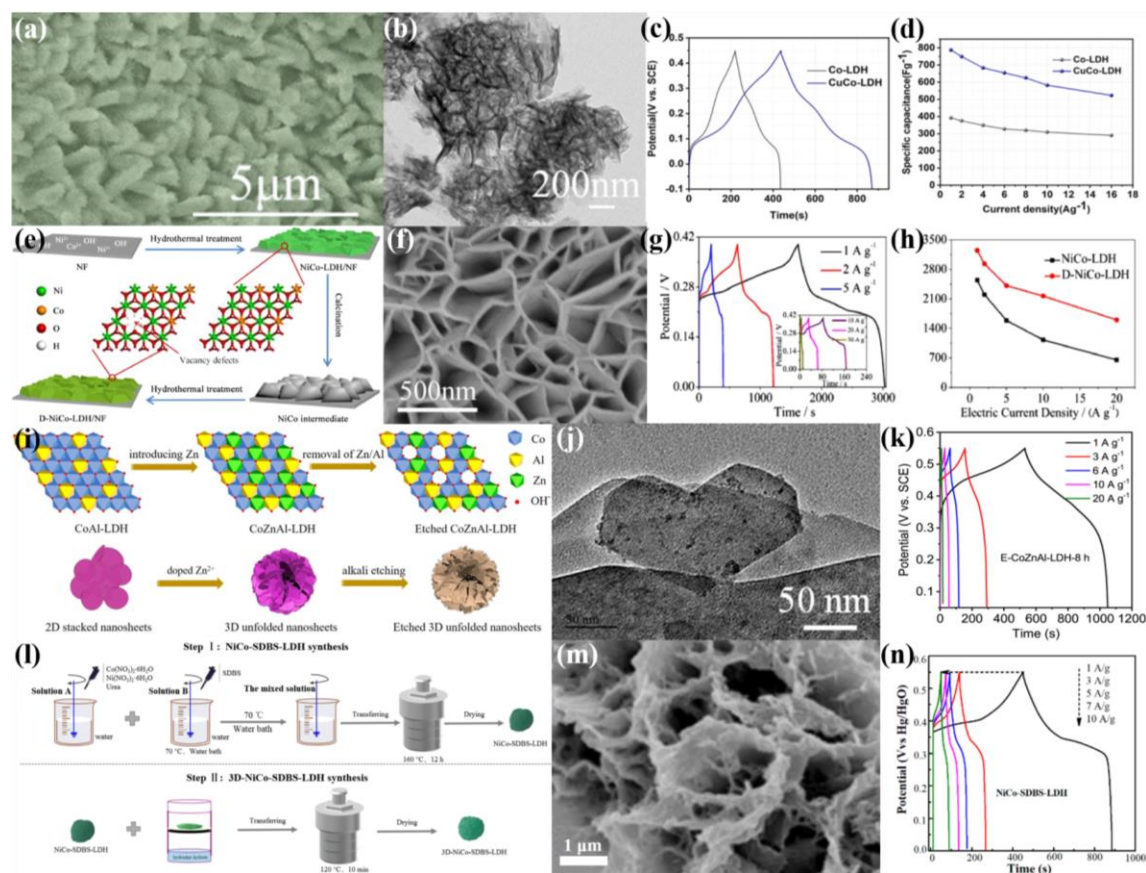


**Fig. 15** (a) SEM image of CuCo-LDHs, (b) TEM image of CuCo-LDHs, (c) GCD curves, and (d) rate capability of Co-LDHs and CuCo-LDHs.<sup>185</sup> Copyright 2022, American Chemical Society. (e) Schematic illustration of introducing vacancy defects to NiCo-LDHs through the memory effect, (f) SEM image of D-NiCo-LDHs/NF nanosheet arrays, (g) GCD curves of the D-NiCo-LDHs/NF electrode at different current densities, (h) capacitance retention of D-NiCo-LDHs/NF and NiCo-LDHs/NF electrodes at different current densities.<sup>216</sup> Copyright 2022, Elsevier Ltd. (i)  $\text{Zn}^{2+}$  doped induced morphological change in CoAl-LDHs and Al/Zn dual ion etching of CoZnAl-LDHs in alkaline solution, (j) TEM image of E-CoZnAl-LDHs-8 h, (k) GCD curves of E-CoZnAl-LDHs-8 h at different scan rates and current densities.<sup>217</sup> Copyright 2022, Elsevier Ltd. (l) Diagram of the synthesis of 3D-NiCo-SDBS-LDHs, (m) SEM of 3D-NiCo-SDBS-LDHs at different magnifications,

**(n) GCD curves of NiCo-SDBS-LDHs at different scan rates and current densities<sup>218</sup> Copyright 2022, MDPI.**

For electrochemical materials, domain boundaries are considered to work as active sites because of their defect enrichment. Nevertheless, LDHs are easy to form single-crystal nanosheets caused by the 2D lattice.<sup>219</sup> Many researches have been done in designing layered structures for providing abundant active sites and speeding up mass transfer.<sup>220</sup> Ban et al.<sup>220</sup> proposed a method to introduce low-angle grain boundaries (LAGB) in NiCo-LDHs flakes. The defect-rich nanoflakes were ultimately construct cages with hollow structure (Fig. 16 (a)). Both the hierarchical structure and the formation of grain boundaries are explained by the  $\text{Ni}^{2+}/\text{Co}^{2+}$  ratio during "etch growth". Domain boundary defects also bring about the preferential formation of oxygen vacancies. In addition, DFT calculations show that Co substitution plays a decisive role in fabricating lattice defects and forming domain boundaries. The prepared NiCo-LDHs-2 electrode material showed a significant increase in specific capacitance to  $899 \text{ C g}^{-1}$  at  $1 \text{ A g}^{-1}$ . The maximum energy density of the NiCo-LDHs-2//AC asymmetric capacitor was  $101.1 \text{ Wh kg}^{-1}$  at  $1.5 \text{ kW kg}^{-1}$ .

Designing metal cation defects with the desired structure is a major challenge to improve electrochemical performances. Wu et al.<sup>215</sup> designed ultrathin ZnNi-LDHs nanosheets with Zn-rich vacancies uniformly anchored on a CuO nanowire backbone as high-performance capacitive electrodes by a zeolite imidazolium salt framework-8

derivatization method (Fig. 16 (b)). The optimized  $V_{Zn}$ -deficient electrode achieved an area capacity of  $3967 \text{ mF cm}^{-2}$  at  $2.0 \text{ mA cm}^{-2}$ . Moreover, the maximum energy density of the device composed of  $V_{Zn}$ -deficient samples and AC was  $1.03 \text{ mWh cm}^{-3}$  and the power density was  $9.3 \text{ mW cm}^{-3}$ . The mechanistic study showed that  $V_{Zn}$  modulated the electronic structure of the ZnNi-LDHs nanosheets sheets, promoting the electronic conductivity and surface Faraday reaction. This work reveals the role of metal cation defects in influencing the electrochemical activity at the atomic level. Coincidentally, Kim et al.<sup>221</sup> developed a lattice engineering route for concurrently controlling the defect and the porosity via tuning the elastic deformation and the chemical interactions of the nanosheets in restacking. The increase in intercalation size and reduction in charge density effectively increases the oxygen vacancy content and improves the porosity amount. The defect-rich Co-Al-LDHs- $\text{NO}_3$ -nanohybrids exhibit excellent performances as electrodes with a  $2230 \text{ F g}^{-1}$  specific capacitance of  $2230 \text{ F g}^{-1}$  at  $1 \text{ A g}^{-1}$ . Combined with DFT calculations, the observed good correlation between overpotential (capacitance) and defect content (stacking) number highlights the significance of the defect (stacking) structure in the optimization of energy function. Zhang et al.<sup>222</sup> prepared oxygen-rich 3D  $\text{Co}_{0.50}\text{-Ga}_{0.50}$ -LDHs assembled in porous ultra-thin nanosheets using a simple one-step method (Fig. 16 (c)). This synthetic strategy introduced many holes in the ultrathin LDHs nanosheets, resulting in a high concentration of oxygen vacancies in  $\text{Co}_{0.50}\text{-Ga}_{0.50}$ -LDHs. The synergistic effect of the oxygen vacancies and the introduced Ga ions enhances the adsorption of  $\text{OH}^-$  by the LDHs nanosheets,

conferring Co<sub>0.50</sub>-Ga<sub>0.50</sub>-LDHs with excellent properties for supercapacitors. The prepared LDHs achieve a specific capacitance of 0.62 C cm<sup>-2</sup> at 10 mV s<sup>-1</sup>. The Co<sub>0.50</sub>-Ga<sub>0.50</sub>-LDHs//AC asymmetric supercapacitors have excellent energy density and service life. This discovery also promotes the wider application of porous ultra-thin LDHs nanosheets in energy storage and other fields.



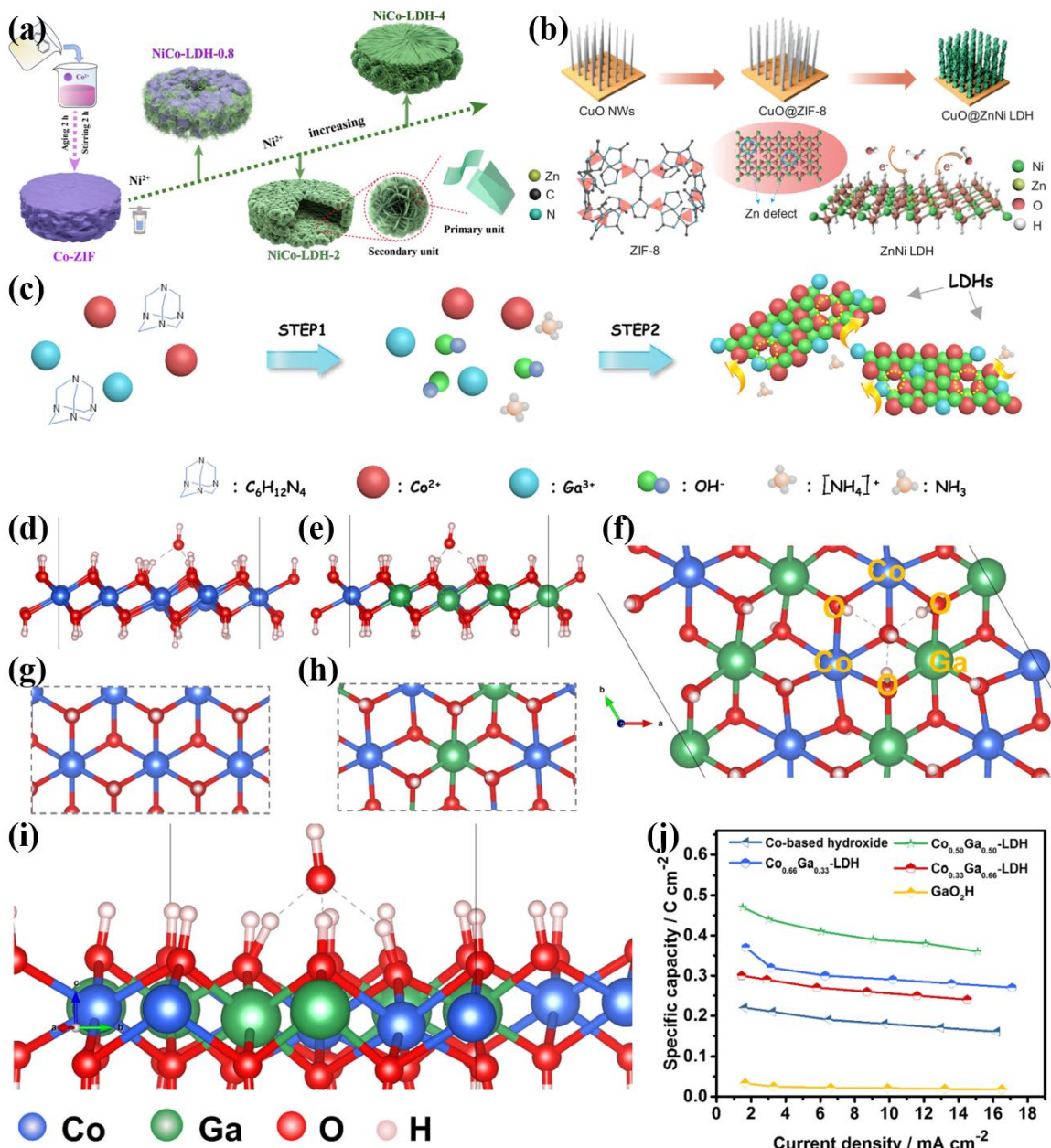


Fig. 16 (a) Synthesis strategy of NiCo-LDHs.<sup>220</sup> Copyright 2022, Springer. (b) Schematic illustration of the fabrication procedures of the hierarchical ZnNi-LDHs architectures with rich  $\text{V}_{\text{Zn}}$  through ZIF-derived method.<sup>215</sup> Copyright 2021, Elsevier Ltd. (c) Synthesis mechanism of defect-rich porous ultrathin LDHs, the crystal structure and adsorption sites on the side and top views of (d, g) bulk Co-LDHs, (e, h) bulk Co-Ga-LDHs and (f, i) oxygen defect-rich  $\text{Co}_{0.50}\text{-Ga}_{0.50}$ -

LDHs, (j) Rate performance of GaOOH, Co-based hydroxide and Co<sub>x</sub>-Ga<sub>y</sub>-LDHs electrodes.<sup>222</sup>

Copyright 2021, Elsevier Inc.

### 3.3 Generation of heterogeneous structures

The construction of heterogeneous structures is another important strategy to enhance the electrochemical properties of LDHs. The interfacial regions of heterogeneous can provide opportunities to enrich the number of active sites<sup>223</sup> and promote electron transfer.<sup>224, 225</sup> And strong electronic interactions in the heterogeneous interfaces facilitate the enhancement of electronic and ionic conductivity<sup>226</sup> and redox reaction kinetics.<sup>227</sup> However, the tightness of the heterogeneous interface is difficult to control, and the existence of voids between the interfaces affects the electrochemical properties. Adding certain ingredients such as binders in the synthesis process might solve the tightness problem. Luo et al.<sup>228</sup> have successfully synthesized layered NiCo<sub>2</sub>O<sub>4</sub>@NiFe-LDHs heterostructures by sequential hydrothermal methods, heat treatment and electrodeposition, as positive electrodes for high-performance supercapacitors. In this unique structure, on the one hand, NiCo<sub>2</sub>O<sub>4</sub>, which acts as a scaffold, provides high conductivity, thus accelerating transfer of electron. On the other hand, the NiFe-LDHs nanosheets have high surface area, providing an abundance of active sites for electrochemical reactions. The 3D layered structure is also more conducive to diffuse electrolyte ions, and SEM images are displayed in Fig. 17 (a). Thus, the synergistic effect between NiCo<sub>2</sub>O<sub>4</sub> and NiFe-LDHs confers the best NiCo<sub>2</sub>O<sub>4</sub>@NiFe-LDHs-150/CC with excellent electrochemical

performances including good area specific capacitance ( $1.09 \text{ F cm}^{-2}$  at  $1 \text{ mA cm}^{-2}$ ) (Fig. 17 (b, c)), small charge transfer resistance ( $0.35 \Omega$ ) and excellent cycling stability.

Huang et al.<sup>161</sup> obtained a unique array of intercalated pseudocapacitive properties and battery-type electrode materials LDHs nanosheets by a simple and pollution-free two-step electrodeposition technique. The electrode material consists of  $\text{MoO}_3$  and NiCo-LDHs grown directly on a 3D conductive NF substrate to form a binder-free 2D ultrathin cross-layered heterogeneous structure ( $\text{NiCo-LDHs@MoO}_3/\text{NF}$ ). This heterojunction exhibited a  $952.2 \text{ C g}^{-1}$  specific capacitance at  $1 \text{ A g}^{-1}$  and a 86.42% capacity retention experiencing 10000 cycles at  $20 \text{ A g}^{-1}$ . Wang et al.<sup>167</sup> prepared a core-sheath heterostructure ( $\text{MnCo}_2\text{O}_4@\text{NiCo-LDHs}/\text{NF}$ ) consisting of NiCo-LDHs encapsulating  $\text{MnCo}_2\text{O}_4$  nanowires on a NF substrate. As shown in Fig. 17 (d), the core-sheath structure with a diameter of about 65 nm were anchored on the NF backbone. NiCo-LDHs nanosheets as the sheath material. This heterogeneous structure combines the advantages of the interconnection between NiCo-LDHs nanosheets, the high electrical conductivity and mechanical strength of  $\text{MnCo}_2\text{O}_4$ . Moreover, the  $\text{MnCo}_2\text{O}_4@\text{NiCo-LDHs}/\text{NF}$  composite achieves a  $4555.0 \text{ F g}^{-1}$  specific capacitance at  $1 \text{ A g}^{-1}$  (Fig. 17 (e)) and a 78.7% capacitance retention undergoing 5000 cycles (Fig. 17 (f)).

Exploiting the synergistic effect of bilayer capacitance and pseudo capacitance and modifying nanostructures are also common strategies. Kuang et al.<sup>229</sup> designed and synthesized a core-shell heterostructure graphene nano scroll array composite, in which

petal-like NiCo-LDHs nanoflakes are vertically anchored to a 3D interconnected skeleton of GNSs, accomplished by a highly convenient microwave-assisted method (Fig. 17 (g)). This design combines several advantages, for example more active sites, promoting electron and ion collection/transport and buffering the volume variation in cycling process. Owing to its superior nanostructure (Fig. 17 (h, i)), the prepared NiCo-LDH@GNSs electrode has a  $1470 \text{ F g}^{-1}$  specific capacitance of  $1470 \text{ F g}^{-1}$  at  $1 \text{ A g}^{-1}$  and a 81.6% retention rate after 1000 cycles. Multilayer multi-walled carbon nanotube and graphene nanoribbon/CoNi-LDHs (MWGR/CoNi-LDHs) composite was prepared by Ma et al.<sup>230</sup> using a rapid microwave method. The synergistic effect between the MWCNTs-GONRs with high electrical conductivity, structural stability and electrochemical properties and the LDHs with a p-n junction structure facilitates the redox reaction. As a result, the MWGR/CoNi-LDHs has a unique heterogeneous structure and excellent electrochemical properties ( $1 \text{ A g}^{-1}$ , specific capacitance of  $1030.2 \text{ C g}^{-1}$ ) (Fig. 17 (b, c)). The prepared MWGR/Co-Ni LDH//AC devices have an energy density of  $47.2 \text{ Wh kg}^{-1}$  at  $0.85 \text{ kW kg}^{-1}$  and a 88.8% retention rate undergoing 10000 cycles at  $10 \text{ A g}^{-1}$ .

An intriguing heterostructure electrode material of NiFe-LDHs was fabricated through Zhang et al.<sup>231</sup> using a high-voltage electrochemical cycle activation (ECA) technique (Fig. 17 (j)). During the high-voltage ECA process, the surface of NiFe-LDHs is reconstituted in situ into a low-crystalline NiOOH phase, which eventually evolves into a unique NiFe-LDHs/NiOOH heterostructure. This surface reconstruction process can

generate abundant non-homogeneous interfaces, increase the active sites for reversible cation adsorption and intercalation, and significantly improve the electrochemical performances in neutral electrolytes. In a neutral electrolyte (2 M LiNO<sub>3</sub> solution), the ECA (1.2 V-50) electrode presented a 107 mAh g<sup>-1</sup> specific capacitance at 1 A g<sup>-1</sup> (Fig. 17 (k)), which was 50 times higher than that of the initial NiFe-LDHs (2.1 mAh g<sup>-1</sup> 1 A g<sup>-1</sup>). By coupling with MoS<sub>2</sub>/rGO electrodes, the assembled ECA (1.2 V-50)//MoS<sub>2</sub>/rGO hybrid supercapacitor device has an energy density of 48.1 Wh kg<sup>-1</sup> at 432.9 W kg<sup>-1</sup>.



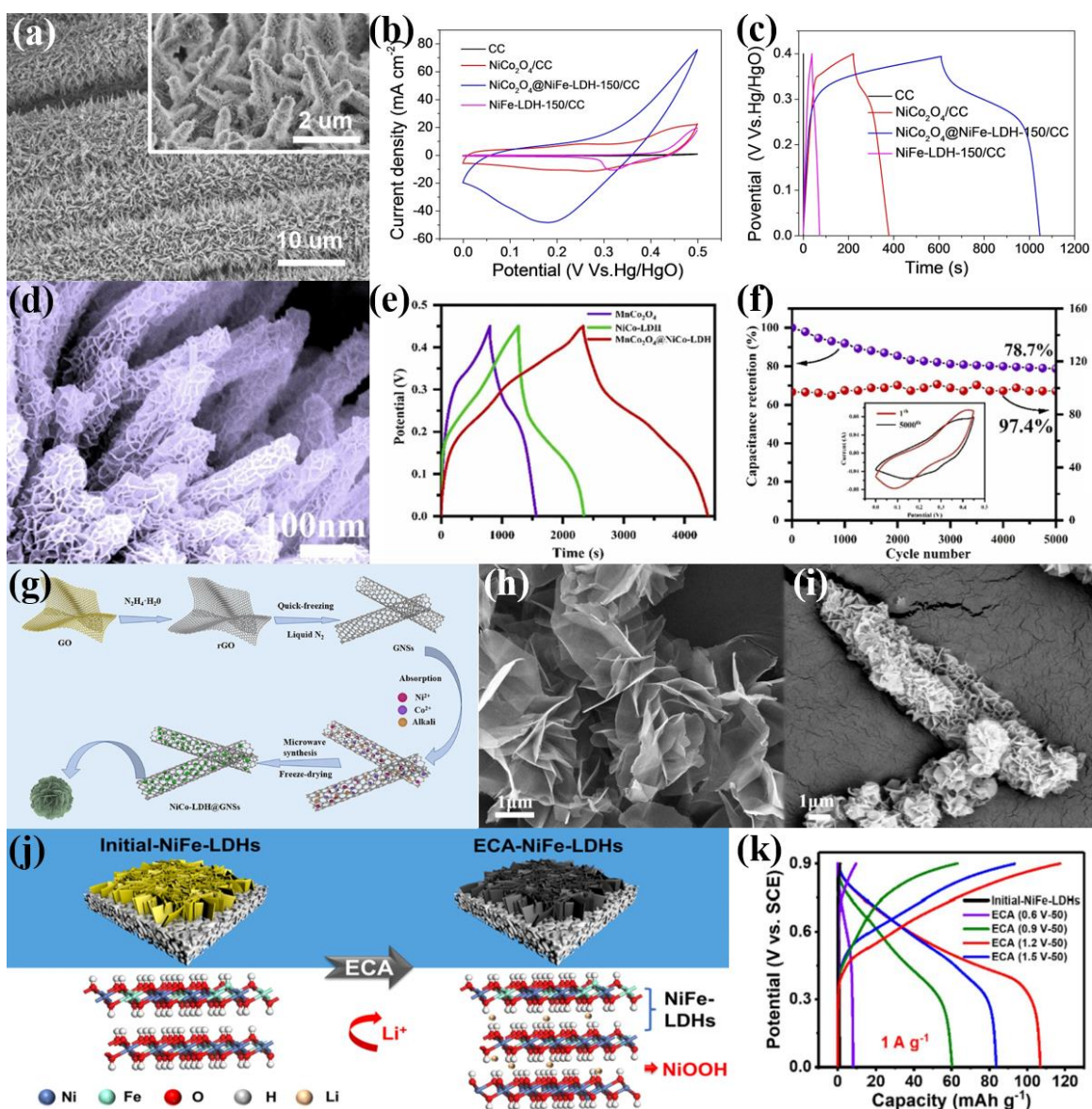


Fig. 17 (a) SEM image of  $\text{NiCo}_2\text{O}_4@\text{NiFe-LDHs-150/CC}$ , (b) CV curves of the CC,  $\text{NiCo}_2\text{O}_4/\text{CC}$ ,  $\text{NiCo}_2\text{O}_4@\text{NiFe-LDHs-150/CC}$  and  $\text{NiFe-LDHs-150/CC}$  at  $100 \text{ mV s}^{-1}$ , (c) GCD curves of the CC,  $\text{NiCo}_2\text{O}_4/\text{CC}$ ,  $\text{NiCo}_2\text{O}_4@\text{NiFe-LDHs-150/CC}$  and  $\text{NiFe-LDHs-150/CC}$  at  $1 \text{ mA cm}^{-2}$ .<sup>228</sup> Copyright 2022, Wiley-VCH GmbH. (d) SEM image of  $\text{MnCo}_2\text{O}_4@\text{NiCo-LDHs/NF}$ , (e) GCD curves of  $\text{MnCo}_2\text{O}_4/\text{NF}$ ,  $\text{NiCo-LDHs/NF}$  and  $\text{MnCo}_2\text{O}_4@\text{NiCo-LDHs/NF}$  at  $1 \text{ A g}^{-1}$ , (f) the cycling performance at  $10 \text{ A g}^{-1}$  (the inset showing CV curves recorded at the 1 st and 5000th cycles

measured at  $10 \text{ mV s}^{-1}$ ).<sup>167</sup> Copyright 2022, Elsevier B.V. (g) Schematic illustration of the synthesis procedures of NiCo-LDHs@GNSs, SEM images of (h) pristine NiCo-LDHs and (i) NiCo-LDHs@GNSs.<sup>229</sup> Copyright 2022 Elsevier Ltd. (j) Schematic illustration of the fabrication processes of ECA (1.2 V-50), (K) GCD curves of ECA (1.2 V-50) at  $1 \text{ A g}^{-1}$ .<sup>231</sup> Copyright 2022, Elsevier B.V.

Zeolite imidazolium skeletons (ZIFs) are excellent templates for the synthesis of functional materials and have extensively applications.<sup>232</sup> However, the direct use of ZIFs as electrode materials has limited exposed electroactive sites, poor chemical stability, slow charging kinetics and unsatisfactory electrochemical performances.<sup>233</sup> How to combine their advantages and give full play to their performance becomes a key issue. Liao et al.<sup>234</sup> demonstrated the in situ transformation of ZnCo-ZIFs modified on ZnCo nanorod arrays (ZnCo-NA) into 3D spatially distributed ZnCo-LDHs/ZnCo-NA heterostructures (Fig. 18 (a)). This structure has a huge specific surface area, and its SEM image is shown in Fig. 18 (b). The electrochemical performances was improved due to its abundant electroactive sites and ion migration paths in all directions, reaching a  $1576 \text{ F g}^{-1}$  specific capacitance at  $2 \text{ A g}^{-1}$ . In Fig. 18 (c), the ZnCo-LDHs/ZnCo-NA electrode has the longest discharge time of GCD curve, proving the best energy storage capacity among the three samples. A coin cell asymmetric supercapacitor (aSC) was assembled exhibiting a 88.1% capacitance retention after 5000 cycles. More importantly, this simple in situ mimetic transformation of the ZIFs template into an intriguing LDHs demonstrates the application of a new generation of



bimetallic heterostructures in energy-related fields.

Wan et al.<sup>168</sup> have in situ modified arrays of highly porous FeCoSe<sub>2</sub>@NiCo-LDHs core-shell nanosheets on the surface of CC by electrodeposition method and salinization treatment. The hierarchical heterogeneous structure consisting of two vertically aligned interconnected 2D nanosheets provided high surface area and an effective diffusion pathway for rapid electron/ion transport and generated a heterogeneous interface rich in electron structure alteration. The results show that the well-designed FeCoSe<sub>2</sub>@NiCo-LDHs electrode has a much higher specific capacitance of 220.9 mA h g<sup>-1</sup> at 1 A g<sup>-1</sup> and a capacity retention of 83.5% at 20 A g<sup>-1</sup>, with a cycling stability better than that of the one-component electrode. In addition, the asymmetric supercapacitor assembled from FeCoSe<sub>2</sub>@NiCo-LDHs electrodes and layered porous carbon electrodes exhibits an energy density of 65.9 Wh kg<sup>-1</sup> at 1.248 kW kg<sup>-1</sup> and a capacity retention of 87.6% after more than 10000 cycles. These excellent performances indicate that the integrated electrodes have good prospects, and the idea of synthesizing heterostructures on the substrate surface for improving the resulting performances has good operability.

The MXene/graphene oxide/NiMn-LDHs (MGL) material prepared by Chen et al.<sup>235</sup> also makes reasonable use of the advantages of the heterostructure (Fig. 18 (d)). By utilizing the heterostructure, the MXene stacking problem can be effectively prevented. SEM image of MGL show that nano-LDHs aggregates on the surface of MXene flakes, forming blocky porous arrays (Fig. 18 (e)). The structural stability of the matrix is ensured,

which can inhibit LDHs morphological collapse and thus significantly increase the specific capacitance of LDHs. The presentation of graphene oxide accelerates charge transfer and increasing the electron density. The existence of the various components in this heterogeneous structure largely enhances the active sites and electrochemical capability. As an anode material, MGL achieves a  $241.9 \text{ mAh g}^{-1}$  specific capacitance of and a 90.9% cycling stability at  $1 \text{ A g}^{-1}$  in the presence of multivalent (Mn, Ni) hydroxides and stabilized carbon materials. The combination of the conductivity of the surface graphene oxide and the substrate MXene increases the available electrons on the hydroxide root. The assembled asymmetric device can achieve a  $2.0 \text{ V}$  voltage window (Fig. 18 (f)). This once again demonstrates the importance of constructing heterogeneous structures for enhancing the electrochemical properties and proves that the synergy between these three materials has a wide range of applications. Besides, Zhu et al.<sup>236</sup> prepared  $\text{Co}_2\text{Mn}$  bimetallic hydroxide nanofins directly on NF by hydrothermal method, and then prepared  $\text{Co}_2\text{Al}$ -LDHs nanosheets on  $\text{Co}_2\text{Mn}$  nanofins by hydrothermal method to obtain heterostructure nanocomposites ( $\text{Co}_2\text{Al}/\text{Co}_2\text{Mn}/\text{NF}$ ) (Fig. 18(g)). Fig. 18 (h) shows the structure of  $\text{Co}_2\text{Al}/\text{Co}_2\text{Mn}/\text{NF}$  surface nanosheets. The specific capacitance can reach  $2502.0 \text{ F g}^{-1}$  at  $1 \text{ A g}^{-1}$ . Undergoing 7000 cycles, the specific capacitance is maintained at 92.21%. The energy density at  $412.73 \text{ W kg}^{-1}$  is  $64.58 \text{ Wh kg}^{-1}$ .

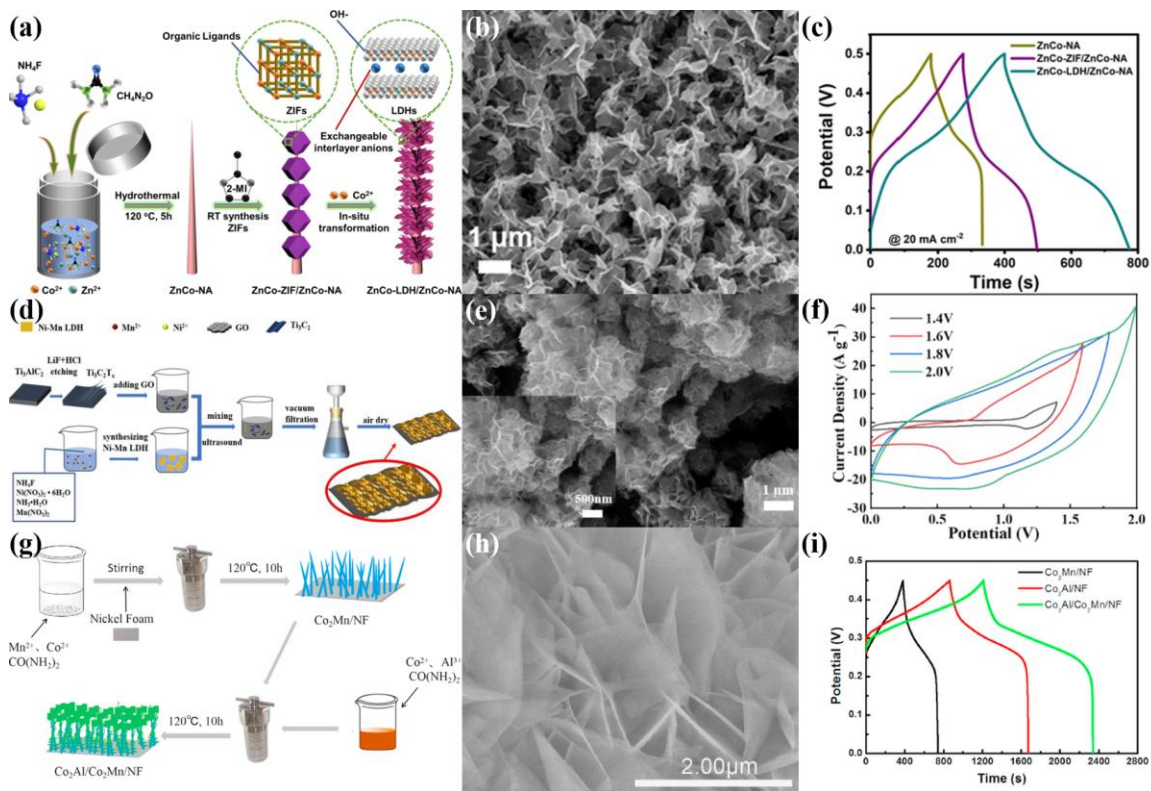


**Fig. 18** (a) Schematic illustration for the synthesis processes of ZnCo-LDHs/ZnCo-NA hybrid, (b) SEM image of ZnCo-LDHs/ZnCo-NA, (c) GCD curves of the ZnCo-NA, ZnCo-ZIF/ZnCo-NA and ZnCo-LDHs/ZnCo-NA electrodes.<sup>234</sup> Copyright 2022, Elsevier Inc. (d) Schematic illustration on the fabrication of MGL composite, (e) SEM image of MGL composite, (f) CV curves of MGL//AC in different scan potential windows at scan rate of  $100\ \text{mV s}^{-1}$ .<sup>235</sup> Copyright 2021, Elsevier Ltd. (g) Schematic diagram of the synthesis of  $\text{Co}_2\text{Al}/\text{Co}_2\text{Mn}/\text{NF}$ , (h) SEM image of  $\text{Co}_2\text{Al}/\text{Co}_2\text{Mn}/\text{NF}$ , (i) GCD curves of the  $\text{Co}_2\text{Mn}/\text{NF}$ ,  $\text{Co}_2\text{Al}/\text{NF}$  and  $\text{Co}_2\text{Al}/\text{Co}_2\text{Mn}/\text{NF}$  at current density of  $1\ \text{A g}^{-1}$ .<sup>236</sup> Copyright 2020, Elsevier B.V.

Stable  $\text{MnO}_2$  nanowires@NiCo-LDHs heterostructures were fabricated via a liquid-phase way by Ma et al.<sup>237</sup> The NiCo-LDHs nanosheets were grown uniformly in stable

channels on the surface of the ultra-long MnO<sub>2</sub> nanowires, and the synthesis schematic is shown in Fig. 19 (a). SEM images of MnO<sub>2</sub>@LDHs-2 sample in Fig. 19 (b) is made up of NiCo-LDHs nanosheets evenly grown on the MnO<sub>2</sub> periphery, which favors electron transfer and ion diffusion during the electrochemical reaction. Electrochemical testing revealed that the core-shell heterostructure separately displayed 708 C g<sup>-1</sup> and 630 C g<sup>-1</sup> specific capacitance at 1 A g<sup>-1</sup> and 10 A g<sup>-1</sup>, and a 82.3% capacitance retention rate after 2000 cycles. Characterization by Raman spectroscopy revealed that the prepared electrode has a transition from  $\alpha$  phase to  $\beta$  phase during cycling in comparison with NiCo-LDHs, due to the heterogeneous structure buffering the collapse. Furthermore, the asymmetric supercapacitor assembled with this electrode exhibits a 72.4% capacitance retention rate experiencing 10000 cycles. Chen et al.<sup>238</sup> constructed a bilayer LDHs nanosheet array through hydrothermal method (Fig. 19 (c)). The prepared bilayer electrode material with Ni, Co and Mn elements has a high surface area. As a result, this structure increases the contact between the electrolyte and the prepared material. The bilayer electrode showed excellent capacitive performance (2950 F g<sup>-1</sup> at 1 A g<sup>-1</sup>) (Fig. 19 (d)) and good stability (79% retention after 10000 cycles at 10 A g<sup>-1</sup>). Besides, the asymmetric NiCo/NiMn-LDHs//AC devices were prepared, which had good capacity and 82.2% cycling stability after 10000 cycles. The preparation of this double-LDHs array provides a new idea for increasing the active sites of electrode materials.

Two nanostructures of ZnO nanorods (NR) and nanosheets (NF) were prepared by

hydrothermal method on conductive flexible CC by Xiong et al.<sup>239</sup> Then NiCo-LDHs nanosheets were formed on these nanostructures for preparing NiCo-LDHs/ZnO NR/CC and NiCo-LDHs/ZnO NF/CC heterostructures (Fig. 19 (e)). The influences of ZnO morphology on electrochemical properties were studied in detail. The results show that the latter heterostructure is denser and more homogeneous than the former. The corresponding SEM image is shown in Fig. 19 (f). The latter heterostructure has more excellent electrochemical properties than the former heterostructure (Fig. 19 (g)), with a 2.6-fold specific capacitance ( $1577.6 \text{ F g}^{-1}$  at  $1 \text{ A g}^{-1}$ ), a 2.2-fold higher multiplicative capacity and a 1.5-fold higher cycling stability. Moreover, the NiCo-LDHs/ZnO NFs//AC asymmetric solid-state flexible device has a maximum energy density of  $51.39 \text{ Wh kg}^{-1}$  at  $800 \text{ W kg}^{-1}$  with 87.3% capacitance retention experiencing 1000 cycles. Finally, the two packaged devices were successfully lit in series with a red 2.2V LED, demonstrating the potential for practical applications. Zhou et al.<sup>240</sup> prepared porous heterostructure  $\text{NiCo}_2\text{S}_4/\text{NiCo-LDHs}$  on carbon fiber paper using a simple solvothermal method. The active material was deposited vertically on the carbon fiber paper and its SEM image is shown in Fig. 19 (i). This composite was assembled from nanoflakes into an intertwined 3D structure with abundant microporous dimensions and excellent electrochemical properties. Its unique structure facilitates the acceleration of electron transfer and electrolyte transport during electrochemical processes. The specific capacitance was  $1403 \text{ F g}^{-1}$  at  $10 \text{ mA cm}^{-2}$ . At  $30 \text{ mA cm}^{-2}$ , the capacitance retention undergoing 5000 cycles reached 111.1%, showing

excellent cycling stability. Symmetric supercapacitors assembled from this material correspond to a  $0.19 \text{ F cm}^{-2}$  area capacitance at  $3 \text{ mA cm}^{-2}$  (Fig. 19 (h)).

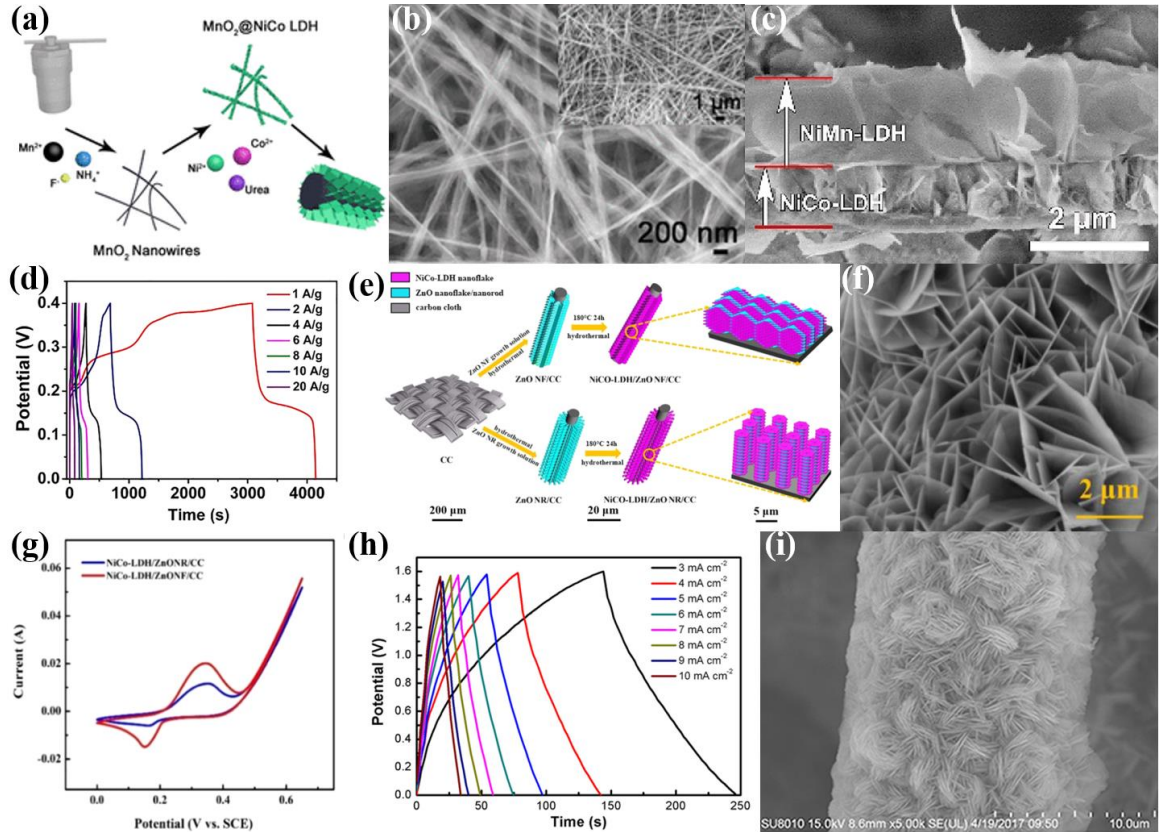


Fig. 19 (a) Schematic illustration of the formation processes for the stable MnO<sub>2</sub> nanowires@NiCo-LDHs nanosheet core-shell heterostructure, (b) SEM image of MnO<sub>2</sub>@LDHs-2 samples.<sup>237</sup> Copyright 2021, American Chemical Society. (c) Cross-sectional diagram of NiCo-LDHs and NiCo/NiMn-LDHs, (d) GCD curves of NiCo/NiMn-LDHs electrode at various current densities, respectively.<sup>238</sup> Copyright 2021, Elsevier Ltd. (e) The synthesis procedures of NiCo-LDHs NF on ZnO NF/CC and ZnO NR/CC substrates, (f) SEM image of NiCo-LDHs/ZnO NF/CC, (g) CV profiles of NiCo-LDHs/ZnO NR/CC and NiCo-LDHs/ZnO NF/CC electrodes at the scanning speed of  $5 \text{ mV s}^{-1}$ .<sup>239</sup> Copyright 2020, Elsevier B.V. (h) Galvanostatic current charge-

discharge curves at different current densities, (i) SEM image of  $\text{NiCo}_2\text{S}_4/\text{NiCo-LDHs}$  sample.<sup>240</sup>

Copyright 2021, Springer.

### 3.4 Preparation of binder-free materials

Growing metal precursors directly onto the surface of the **current collector**, such as NF, copper foam, stainless steel mesh and carbon-based materials, offers significant advantages.<sup>241-243</sup> **This modification strategy reduces the mass of inactive materials such as conductive polymer binders, increasing the total energy density and allowing for lighter weight devices to be assembled.**<sup>244</sup> In the process, charge transfer and internal resistance are reduced. Besides, the elimination of the polymer binder allows more electroactive sites to be exposed, which increases the electrical conductivity and speeds up the rate of electron transfer. Importantly, this strategy allows for the combination of different types of active material, which provides the opportunity for multi-component synergistic effects that improve electrochemical performance.<sup>35</sup> **But a suitable base material needs to be selected. The pretreatment for base material is beneficial to the growth of active material.**

Li et al.<sup>245</sup> synthesized nickel iron sulfide nanosheets ( $\text{NiFeSx}$ ) and carbon nanotubes (CNTs) on diatomite by chemical vapor deposition and two-step hydrothermal method to overcome transition metal LDHs in the field of supercapacitors application challenges such as easy aggregation and low conductivity. The synthesis of this composite successfully exploited the cooperative effect of multicomponent materials for enhancing the electrochemical properties (Fig. 20 (a)). SEM image of  $\text{NiFeSx@CNTs@MnS}$  is shown in



Fig. 20 (b). After the simultaneous sulfidation process, NiFeSx also has ortho-hexagonal nanosheet morphology and shows the presence of CNTs on its surface. The diatomite as the matrix can provide a good environment for the uniform dispersion of nanomaterials on its surface, expands the active sites in contact with the electrolyte, and significantly improves the electrochemical performance. Combining high conductivity and simultaneous sulfurization effect, NiFeSx@CNTs@MnS@diatomite structure displays a 552 F g<sup>-1</sup> specific capacitance at 1 A g<sup>-1</sup> (Fig. 20 (c)) and a retention rate of 68.4% at 10 A g<sup>-1</sup>, maintaining a 89.8% cycling stability after 5000 cycles at 5 A g<sup>-1</sup>. Furthermore, the asymmetric supercapacitor assembled by this composite and graphene achieves an energy density of 28.9 Wh kg<sup>-1</sup> at 9375 W kg<sup>-1</sup>. Rajapriya et al.<sup>246</sup> synthesized laminated NiS nanoflowers on flexible CC substrates by hydrothermal method, and then used electrodeposition to vertically immobilize Sr-Fe LDHs nanosheets on highly conductive and flexible NiS/CC electrodes without destroying the original structure. This abundant 3D hybridized NiS@Sr-Fe OH/CC nanostructure provides a large number of nucleation active sites. The excellent structural (Fig. 20 (d)) and morphological advantages of the reticular flakes accelerate the activity of NiS/CC, Sr-Fe OH/CC and NiS@Sr-Fe OH/CC flexible electrodes having specific capacitances of 556, 1151 and 1553 F g<sup>-1</sup> (Fig. 20 (e, f)) at 1 A g<sup>-1</sup>, respectively. The NiS@Sr-Fe OH/CC//AC/CC device has an energy density of 53.07 Wh kg<sup>-1</sup> at 4.4 kW kg<sup>-1</sup>.

Lohani et al.<sup>247</sup> designed an assembly of thin-LDHs nanosheets arranged in the lumen

and luminal portions of a polypyrrole tunnel as electrode material. SEM images show NiCo-LDHs@H-PPy@CC electrode are constructed by combining NiCo-LDHs nanosheets inside and outside the lumen on long polypyrrole tunnels on CC (Fig. 20 (g)). The capacitance of the sample at  $1.0 \text{ mA cm}^{-2}$  was  $149.16 \text{ mAh g}^{-1}$  (Fig. 20 (h, i)). Besides, the device consisting of NiCo-LDHs@H-PPy@CC and vanadium phosphate carbon nanofibers (VPO@CNFs900) has a specific energy density of  $32.42 \text{ Wh kg}^{-1}$  at  $3 \text{ mA cm}^{-2}$ . Using the facile and feasible in-situ oxidation combined with potentiation electrodeposition method, Wang et al.<sup>248</sup> constructed densely distributed, core-shell structured  $\text{Cu(OH)}_2$ @NiFe-LDHs nanoarrays (COH@NF-LDHs/CF) on copper foam. This unique core-shell structure and the synergy between  $\text{Cu(OH)}_2$  and NiFe-LDHs provide great advantages such as sufficient chemically active sites, electron and ion transfer pathways to enhance the electrochemical performances. Especially at  $5 \text{ mA cm}^{-2}$ , the capacitance of the synthesized COH@NF-LDHs/CF can reach  $4.139 \text{ F cm}^{-2}$ , which is significantly better than those of single bare  $\text{Cu(OH)}_2$  ( $198 \text{ mF cm}^{-2}$  at the same current density) and NiFe-LDHs/CF ( $71 \text{ mF cm}^{-2}$ ). Furthermore, COH@NF-LDHs/CF exhibits remarkable stability (86.47% for 5000 cycles). The asymmetric supercapacitor possesses a high energy density of  $65.56 \text{ Wh kg}^{-1}$  at  $750 \text{ W kg}^{-1}$ .

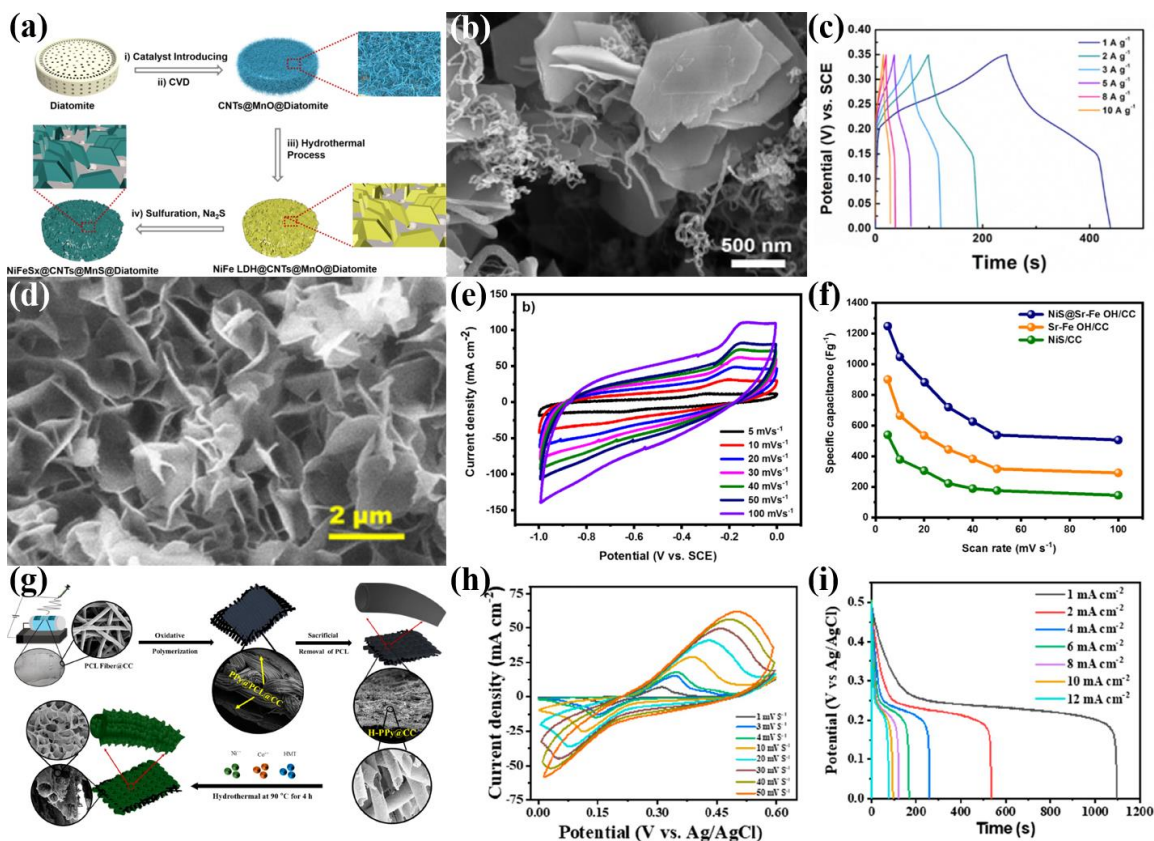


Fig. 20 (a) The schematic illustration for the preparation processes of NiFeSx@CNTs@MnS@Diatomite, (b) SEM image of NiFeSx@CNTs@MnS@Diatomite, (c) GCD curves with different current densities.<sup>245</sup> Copyright 2021, Elsevier Inc. (d) SEM images of NiS@Sr-Fe OH/CC nanostructure. (e) CV curves at different scan rates, (f) the calculated specific capacitance of Sr-Fe OH/CC, NiS/CC and NiS@Sr-Fe OH/CC at 5-100 mV s<sup>-1</sup>.<sup>246</sup> Copyright 2022, Elsevier Ltd. (g) Schematic representation of the step-by-step synthesis of NiCo-LDH@H-PPy@CC, (h) CV curves at different scan rates, (i) GCD profile for the NiCo-LDHs@H-PPy@CC electrode at different current densities.<sup>247</sup> Copyright 2022, American Chemical Society.

NF is also commonly used as a substrate material in supercapacitors, mainly because of porous structure, low density and excellent conductivity. The growth of LDHs on its

surface as supercapacitor electrode materials has several advantages: The 3D mesh structure of NF substrate enables the effective deposition of active materials and promotes the transfer of charges. Direct deposition of LDHs material on NF eliminates the need for pressing during electrochemical performance testing and eliminates the need for adhesive, making the test results more representative. Cao et al.<sup>249</sup> chemically etched NF with transition metal (NiCo-based) nitric acid solutions of different Ni and Co ratios. And after rinsing and drying, the etched NF was used as the anode and the platinum mesh as the cathode in an alkaline solution. By constant voltage action, NiCo-LDHs will self-grow on the NF (Fig. 21 (a)). The  $\text{Ni}_1\text{Co}_2/\text{NF}$  monolithic electrode exhibited the best electrochemical performanceS with a specific capacitance of  $3.01 \text{ C cm}^{-2}$  at  $1 \text{ mA cm}^{-2}$  (Fig. 21 (b)). A hybrid device showed the energy density of  $97.4 \text{ pWh cm}^{-2}$  at  $800.5 \text{ } \mu\text{W cm}^{-2}$ , and an initial capacity of 85.0% after 5000 cycles (Fig. 21 (c)).

The CoMn-LDHs nanostructured high-performance self-contained supercapacitor electrode was prepared on NF surface by Emin et al.<sup>250</sup> by employing electrochemical deposition, as shown in Fig. 21 (e). The electrode has an open interconnected thin layered structure (Fig. 21 (d)) with a high capacitance of  $2673.6 \text{ F g}^{-1}$  at  $1 \text{ A g}^{-1}$  (Fig. 21 (f)) and good cycling stability (86.7% for 5000 cycles at  $12 \text{ A g}^{-1}$ ). The asymmetric device has an energy density of  $97.5 \text{ Wh kg}^{-1}$  at  $800.0 \text{ W kg}^{-1}$ , a capacitance retention of 89.2% for 5000 cycles at  $5 \text{ A g}^{-1}$ , and a coulombic efficiency of about 100% (Fig. 21 (g)). Lu et al.<sup>251</sup> constructed a binder-free NiCo-LDHs high-performance energy storage device on NF by

in situ electrochemically triggered MOF hydrolysis, which has remarkable energy storage capacity under solar irradiation (Fig. 21 (h)). Through electrochemically controlled hydrolysis, the ligands in the MOFs are replaced by  $\text{OH}^-$  and the resulting NiCo-LDHs retain the original layered porous structure of the MOFs. The NiCo-LDHs electrode has ample oxygen vacancies and a large surface area (Fig. 21 (i)), reaching a capacity of  $5.4 \text{ C cm}^{-2}$  at  $1.25 \text{ mA cm}^{-2}$ , 64.3 times than that of the MOF template. Importantly, the electrode material also has excellent photothermal conversion capabilities ( $52.9^\circ\text{C}$  temperature rise in only 30 s). Furthermore, the energy density of the asymmetric supercapacitor prepared using NiCo-LDH increased by 329.2% after 15 min of sunlight irradiation at low temperatures ( $-4^\circ\text{C}$ ).

Stainless steel mesh (SS) is also a suitable substrate material for the growth of LDHs. Wang et al.<sup>252</sup> prepared uniformly distributed 3D NiFe Prussian blue analogues (NiFe PBAs) nanocubes on SS and transformed them into 3D oxide arrays (SS@NiFe NSs@NiFe NCs) by penetrating 2D NiFe-LDHs and thermally annealing them in air (Fig. 21 (j)). This 3D array shows a nanocubic structure (Fig. 21 (k)) with high specific surface area and good electrochemical properties. In addition, hybrid supercapacitor (HSC) SS@NiFe NSs@NiFe NCs//SS@Fe<sub>2</sub>O<sub>3</sub> devices were assembled and showed impressive electrochemical performance. In order to show the performances in this chapter, Table 3 display the properties of device based on LDHs and its composite electrodes.

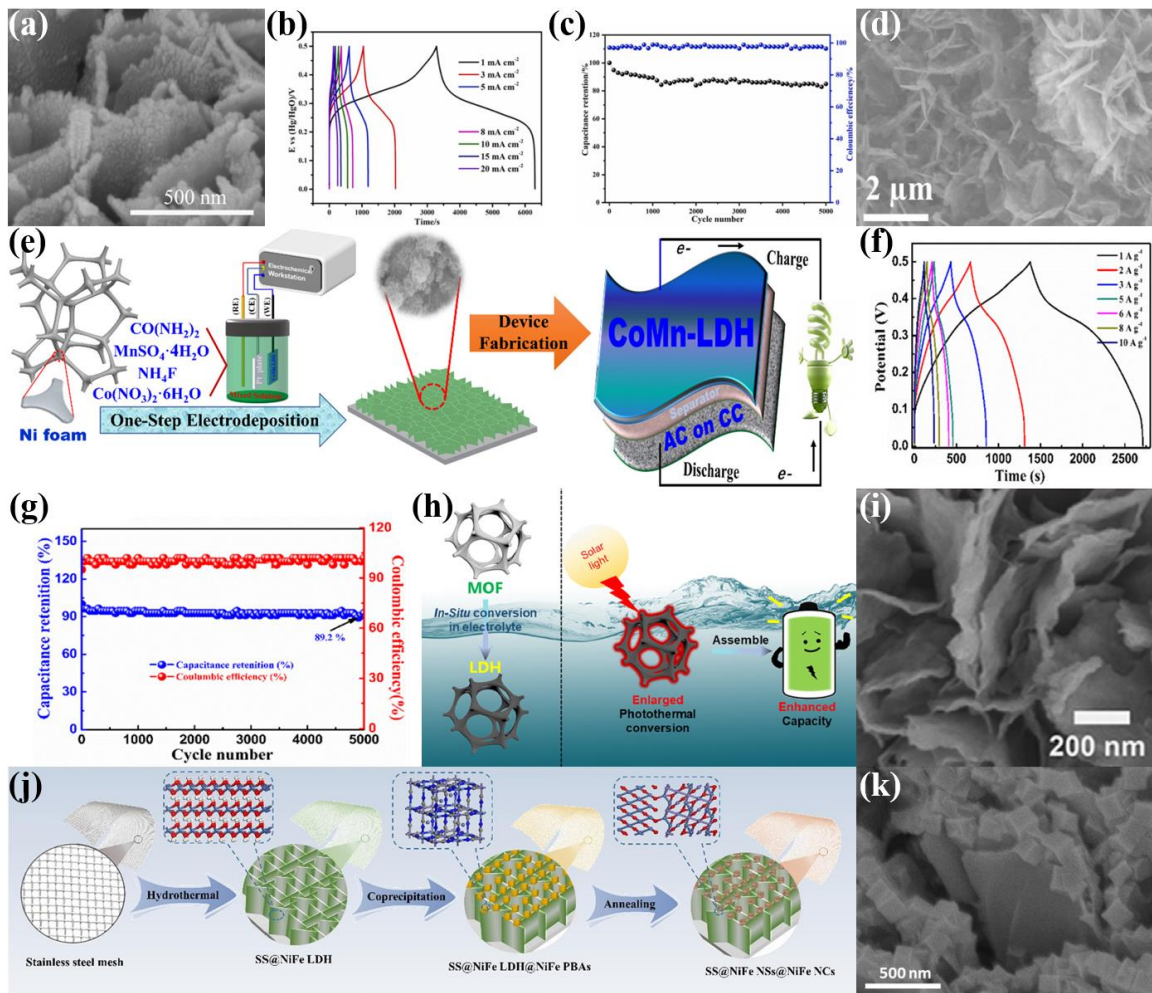


Fig. 21 (a) SEM image of NiCo-LDHs hierarchical nanosheets on NF, (b) GCD curves of  $\text{Ni}_1\text{Co}_2/\text{NF}$  electrode with current densities from 1 to 20  $\text{mA cm}^{-2}$ , (c) cycling performance of the HSC device.<sup>249</sup> Copyright 2022, Elsevier B.V. (d) SEM image of CoMn-LDHs, (e) main fabrication procedures of the CoMn-LDHs cathodes and AASCs, (f) GCD curves at various current densities of 1-10  $\text{A g}^{-1}$ , (g) cycling performance and coulombic efficiency during 5000 cycles at 5  $\text{A g}^{-1}$ .<sup>250</sup> Copyright 2022, Elsevier Ltd. (h) Synthesis and working process diagram, (i) SEM image of NC37.<sup>251</sup> Copyright 2022, Elsevier B.V. (j) Schematic illustration of the formation of SS@NiFe-LDHs@NiFe NCs, (k) SEM image of SS@NiFe NSs@NiFe NCs.<sup>252</sup> Copyright 2021, Elsevier B.V.



### 3.5 Application of LDHs-based supercapacitors

LDHs-based supercapacitors are widely used in flexible wearability or integration with other intelligent devices. Li et al.<sup>253</sup> prepared NiCo-LDH on flexible CC and  $\text{Ti}_3\text{C}_2\text{T}_x$  functional CC by high magnetic field electrodeposition (Fig. 22 (a)). The flexible hybrid supercapacitor has excellent energy density and cyclic stability. The device exhibits slight polarization during bending and the total capacitance remains almost constant, further confirming the great flexibility (Fig. 22 (b), (c)). Three devices connected in series lighting up the red and yellow LED lights connected in parallel proves the potential application (Fig. 22 (d)). Nagaraju et al.<sup>254</sup> used a hot-air oven-based method to grow aligned NC LDH NFAs on Ni fabric and a simple electrochemical deposition method to further decorate fluffy NC LDH NS branches on NC LDH NFAs (Fig. 22 (e)). The shape of the CV curves measured under various bending conditions at  $50 \text{ mV s}^{-1}$  is almost similar to normal without any distortion (Fig. 22 (f), (g)), which shows that the device has good capacitance and flexibility. Fig. 22 (h) demonstrates its potential suitability for wearable electronic applications. By adjusting the ratio of Ni and Co, Liu et al.<sup>255</sup> obtained the optimized porous nanoflower-like NiCo LDH (Fig. 22 (i)). A flexible  $\text{Ni}_3\text{Co}_1 \text{ LDH@graphene//AC}$  asymmetric supercapacitor is prepared by using screen printing, and the device exhibits excellent flexibility with maintaining 95.8% capacitance after bending at different angles and 400 bends (Fig. 22 (j)). When the two devices are connected in series, they can power



the watch for more than 60 minutes after only 50 seconds of charging, and can power the watch normally even when it is worn on the hand and fully submerged in water (Fig. 22 (k), (l)).

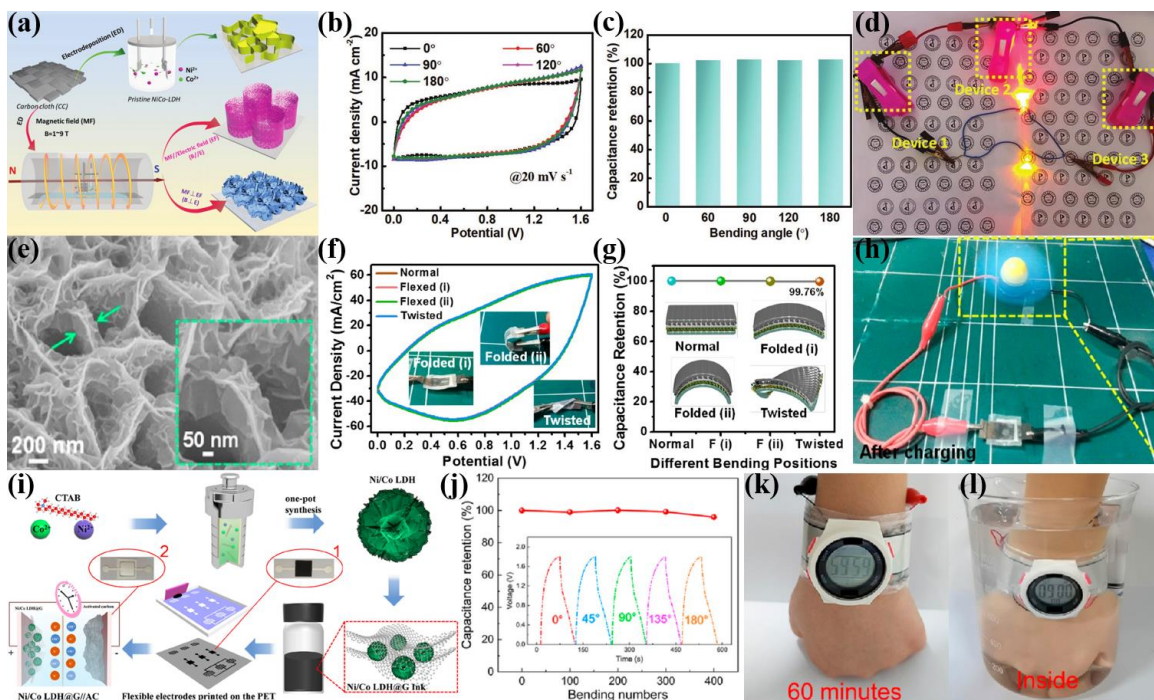


**Fig. 22** (a) Schematic illustration of the preparation of NiCo-LDH on CC, (b) CV curves and (c)

capacitance retention of the device with bending at different angles, (d) digital picture of three

devices connected in series lighting up the red and yellow LED lights connected in parallel.<sup>253</sup>

Copyright 2022 Wiley-VCH GmbH. (e) Core-shell-like NC-LDH NFAs@NSs/Ni fabric, (f) CV

curves and (g) capacitance retention of the flexible hybrid SC under various flexed conditions, the

corresponding insets showing the photographic and schematic diagrams of the device under flexed

states, (h) the potential suitability of the device for wearable electronic applications.<sup>254</sup> Copyright

2017 American Chemical Society. (i) Schematic diagram of the preparation of screen-printed

flexible NiCo LDH-based electrodes, (j) capacitance retention of the flexible Ni<sub>3</sub>Co<sub>1</sub> LDH@G//AC

ASC under different bending cycles, inset of GCD curves tested under different bending angles,

(k) two devices connected in series to power the electronic watch, (l) two devices connected in

series in water to power the electronic watch.<sup>255</sup> Copyright 2022 American Chemical Society.

**Table. 3 Properties of devices consisting of LDHs and its composites mentioned in this chapter.**

Devices	Electrolyte	Capacitance	Energy density at power density	Cycles	Ref.
3%-Ni-C/NiAl-LDHs//AC	6 M KOH	210.8 C g <sup>-1</sup> , 1 A g <sup>-1</sup>	74.9 Wh kg <sup>-1</sup> at 800 W kg <sup>-1</sup>	10000, 91.4%	<sup>205</sup>
NiCo-LDHs-S/PNT//GF-LDHs@NF	3 M KOH	98 F g <sup>-1</sup> , 1 A g <sup>-1</sup>	16.28 Wh kg <sup>-1</sup> at 650 W kg <sup>-1</sup>	8000, 74%	<sup>87</sup>
CoFe-LDHs/P2//AC	6 M KOH	1686 F g <sup>-1</sup> , 1 A g <sup>-1</sup>	75.9 Wh kg <sup>-1</sup> at 1124 W kg <sup>-1</sup>	10000, 97.5%	<sup>209</sup>
CoNiMg-LDHs//AC	—	333 C g <sup>-1</sup> , 1 A g <sup>-1</sup>	73.9 Wh kg <sup>-1</sup> at 0.8 kW kg <sup>-1</sup>	5000, 87%	<sup>212</sup>
NCW-2//rGO	PVA-KOH	98 F g <sup>-1</sup> , 2 A g <sup>-1</sup>	34 Wh kg <sup>-1</sup> at 1.32 kW kg <sup>-1</sup>	10000, 86%	<sup>182</sup>
Ni-Co(OH)(BA)//AC	—	118 F g <sup>-1</sup> , 1 A g <sup>-1</sup>	47.5 Wh kg <sup>-1</sup> at 850 W kg <sup>-1</sup>	8000, 91%	<sup>207</sup>
ECA(1.2 V-50)//MoS <sub>2</sub> /rGO	—	134 F g <sup>-1</sup> , 0.5 A g <sup>-1</sup>	48.1 Wh kg <sup>-1</sup> at 432.9 W kg <sup>-1</sup>	—	<sup>231</sup>
NiAl-Cl LDHs//AC	6 M KOH	81.82 F g <sup>-1</sup> , 1 A g <sup>-1</sup>	53.9 Wh kg <sup>-1</sup> at 1540 W kg <sup>-1</sup>	1000, 94.1%	<sup>206</sup>
NMHS-4//AC	1 M KOH	97.3 F g <sup>-1</sup> , 1 A g <sup>-1</sup>	34.61 Wh kg <sup>-1</sup> at 831 W kg <sup>-1</sup>	10000, 85%	<sup>213</sup>
ZnO@Ni/Co-LDHs//AC	PVA-KOH	24.6 mF cm <sup>-2</sup> , 0.5 mA cm <sup>-2</sup>	7.7 uW h cm <sup>-2</sup> at 375.0 pW cm <sup>-2</sup>	—	<sup>211</sup>
CuCoNi-OH//HPC	3 M KOH	180 C g <sup>-1</sup> , 0.5 A g <sup>-1</sup>	39.67 Wh kg <sup>-1</sup> at 400 W kg <sup>-1</sup>	—	<sup>210</sup>

NiFe-LDHs@SCN-32//AC	6 M KOH	386 F g <sup>-1</sup> , 1 A g <sup>-1</sup>	68.7 Wh kg <sup>-1</sup> at 827.5 W kg <sup>-1</sup>	8000, 83.3%	214
NTA18//AC	1 M KOH	126 F g <sup>-1</sup> , 1 A g <sup>-1</sup>	45.1 Wh kg <sup>-1</sup> at 16000 W kg <sup>-1</sup>	5000, 59%	183
CuCo-LDHs//AC	1 M KOH	76 F g <sup>-1</sup> , 1 A g <sup>-1</sup>	22 Wh kg <sup>-1</sup> at 23200 W kg <sup>-1</sup>	10000, 91.3%	185
D-NiCo-LDHs/NF//AC	3 M KOH	267 F g <sup>-1</sup> , 1 A g <sup>-1</sup>	53 Wh kg <sup>-1</sup> at 752 W kg <sup>-1</sup>	5000, 94.7%	216
3D-NiCo-SDBS-LDHs//AC	1 M KOH	205.7 F g <sup>-1</sup> , 1 A g <sup>-1</sup>	73.14 Wh kg <sup>-1</sup> at 800 W kg <sup>-1</sup>	10000, 95.5%	218
NiCo-LDHs-2//AC	6 M KOH	559 C g <sup>-1</sup> , 1 A g <sup>-1</sup>	101.1 Wh kg <sup>-1</sup> at 1500 W kg <sup>-1</sup>	5000, 87.8%	220
V <sub>Zn</sub> -defect sample//AC	1.2 M LiOH	528.5 mF cm <sup>-2</sup> , 2 mA cm <sup>-2</sup>	1.03 mW h cm <sup>-3</sup> at 9.35 mW cm <sup>-2</sup>	2000, 85.6%	215
Co <sub>0.50</sub> -Ga <sub>0.50</sub> -LDHs//AC	6 M KOH	187 mF cm <sup>-2</sup> , 3.15 mA cm <sup>-2</sup>	33.38 Wh kg <sup>-1</sup> at 920 W kg <sup>-1</sup>	10000, 95.8%	222
E-CoZnAl-LDHs-8 h//AC	1 M KOH	114 F g <sup>-1</sup> , 1 A g <sup>-1</sup>	36.75 Wh kg <sup>-1</sup> at 400 W kg <sup>-1</sup>	8000, 72.7%	217
NiCo-LDHs@MoO <sub>3</sub> /NF//AC	2 M KOH	952.2 C g <sup>-1</sup> , 1 A g <sup>-1</sup>	58.06 Wh kg <sup>-1</sup> at 800 W kg <sup>-1</sup>	10000, 86.42%	161
NiCo-LDHs@GNSs//AC	3 M KOH	102.6 F g <sup>-1</sup> , 1 A g <sup>-1</sup>	32.1 Wh kg <sup>-1</sup> at 750.4 W kg <sup>-1</sup>	—	229

MWGR/CoNi-LDHs//AC	6 M KOH	132.9 F g <sup>-1</sup> , 1 A g <sup>-1</sup>	47.2 Wh kg <sup>-1</sup> at 850 W kg <sup>-1</sup>	10000, 88.8%	230
MnCo <sub>2</sub> O <sub>4</sub> @NiCo-LDHs/NF//AC	6 M KOH	60 F g <sup>-1</sup> , 1 A g <sup>-1</sup>	21.3 Wh kg <sup>-1</sup> at 160 W kg <sup>-1</sup>	5000, 86.6%	167
ZnCo-LDHs/ZnCo-NA//AC	6 M KOH	68.4 F g <sup>-1</sup> , 0.2 A g <sup>-1</sup>	21.3 Wh kg <sup>-1</sup> at 900 W kg <sup>-1</sup>	5000, 88.1%	234
FeCoSe <sub>2</sub> @NiCo-LDHs//PPC-2	2 M KOH	95.2 mAh g <sup>-1</sup> , 1 A g <sup>-1</sup>	1.248 kW kg <sup>-1</sup> at 65.9 Wh kg <sup>-1</sup>	10000, 87.6%	168
MXene/GO/Ni-Mn LDHs//AC	PVA-KOH	69.1 mAh g <sup>-1</sup> , 1 A g <sup>-1</sup>	55.3 Wh kg <sup>-1</sup> at 800 W kg <sup>-1</sup>	4000, 94.7%	235
Co <sub>2</sub> Al/Co <sub>2</sub> Mn/NF//AC	6 M KOH	281.7 C g <sup>-1</sup> , 0.5 A g <sup>-1</sup>	64.58 Wh kg <sup>-1</sup> at 412.7 W kg <sup>-1</sup>	7000, 92.21%	236
MnO <sub>2</sub> @LDHs-2//AC	6 M KOH	95.5 F g <sup>-1</sup> , 0.5 A g <sup>-1</sup>	31.9 Wh kg <sup>-1</sup> at 502.7 W kg <sup>-1</sup>	10000, 72.4%	237
NiCo/NiMn-LDHs//AC	6 M KOH	185.1 F g <sup>-1</sup> , 1 A g <sup>-1</sup>	45.16 Wh kg <sup>-1</sup> at 1400 W kg <sup>-1</sup>	10000, 82.2%	238
NiCo-LDHs/ZnO NFs//AC	1 M KOH	144.5 F g <sup>-1</sup> , 1 A g <sup>-1</sup>	51.39 Wh kg <sup>-1</sup> at 800 W kg <sup>-1</sup>	1000, 87.3%	239
NiFeSx@CNTs@MnS@diatomite//graphene	6 M KOH	92.3 F g <sup>-1</sup> , 0.5 A g <sup>-1</sup>	28.9 Wh kg <sup>-1</sup> at 9375 W kg <sup>-1</sup>	5000, 80.8%	245
NiS@Sr-Fe OH/CC//AC	1 M KOH	146.21 F g <sup>-1</sup> , 1 A g <sup>-1</sup>	53.07 Wh kg <sup>-1</sup> at 4.4 kW kg <sup>-1</sup>	—	246
NiCo-LDHs@H-PPy@CC//VPO@CNFs900	2 M KOH	40.53 mAh g <sup>-1</sup> , 3 mA cm <sup>-2</sup>	32.42 Wh kg <sup>-1</sup> at 359.16 W kg <sup>-1</sup>	10000, 94.09%	247

COH@NF-LDHs/CF//AC	6 M KOH	195.7 F g <sup>-1</sup> , 1 A g <sup>-1</sup>	65.56 Wh kg <sup>-1</sup> at 750 W kg <sup>-1</sup>	5000, 88.93%	248
Ni <sub>1</sub> Co <sub>2</sub> /NF//AC	1 M KOH	273.8 mF cm <sup>-2</sup> , 1 mA cm <sup>-2</sup>	97.4 pWh cm <sup>-2</sup> at 800.5 μw cm <sup>-2</sup>	5000, 85%	249
CoMn-LDHs//AC	2 M KOH	274.26 F g <sup>-1</sup> , 1 A g <sup>-1</sup>	97.5 Wh kg <sup>-1</sup> at 800 W kg <sup>-1</sup>	5000, 89.2%	250
NiCo-LDHs//GO/AC	1 M KOH	1.4 C cm <sup>-2</sup> , 1.25 mA cm <sup>-2</sup>	1.06 mWh cm <sup>-2</sup> at 1.03 mW cm <sup>-2</sup>	—	251
NSs@NiFe NCs//SS@Fe <sub>2</sub> O <sub>3</sub>	1 M Na <sub>2</sub> SO <sub>4</sub>	102 F g <sup>-1</sup> , 1 A g <sup>-1</sup>	45.9 Wh kg <sup>-1</sup> at 902.7 W kg <sup>-1</sup>	2000, 89.7%	252
Ti <sub>3</sub> C <sub>2</sub> T <sub>x</sub> /NiCo-LDH-3 T (B//E)//AC	PVA-KOH	3.12 C cm <sup>-2</sup> , 1 mA cm <sup>-2</sup>	0.134 mWh cm <sup>-2</sup> at 1.61 mW cm <sup>-2</sup> 2	6000, 82.3%	253
NC LDH NFAs@NSs/Ni fabric//AC@CF	1 M KOH	1147.23 mF cm <sup>-2</sup> , 3 mA cm <sup>-2</sup> 2	46.15 Wh kg <sup>-2</sup> at 2604.42 W kg <sup>-1</sup>	2000, 86.49%	254
Ni <sub>3</sub> Co <sub>1</sub> LDH@G//AC	PVA-KOH	599 mF cm <sup>-2</sup> , 1 mA cm <sup>-2</sup>	0.27 mWh cm <sup>-2</sup> at 0.9 mW cm <sup>-2</sup>	10000, 123%	255

#### 4. Summary and outlook

Supercapacitors is one of the most promising energy storage devices, because of the advantages of fast charging and discharging speed, large temperature range and long cycle life. Large specific surface area by layered structure can substantially increase the double layer capacitance, and the redox reaction of transition metal elements can provide pseudocapacitance. The LDHs can be used for the energy storage of supercapacitors by both double layer capacitance and pseudocapacitance mechanisms. Meanwhile, the anions between the layers give rich options for modification and compounding of LDHs.

The advantages and disadvantages of each method can be considered after a broad understanding of the various synthesis methods. The appropriate method can be reasonably selected to prepare electrode materials with better performances. However, the prepared electrode materials in many cases still do not meet the actual requirements. Thus, the modification of the materials is particularly important. For instance, other components can be added during the preparation process or compounded with other materials for performance optimization. The defects can be constructed by etching and heat treatment for increasing the number of active sites. The heterogeneous structures can be generated on LDHs by electrochemical deposition to promote electron transfer. The electrode materials can be grown directly on the substrate to generate binder-free electrodes to reduce the internal resistance and mass, as well as enhance the ability of charge transfer.

This paper reviews the recent progress and results of preparation methods and



modification methods of hybrid LDHs, providing a cutting-edge reference for supercapacitor applications based on LDHs. A comprehensive understanding of the characteristics of various synthesis and modification methods can help to further synthesize materials with outstanding performances. There are both connections and distinctions between different synthesis and modification methods, and adequate mastery of these methods facilitates further research.

However, the LDHs still have poor electrical conductivity, which inevitably leads to blocked electron transfer in the redox process and further affects the capacitance performances. Specifically, the CV curve deviates from the rectangular shape and the current-voltage is correspondingly poor during constant GCD processes. Moreover, the existing methods for synthesis and modification of LDHs still have the disadvantages of complex reaction conditions and environmental pollution, which should be combined with the actual conditions in the subsequent research process to select the appropriate synthesis and modification methods.

It is a very meaningful work to further enhance the conductivity and the structure stability in order to expand the application fields while making full use of the structural advantages of the LDHs. As the research progresses, the preparation of LDHs evolves from simply using the synthesized LDHs directly as electrode materials to composite materials, and the continuous optimization of properties can enable a wider range of applications in the future. It is believed that with the efforts of many researchers, the LDHs have great

development prospects in the future and expect that the LDHs can contribute more to the development of science and technology.

### **Acknowledgement**

We gratefully appreciate the support of the Natural Science Foundation of Shandong (ZR2019BB063). The author gratitude the environmental and function material team, supported by the Project of Shandong Province Higher Educational Young Innovative Talent Introduction and Cultivation.

### **Conflict of Interest**

The authors declare that they have no conflict of interest.

### **References**

1. L. Sun, Y. Gong, D. Li and C. Pan, Biomass-derived porous carbon materials: synthesis, designing, and applications for supercapacitors, *Green Chem*, 2022, **24**, 3864-3894.
2. J. Ahmad and K. Majid, In-situ synthesis of visible-light responsive Ag<sub>2</sub>O/graphene oxide nanocomposites and effect of graphene oxide content on its photocatalytic activity, *Adv Compos Hybrid Ma*, 2018, **1**, 374-388.
3. Z. Song, J. Wu, L. Sun, T. Zhu, C. Deng, X. Wang, G. Li, Y. Du, Q. Chen, W. Sun, L. Fan, H. Chen, J. Lin and Z. Lan, Photocapacitor integrating perovskite solar cell and symmetrical supercapacitor generating a conversion storage efficiency over 20 %, *Nano Energy*, 2022, **100**, 107501.
4. C. T. Sarr, M. B. Camara and B. Dakyo, Supercapacitors aging assessment in wind/tidal intermittent energies application with variable temperature, *J Energy Storage*, 2022, **46**, 103790.

5. N. Li, C. Y. Jia, Z. Fang, Z. J. Jiang, A. Ahmed, D. N. Hao, Z. T. Zhang and D. B. Luo, A U-shaped kinetic energy harvester for application in a near-zero energy parking system, *Sustain Cities Soc*, 2022, **81**, 103866.
6. B. R. Ravada, N. R. Tummuru and B. N. L. Ande, Photovoltaic-Wind and Hybrid Energy Storage Integrated Multi-Source Converter Configuration for DC Microgrid Applications, *Ieee T Sustain Energ*, 2021, **12**, 83-91.
7. Y. Lin, X. M. Chen, Y. Tuo, Y. Pan and J. Zhang, In-situ doping-induced lattice strain of NiCoP/S nanocrystals for robust wide pH hydrogen evolution electrocatalysis and supercapacitor, *J Energy Chem*, 2022, **70**, 27-35.
8. X. Chen, S. Z. Li, Y. X. Liu, K. Xie and Y. Q. Wang, MOF-derived Mo-CoP@NiFe LDH hierarchical nanosheets for high-performance hybrid supercapacitors, *J Alloy Compd*, 2022, **919**, 165842.
9. J. J. C. Mancera, J. L. Saenz, E. Lopez, J. M. Andujar, F. S. Manzano, F. J. Vivas and F. Isorna, Experimental analysis of the effects of supercapacitor banks in a renewable DC microgrid, *Appl Energ*, 2022, **308**, 118355.
10. Y. Wei, W. Luo, X. Li, Z. Lin, C. Hou, M. Ma, J. Ding, T. Li and Y. Ma, PANI-MnO<sub>2</sub> and Ti<sub>3</sub>C<sub>2</sub>T<sub>x</sub> (MXene) as electrodes for high-performance flexible asymmetric supercapacitors, *Electrochim Acta*, 2022, **406**, 139874.
11. R. Wang, Z. H. Meng, X. M. Yan, T. Tian, M. Lei, R. A. Pashameah, H. M. Abo-Dief, H. Algadi, N. N. Huang, Z. H. Guo and H. L. Tang, Tellurium intervened Fe-N codoped carbon for improved oxygen reduction reaction and high-performance Zn-air batteries, *J Mater Sci Technol*, 2023, **137**,

- 215-222.
12. C. Jing, Y. F. Zhang, J. J. Zheng, S. S. Ge, J. Lin, D. Pan, N. Naik and Z. H. Guo, In-situ constructing visible light CdS/Cd-MOF photocatalyst with enhanced photodegradation of methylene blue, *Particuology*, 2022, **69**, 111-122.
  13. T. Ma, H. X. Yang and L. Lu, Development of hybrid battery-supercapacitor energy storage for remote area renewable energy systems, *Appl Energ*, 2015, **153**, 56-62.
  14. Q. Q. Li, M. J. Liu, F. Z. Huang, X. Q. Zuo, X. Wei, S. K. Li and H. Zhang, Co<sub>9</sub>S<sub>8</sub>@MnO<sub>2</sub> core-shell defective heterostructure for High-Voltage flexible supercapacitor and Zn-ion hybrid supercapacitor, *Chem Eng J*, 2022, **437**, 135494.
  15. Y. Ma, M. Ma, X. Yin, Q. Shao, N. Lu, Y. Feng, Y. Lu, E. K. Wujcik, X. Mai, C. Wang and Z. Guo, Tuning polyaniline nanostructures via end group substitutions and their morphology dependent electrochemical performances, *Polymer*, 2018, **156**, 128-135.
  16. Y. Ma, Z. Zhuang, M. Ma, Y. Yang, W. Li, M. Dong, S. Wu, T. Ding and Z. Guo, Solid polyaniline dendrites consisting of high aspect ratio branches self-assembled using sodium lauryl sulfonate as soft templates: synthesis and electrochemical performance, *Polymer*, 2019, **182**, 121808.
  17. Y. Zhang, W. F. Cai, Y. J. Guo and Y. Wang, Self-supported Co-Ni-S@CoNi-LDH electrode with a nanosheet-assembled core-shell structure for a high-performance supercapacitor, *J Alloy Compd*, 2022, **908**, 164635.
  18. J. A. Lopez-Villanueva and S. R. Bolivar, Constant Phase Element in the Time Domain: The Problem of Initialization, *Energies*, 2022, **15**, 792.

19. H. J. Liu, J. C. Zhu, Z. Li, Z. C. Shi, J. L. Zhu and H. Mei, Fe<sub>2</sub>O<sub>3</sub>/N doped rGO anode hybridized with NiCo LDH/Co(OH)(2) cathode for battery-like supercapacitor, *Chem Eng J*, 2021, **403**, 126325.
20. Z. X. Wang, X. F. Li, L. Y. Wang, Y. P. Li, J. Y. Qin, P. T. Xie, Y. P. Qu, K. Sun and R. H. Fan, Flexible multi-walled carbon nanotubes/polydimethylsiloxane membranous composites toward high-permittivity performance, *Adv Compos Hybrid Ma*, 2020, **3**, 1-7.
21. J. Wang, Y. Liu, Z. Fan, W. Wang, B. Wang and Z. Guo, Ink-based 3D printing technologies for graphene-based materials: a review, *Adv Compos Hybrid Ma*, 2019, **2**, 1-33.
22. D. Yan, L. Liu, X. Y. Wang, K. Xu and J. H. Zhong, Biomass-Derived Activated Carbon Nanoarchitectonics with Hibiscus Flowers for High-Performance Supercapacitor Electrode Applications, *Chem Eng Technol*, 2022, **45**, 649-657.
23. Y. Ma, C. Hou, H. Zhang, Q. Zhang, H. Liu, S. Wu and Z. Guo, Three-dimensional core-shell Fe<sub>3</sub>O<sub>4</sub>/Polyaniline coaxial heterogeneous nanonets: Preparation and high performance supercapacitor electrodes, *Electrochim Acta*, 2019, **315**, 114-123.
24. Z. Zhuang, W. Wang, Y. Wei, T. Li, M. Ma and Y. Ma, Preparation of polyaniline nanorods/manganese dioxide nanoflowers core/shell nanostructure and investigation of electrochemical performances, *Adv Compos Hybrid Ma*, 2021, **4**, 938-945.
25. M. Zheng, Y. Wei, J. Ren, B. Dai, W. Luo, M. Ma, T. Li and Y. Ma, 2-aminopyridine functionalized magnetic core-shell Fe<sub>3</sub>O<sub>4</sub>@polypyrrole composite for removal of Mn (VII) from aqueous solution by double-layer adsorption, *Sep Purif Technol*, 2021, **277**, 119455.
26. C. D. Ma, J. L. Bai, M. Demir, X. Hu, S. F. Liu and L. L. Wang, Water chestnut shell-derived N/S-

- doped porous carbons and their applications in CO<sub>2</sub> adsorption and supercapacitor, *Fuel*, 2022, **326**, 125119.
27. Y. Ma, C. P. Hou, H. Zhang, M. T. Qiao, Y. H. Chen, H. P. Zhang, Q. Y. Zhang and Z. H. Guo, Morphology-dependent electrochemical supercapacitors in multi-dimensional polyaniline nanostructures, *J Mater Chem A*, 2017, **5**, 14041-14052.
  28. B. Dai, Y. Ma, S. X. Feng, H. W. Wang, M. L. Ma, J. X. Ding, X. Q. Yin and T. X. Li, Fabrication of one-dimensional M (Co, Ni)@polyaniline nanochains with adjustable thickness for excellent microwave absorption properties, *J Colloid Interf Sci*, 2022, **627**, 113-125.
  29. L. A. Chen, X. W. Zheng, C. Y. Hao, Q. D. Sun, P. C. Si, L. J. Ci and J. Wei, Enhanced ions and electrons transmission enables high-performance KxMnO@C cathode for hybrid supercapacitors, *Ceram Int*, 2022, **48**, 16516-16521.
  30. Y. Yang, M. T. Hoang, A. Bhardwaj, M. Wilhelm, S. Mathur and H. Wang, Perovskite solar cells based self-charging power packs: Fundamentals, applications and challenges, *Nano Energy*, 2022, **94**, 106910.
  31. Q. Wu, P. F. Li, Y. H. Wang and F. F. Wu, Construction and electrochemical energy storage performance of free-standing hexagonal Ti<sub>3</sub>C<sub>2</sub> film for flexible supercapacitor, *Appl Surf Sci*, 2022, **593**, 153380.
  32. J. L. Shang, Y. D. Zhang, Q. Zhang, Y. Li, F. Y. Deng, R. J. Gao and J. B. Wang, A novel interlaced NiCoFe hydrotalcite assembled by nanorods and nanosheets with enhanced electrochemical performance for supercapacitor, *J Alloy Compd*, 2022, **925**, 166668.

33. M. A. Aziz, S. S. Shah, S. M. Abu Nayem, M. N. Shaikh, A. S. Hakeem and I. A. Bakare, Peat soil-derived silica doped porous graphitic carbon with high yield for high-performance all-solid-state symmetric supercapacitors, *J Energy Storage*, 2022, **50**, 104278.
34. E. Cevik, S. M. M. Asiri, T. F. Qahtan and A. Bozkurt, Fabrication of high mechanical stability electrodes and bio-electrolytes for high-performance supercapacitor application, *J Alloy Compd*, 2022, **913**, 165230.
35. Y. S. Chen, Z. Yin, D. L. Huang, L. Lei, S. Chen, M. Yan, L. Du, R. H. Xiao and M. Cheng, Uniform polypyrrole electrodeposition triggered by phytic acid-guided interface engineering for high energy density flexible supercapacitor, *J Colloid Interf Sci*, 2022, **611**, 356-365.
36. F. Ran, X. Yang and L. Shao, Recent progress in carbon-based nanoarchitectures for advanced supercapacitors, *Adv Compos Hybrid Ma*, 2018, **1**, 32-55.
37. K. Dericiler, A. Kocanali, M. Buldu-Akturk, E. Erdem and B. Saner Okan, Upcycling process of transforming waste coffee into spherical graphene by flash pyrolysis for sustainable supercapacitor manufacturing with virgin graphene electrodes and its comparative life cycle assessment, *Biomass Convers Bior*, 2022, DOI: <https://doi.org/10.1007/s13399-022-02447-8>.
38. X. Li, Z. Lin, Y. Wei, W. Luo, J. Ding, T. Li and Y. Ma, MXene-MnO<sub>2</sub>-CoNi layered double hydroxides//activated carbon flexible asymmetric supercapacitor, *Journal of Energy Storage*, 2022, **55**, 105668.
39. H. Wei, A. Li, D. Kong, Z. Li, D. Cui, T. Li, B. Dong and Z. Guo, Polypyrrole/reduced graphene aerogel film for wearable piezoresistive sensors with high sensing performances, *Adv Compos*



- Hybrid Ma*, 2021, **4**, 86-95.
40. S. Islam, M. M. Mia, S. S. Shah, S. Naher, M. N. Shaikh, M. A. Aziz and A. J. S. Ahammad, Recent Advancements in Electrochemical Deposition of Metal-Based Electrode Materials for Electrochemical Supercapacitors, *Chem Rec*, 2022, **22**, e202200013.
  41. C. L. Liu, Q. Li and K. Wang, State-of-charge estimation and remaining useful life prediction of supercapacitors, *Renew Sust Energ Rev*, 2021, **150**, 111408.
  42. H. Liu, H. B. Wang, X. H. Lu, V. Murugadoss, M. N. Huang, H. S. Yang, F. X. Wan, D. G. Yu and Z. H. Guo, Electrospun structural nanohybrids combining three composites for fast helicid delivery, *Adv Compos Hybrid Ma*, 2022, **5**, 1017-1029.
  43. D. Wei, M. M. Weng, M. H. H. Mahmoud, A. Y. Elnaggar, I. H. El Azab, X. X. Sheng, M. N. Huang, Z. M. El-Bahy and J. T. Huang, Development of novel biomass hybrid aerogel supported composite phase change materials with improved light-thermal conversion and thermal energy storage capacity, *Adv Compos Hybrid Ma*, 2022, **5**, 1910-1921.
  44. P. Huo, S. Ni, P. Hou, Z. Xun, Y. Liu and J. Gu, A Crosslinked Soybean Protein Isolate Gel Polymer Electrolyte Based on Neutral Aqueous Electrolyte for a High-Energy-Density Supercapacitor, *Polymers-Basel*, 2019, **11**, 31086006.
  45. D. S. Kong, Z. M. El-Bahy, H. Algadi, T. Li, S. M. El-Bahy, M. A. Nassan, J. R. Li, A. A. Faheim, A. Li, C. X. Xu, M. N. Huang, D. P. Cui and H. G. Wei, Highly sensitive strain sensors with wide operation range from strong MXene-composited polyvinyl alcohol/sodium carboxymethylcellulose double network hydrogel, *Adv Compos Hybrid Ma*, 2022, **5**, 1976-1987.

46. X. Jin, L. Song, C. Dai, H. Ma, Y. Xiao, X. Zhang, Y. Han, X. Li, J. Zhang, Y. Zhao, Z. Zhang, L. Duan and L. Qu, A self-healing zinc ion battery under -20 °C, *Energy Storage Mater*, 2022, **44**, 517-526.
47. X. Jin, L. Song, C. Dai, Y. Xiao, Y. Han, X. Li, Y. Wang, J. Zhang, Y. Zhao, Z. Zhang, N. Chen, L. Jiang and L. Qu, A Flexible Aqueous Zinc-Iodine Microbattery with Unprecedented Energy Density, *Adv Mater*, 2022, **34**, 2109450.
48. X. Jin, L. Song, H. Yang, C. Dai, Y. Xiao, X. Zhang, Y. Han, C. Bai, B. Lu, Q. Liu, Y. Zhao, J. Zhang, Z. Zhang and L. Qu, Stretchable supercapacitor at -30 °C, *Energ Environ Sci*, 2021, **14**, 3075-3085.
49. X. Jin, L. Song, C. Dai, Y. Xiao, Y. Han, X. Zhang, X. Li, C. Bai, J. Zhang, Y. Zhao, Z. Zhang, L. Jiang and L. Qu, An Aqueous Anti-Freezing and Heat-Tolerant Symmetric Microsupercapacitor with 2.3 V Output Voltage, *Adv Energy Mater*, 2021, **11**, 2101523.
50. L. Song, C. Dai, X. Jin, Y. Xiao, Y. Han, Y. Wang, X. Zhang, X. Li, S. Zhang, J. Zhang, Y. Zhao, Z. Zhang and L. Qu, Pure Aqueous Planar Microsupercapacitors with Ultrahigh Energy Density under Wide Temperature Ranges, *Adv Funct Mater*, 2022, **32**, 2203270.
51. S. Kumar, G. Saeed, L. Zhu, K. N. Hui, N. H. Kim and J. H. Lee, 0D to 3D carbon-based networks combined with pseudocapacitive electrode material for high energy density supercapacitor: A review, *Chem Eng J*, 2021, **403**, 126352.
52. X. J. Liu, M. Gao, J. Y. Chen, S. Guo, W. Zhu, L. C. Bai, W. Z. Zhai, H. J. Du, H. Wu, C. Z. Yan, Y. S. Shi, J. W. Gu, H. J. Qi and K. Zhou, Recent Advances in Stimuli-Responsive Shape-Morphing Hydrogels, *Adv Funct Mater*, 2022, **32**, 2203323.

53. T. Z. Guo, D. Zhou, L. X. Pang, S. K. Sun, T. Zhou and J. Z. Su, Perspectives on Working Voltage of Aqueous Supercapacitors, *Small*, 2022, **18**, e2106360.
54. Y. Wei, W. Luo, Z. Zhuang, B. Dai, J. Ding, T. Li, M. Ma, X. Yin and Y. Ma, Fabrication of ternary MXene/MnO<sub>2</sub>/polyaniline nanostructure with good electrochemical performances, *Adv Compos Hybrid Ma*, 2021, **4**, 1082-1091.
55. M. Athanasiou, S. N. Yannopoulos and T. Ioannides, Biomass-derived graphene-like materials as active electrodes for supercapacitor applications: A critical review, *Chem Eng J*, 2022, **446**, 137191.
56. K. Krishnamoorthy, P. Pazhamalai, S. Manoharan, N. U. L. Ali and S. J. Kim, Recent trends, challenges, and perspectives in piezoelectric-driven self-chargeable electrochemical supercapacitors, *Carbon Energy*, 2022, **4**, 833-855.
57. S. P. Ega and P. Srinivasan, Quinone materials for supercapacitor: Current status, approaches, and future directions, *J Energy Storage*, 2022, **47**, 103700.
58. M. Dhanda, R. Arora, S. Ahlawat, S. P. Nehra and S. Lata, Electrolyte as a panacea to contemporary scientific world of super-capacitive energy: A condense report, *J Energy Storage*, 2022, **52**, 104740.
59. K. P. Ruan and J. W. Gu, Ordered Alignment of Liquid Crystalline Graphene Fluoride for Significantly Enhancing Thermal Conductivities of Liquid Crystalline Polyimide Composite Films, *Macromolecules*, 2022, **55**, 4134-4145.
60. D. Mohanadas and Y. Sulaiman, Recent advances in development of electroactive composite materials for electrochromic and supercapacitor applications, *J Power Sources*, 2022, **523**, 231029.
61. N. N. Loganathan, V. Perumal, B. R. Pandian, R. Atchudan, T. Edison and M. Ovinis, Recent studies

- on polymeric materials for supercapacitor development, *J Energy Storage*, 2022, **49**, 104937.
62. M. M. Amaral, R. Venancio, A. C. Peterlevitz and H. Zanin, Recent advances on quasi-solid-state electrolytes for supercapacitors, *J Energy Chem*, 2022, **67**, 697-717.
  63. H. Wei, H. Gu, J. Guo, D. Cui, X. Yan, J. Liu, D. Cao, X. Wang, S. Wei and Z. Guo, Significantly enhanced energy density of magnetite/polypyrrole nanocomposite capacitors at high rates by low magnetic fields, *Adv Compos Hybrid Ma*, 2017, **1**, 127-134.
  64. J. Kumar, H. J. Jung, R. R. Neiber, R. A. Soomro, Y. J. Kwon, N. Ul Hassan, M. Shon, J. H. Lee, K. Y. Baek and K. Y. Cho, Recent advances in oxygen deficient metal oxides: Opportunities as supercapacitor electrodes, *Int J Energ Res*, 2022, **46**, 7055-7081.
  65. Y. Wei, M. Zheng, W. Luo, B. Dai, J. Ren, M. Ma, T. Li and Y. Ma, All pseudocapacitive MXene-MnO<sub>2</sub> flexible asymmetric supercapacitor, *J Energy Storage*, 2022, **45**, 103715.
  66. J. Chen, Y. Huang, X. Ma and Y. Lei, Functional self-healing materials and their potential applications in biomedical engineering, *Adv Compos Hybrid Ma*, 2018, **1**, 94-113.
  67. F. F. Xing, Z. H. Bi, F. Su, F. Y. Liu and Z. S. Wu, Unraveling the Design Principles of Battery-Supercapacitor Hybrid Devices: From Fundamental Mechanisms to Microstructure Engineering and Challenging Perspectives, *Adv Energy Mater*, 2022, **12**, 2200594.
  68. B. Joshi, E. Samuel, Y. I. Kim, A. L. Yarin, M. T. Swihart and S. S. Yoon, Review of recent progress in electrospinning-derived freestanding and binder-free electrodes for supercapacitors, *Coordin Chem Rev*, 2022, **460**, 214466.
  69. R. Vinodh, R. S. Babu, S. Sambasivam, C. Gopi, S. Alzahmi, H. J. Kim, A. L. F. de Barros and I. M.

- Obaidat, Recent Advancements of Polyaniline/Metal Organic Framework (PANI/MOF) Composite Electrodes for Supercapacitor Applications: A Critical Review, *Nanomaterials-Basel*, 2022, **12**, 1511.
70. N. R. Chodankar, H. D. Pham, A. K. Nanjundan, J. F. S. Fernando, K. Jayaramulu, D. Golberg, Y. K. Han and D. P. Dubal, True Meaning of Pseudocapacitors and Their Performance Metrics: Asymmetric versus Hybrid Supercapacitors, *Small*, 2020, **16**, e2002806.
71. C. Li, L. Sha, K. Yang, F. Kong, P. Li, Y. Tao, X. Zhao and H. Chen, Effects of ultrafiltration on Co-Metal Organic Framework/pre-hydrolysis solution carbon materials for supercapacitor energy storage, *Front Chem*, 2022, **10**, 991230.
72. Y. Guo, H. Liu, D. D. Wang, Z. M. El-Bahy, J. T. Althakafy, H. M. Abo-Dief, Z. H. Guo, B. B. Xu, C. T. Liu and C. Y. Shen, Engineering hierarchical heterostructure material based on metal-organic frameworks and cotton fiber for high-efficient microwave absorber, *Nano Res*, 2022, **15**, 6841-6850.
73. Z. Fahimi, O. Moradlou, A. Sabbah, K. H. Chen, L. C. Chen and M. Qorbani,  $\text{Co}_3\text{V}_2\text{O}_8$  hollow spheres with mesoporous walls as high-capacitance electrode for hybrid supercapacitor device, *Chem Eng J*, 2022, **436**, 135225.
74. Y. Tian, X. Yang, A. Nautiyal, Y. Zheng, Q. Guo, J. Luo and X. Zhang, One-step microwave synthesis of  $\text{MoS}_2/\text{MoO}_3$ @graphite nanocomposite as an excellent electrode material for supercapacitors, *Adv Compos Hybrid Ma*, 2019, **2**, 151-161.
75. B. Jain, A. Hashmi, S. Sanwaria, A. K. Singh, M. A. B. H. Susan and A. Singh, Zinc oxide nanoparticle incorporated on graphene oxide: an efficient and stable photocatalyst for water

- treatment through the Fenton process, *Adv Compos Hybrid Ma*, 2020, **3**, 231-242.
76. O. Gerard, A. Numan, S. Krishnan, M. Khalid, R. Subramaniam and R. Kasi, A review on the recent advances in binder-free electrodes for electrochemical energy storage application, *J Energy Storage*, 2022, **50**, 104283.
  77. Y. T. Wang, X. F. He, G. Y. He, C. Meng, X. M. Chen, F. T. Li and Y. Zhou, A critical review on nickel sulfide-based electrode materials for supercapacitors, *Crit Rev Solid State*, 2022, DOI: <https://doi.org/10.1080/10408436.2022.2078276>.
  78. T. Wang, J. Q. Lei, Y. Wang, L. Pang, F. P. Pan, K. J. Chen and H. X. Wang, Approaches to Enhancing Electrical Conductivity of Pristine Metal-Organic Frameworks for Supercapacitor Applications, *Small*, 2022, **18**, e2203307.
  79. K. Y. Zhang, Z. Y. Ma, H. Deng and Q. Fu, Improving high-temperature energy storage performance of PI dielectric capacitor films through boron nitride interlayer, *Adv Compos Hybrid Ma*, 2022, **5**, 238-249.
  80. Y. Wang, Y.-J. Hu, X. Hao, P. Peng, J.-Y. Shi, F. Peng and R.-C. Sun, Hydrothermal synthesis and applications of advanced carbonaceous materials from biomass: a review, *Adv Compos Hybrid Ma*, 2020, **3**, 267-284.
  81. S. Li, C. Yang, S. Sarwar, A. Nautiyal, P. Zhang, H. Du, N. Liu, J. Yin, K. Deng and X. Zhang, Facile synthesis of nanostructured polyaniline in ionic liquids for high solubility and enhanced electrochemical properties, *Adv Compos Hybrid Ma*, 2019, **2**, 279-288.
  82. S. V. Sadavar, N. S. Padalkar, R. B. Shinde, S. T. Kochuveedu, U. M. Patil, A. S. Patil, R. N. Bulakhe,

- C. D. Lokhande, I. In, R. R. Salunkhe and J. L. Gunjekar, Mesoporous nanohybrids of 2-D Cobalt-Chromium layered double hydroxide and polyoxovanadate anions for high performance hybrid asymmetric supercapacitors, *J Power Sources*, 2022, **524**, 231065.
83. J. Zhao, Y. Guo, Y. Q. Yang, Z. Shen, Q. Wu, L. J. Yang, X. Z. Wang and Z. Hu, Insight into the decay mechanism of cycling capacitance for layered double hydroxides at subnanometer scale, *Chem Commun*, 2022, **58**, 9124-9127.
84. L. Xiao, H. Qi, K. Qu, C. Shi, Y. Cheng, Z. Sun, B. Yuan, Z. Huang, D. Pan and Z. Guo, Layer-by-layer assembled free-standing and flexible nanocellulose/porous  $\text{Co}_3\text{O}_4$  polyhedron hybrid film as supercapacitor electrodes, *Adv Compos Hybrid Ma*, 2021, **4**, 306-316.
85. L. Pu, J. Zhang, N. K. L. Jiresse, Y. Gao, H. Zhou, N. Naik, P. Gao and Z. Guo, N-doped MXene derived from chitosan for the highly effective electrochemical properties as supercapacitor, *Adv Compos Hybrid Ma*, 2022, **5**, 356-369.
86. C. Z. Yin, C. Wang and Q. Hu, Selective removal of As(V) from wastewater with high efficiency by glycine-modified Fe/Zn-layered double hydroxides, *Adv Compos Hybrid Ma*, 2021, **4**, 360-370.
87. Y. F. Wu, Y. C. Hsiao, C. H. Liao, C. S. Hsu, S. Yougbare and L. Y. Lin, Novel design of Sulfur-doped nickel cobalt layered double hydroxide and polypyrrole nanotube composites from zeolitic imidazolate Framework-67 as efficient active material of battery supercapacitor hybrids, *J Colloid Interface Sci*, 2022, **628**, 540-552.
88. Y. F. Wu, Y. C. Hsiao, C. H. Liao, C. S. Hsu, S. Yougbare and L. Y. Lin, Novel design of Sulfur-doped nickel cobalt layered double hydroxide and polypyrrole nanotube composites from zeolitic



- imidazolate Framework-67 as efficient active material of battery supercapacitor hybrids, *J Colloid Interf Sci*, 2022, **628**, 540-552.
89. X. Ge, C. D. Gu, X. L. Wang and J. P. Tu, Ionothermal synthesis of cobalt iron layered double hydroxides (LDHs) with expanded interlayer spacing as advanced electrochemical materials, *J Mater Chem A*, 2014, **2**, 17066-17076.
  90. R. B. Tang, P. Xu, J. W. Dong, H. G. Gui, T. Zhang, Y. S. Ding, V. Murugadoss, N. Naik, D. Pan, M. N. Huang and Z. H. Guo, Carbon foams derived from emulsion-templated porous polymeric composites for electromagnetic interference shielding, *Carbon*, 2022, **188**, 492-502.
  91. L. H. Wang, D. D. Jia, L. J. Yue, K. Zheng, A. T. Zhang, Q. Jia and J. Q. Liu, In Situ Fabrication of a Uniform Co-MOF Shell Coordinated with CoNiO<sub>2</sub> to Enhance the Energy Storage Capability of NiCo-LDH via Vapor-Phase Growth, *ACS Appl Mater Inter*, 2020, **12**, 47526-47538.
  92. Saba Jamil, Afaaf Rahat Alvi, hanza Rauf Khan and M. R. S. A. Janjua, Layered Double Hydroxides(LDHs): Synthesis & Applications, *Prog Chem*, 2018, **31**, 394-412.
  93. L. Hui, Y. R. Xue, B. L. Huang, H. D. Yu, C. Zhang, D. Y. Zhang, D. Z. Jia, Y. J. Zhao, Y. J. Li, H. B. Liu and Y. L. Li, Overall water splitting by graphdiyne-exfoliated and -sandwiched layered double-hydroxide nanosheet arrays, *Nat Commun*, 2018, **9**, 5309.
  94. L. Wang, Z. L. Ma, H. Qiu, Y. L. Zhang, Z. Yu and J. W. Gu, Significantly Enhanced Electromagnetic Interference Shielding Performances of Epoxy Nanocomposites with Long-Range Aligned Lamellar Structures, *Nano-Micro Lett*, 2022, **14**, 224.
  95. B. Zhao, Z. L. Ma, Y. Y. Sun, Y. X. Han and J. W. Gu, Flexible and Robust Ti<sub>3</sub>C<sub>2</sub>T<sub>x</sub>/(ANF (R) FeNi)

- Composite Films with Outstanding Electromagnetic Interference Shielding and Electrothermal Conversion Performances, *Small Struct*, 2022, **3**, 2200162.
96. P. F. Li, X. Q. Liu, M. Arif, H. L. Yan, C. Y. Hu, S. M. Chen and X. H. Liu, In situ growth of glucose-intercalated LDHs on NiCo<sub>2</sub>S<sub>4</sub> hollow nanospheres to enhance energy storage capacity for hybrid supercapacitors, *Colloid Surface A*, 2022, **644**, 128823.
  97. Z. Y. Xiao, Y. J. Mei, S. Yuan, H. Mei, B. Xu, Y. X. Bao, L. L. Fan, W. P. Kang, F. N. Dai, R. M. Wang, L. Wang, S. Q. Hu, D. F. Sun and H. C. Zhou, Controlled Hydrolysis of Metal-Organic Frameworks: Hierarchical Ni/Co-Layered Double Hydroxide Microspheres for High-Performance Supercapacitors, *ACS Nano*, 2019, **13**, 7024-7030.
  98. J. Ni, X. Huang, Y. Bai, B. Zhao, Y. Han, S. Han, T. Xu, C. Si and C. Zhang, Resistance to aggregation-caused quenching: chitosan-based solid carbon dots for white light-emitting diode and 3D printing, *Adv Compos Hybrid Ma*, 2022, **5**, 1865-1875.
  99. C. Jing, B. Dong and Y. Zhang, Chemical Modifications of Layered Double Hydroxides in the Supercapacitor, *Energy Environ Mater*, 2020, **3**, 346-379.
  100. G. Li, Y. Ji, D. Zuo, J. Xu and H. Zhang, Carbon electrodes with double conductive networks for high-performance electrical double-layer capacitors, *Adv Compos Hybrid Ma*, 2019, **2**, 456-461.
  101. Y. Guo, D. Wang, T. Bai, H. Liu, Y. Zheng, C. Liu and C. Shen, Electrostatic self-assembled NiFe<sub>2</sub>O<sub>4</sub>/Ti<sub>3</sub>C<sub>2</sub>T<sub>x</sub> MXene nanocomposites for efficient electromagnetic wave absorption at ultralow loading level, *Adv Compos Hybrid Ma*, 2021, **4**, 602-613.
  102. K. Qu, Z. Sun, C. Shi, W. Wang, L. Xiao, J. Tian, Z. Huang and Z. Guo, Dual-acting cellulose

- nanocomposites filled with carbon nanotubes and zeolitic imidazolate framework-67 (ZIF-67)-derived polyhedral porous  $\text{Co}_3\text{O}_4$  for symmetric supercapacitors, *Adv Compos Hybrid Ma*, 2021, **4**, 670-683.
103. P. Wang, T. Song, H. M. Abo-Dief, J. Song, A. K. Alanazi, B. Fan, M. Huang, Z. Lin, A. A. Altalhi, S. Gao, L. Yang, J. Liu, S. Feng and T. Cao, Effect of carbon nanotubes on the interface evolution and dielectric properties of polylactic acid/ethylene-vinyl acetate copolymer nanocomposites, *Adv Compos Hybrid Ma*, 2022, **5**, 1100-1110.
  104. Q. X. Wu, Z. P. Feng, Z. M. Cai, C. W. Lan, J. C. Xu, K. Bi and Y. N. Hao, Poly(methyl methacrylate)-based ferroelectric/dielectric laminated films with enhanced energy storage performances, *Adv Compos Hybrid Ma*, 2022, **5**, 1137-1144.
  105. H. Liu, T. Xu, Q. Liang, Q. Zhao, D. Zhao and C. Si, Compressible cellulose nanofibrils/reduced graphene oxide composite carbon aerogel for solid-state supercapacitor, *Adv Compos Hybrid Ma*, 2022, **5**, 1168-1179.
  106. M. Xu and M. Wei, Layered Double Hydroxide-Based Catalysts: Recent Advances in Preparation, Structure, and Applications, *Adv Funct Mater*, 2018, **28**, 1802943.
  107. H. Zhang, X. B. Liang, Y. L. Hu, P. Zhang, L. W. Yang, D. Y. He, M. Y. Hua and Y. G. Tong, Correlation of C/C preform density and microstructure and mechanical properties of C/C-ZrC-based ultra-high-temperature ceramic matrix composites, *Adv Compos Hybrid Ma*, 2021, **4**, 743-750.
  108. H. Y. Du, Y. L. An, Y. H. Wei, X. D. Liu, L. F. Hou, B. S. Liu, M. M. Liu and P. K. Liaw, Experimental and numerical studies on strength and ductility of gradient-structured iron plate obtained by surface

- mechanical-attrition treatment, *Mat Sci Eng A-Struct*, 2019, **744**, 471-480.
109. Y. Y. Wang, D. F. Yan, S. El Hankari, Y. Q. Zou and S. Y. Wang, Recent Progress on Layered Double Hydroxides and Their Derivatives for Electrocatalytic Water Splitting, *Adv Sci*, 2018, **5**, 1800064.
  110. G. L. Fan, F. Li, D. G. Evans and X. Duan, Catalytic applications of layered double hydroxides: recent advances and perspectives, *Chem Soc Rev*, 2014, **43**, 7040-7066.
  111. Y. T. Guo, N. Meng, J. Xu, K. N. Zhang, Q. Q. Zhang, E. Pawlikowska, M. Szafran and F. Gao, Microstructure and dielectric properties of Ba<sub>0.6</sub>Sr<sub>0.4</sub>TiO<sub>3</sub>/(acrylonitrile-butadiene-styrene)-poly(vinylidene fluoride) composites, *Adv Compos Hybrid Ma*, 2019, **2**, 681-689.
  112. L. Guo, Y. F. Zhang, J. J. Zheng, L. Q. Shang, Y. J. Shi, Q. Wu, X. X. Liu, Y. M. Wang, L. Q. Shi and Q. Shao, Synthesis and characterization of ZnNiCr-layered double hydroxides with high adsorption activities for Cr(VI), *Adv Compos Hybrid Ma*, 2021, **4**, 819-829.
  113. G. Li, L. Wang, X. Lei, Z. Peng, T. Wan, S. Maganti, M. Huang, V. Murugadoss, I. Seok, Q. Jiang, D. Cui, A. Alhadhrami, M. M. Ibrahim and H. Wei, Flexible, yet robust polyaniline coated foamed polylactic acid composite electrodes for high-performance supercapacitors, *Adv Compos Hybrid Ma*, 2022, **5**, 853-863.
  114. Z. Chen, Q. Fan, M. Huang and H. Cölfen, Synthesis of two-dimensional layered double hydroxides: a systematic overview, *Crystengcomm*, 2022, **24**, 4639-4655.
  115. M. Khorshidi, S. Asadpour, N. Sarmast and M. Dinari, A review of the synthesis methods, properties, and applications of layered double hydroxides/carbon nanocomposites, *J Mol Liq*, 2022, **348**, 118399.

116. A. Kim, I. Varga, A. Adhikari and R. Patel, Recent Advances in Layered Double Hydroxide-Based Electrochemical and Optical Sensors, *Nanomaterials-Basel*, 2021, **11**, 2809.
117. G. Wei, J. M. Zhang, M. Usuelli, X. F. Zhang, B. Liu and R. Mezzenga, Biomass vs inorganic and plastic-based aerogels: Structural design, functional tailoring, resource-efficient applications and sustainability analysis, *Prog Mater Sci*, 2022, **125**, 100915.
118. Y. Ma, X. Xie, W. Yang, Z. Yu, X. Sun, Y. Zhang, X. Yang, H. Kimura, C. Hou, Z. Guo and W. Du, Recent advances in transition metal oxides with different dimensions as electrodes for high-performance supercapacitors, *Adv Compos Hybrid Ma*, 2021, **4**, 906-924.
119. N. S. Padalkar, S. V. Sadavar, R. B. Shinde, A. S. Patil, U. M. Patil, V. V. Magdum, Y. M. Chitare, S. P. Kulkarni, R. N. Bulakhe, V. G. Parale and J. L. Gunjekar, 2D-2D nanohybrids of Ni-Cr-layered double hydroxide and graphene oxide nanosheets: Electrode for hybrid asymmetric supercapacitors, *Electrochim Acta*, 2022, **424**, 140615.
120. N. Wang, H. W. Pang, S. J. Yu, P. C. Gu, S. Song, H. Q. Wang and X. K. Wang, Investigation of Adsorption Mechanism of Layered Double Hydroxides and Their Composites on Radioactive Uranium: A Review, *Acta Chim Sinica*, 2019, **77**, 143-152.
121. Z. Yang, L. Han, X. Fu, Y. Wang, H. Huang and M. Xu, Double-safety flexible supercapacitor basing on zwitterionic hydrogel: over-heat alarm and flame-retardant electrolyte, *Adv Compos Hybrid Ma*, 2022, **5**, 1876-1887.
122. Y. Wang, D. Yang, M. M. Hessien, K. Du, M. M. Ibrahim, Y. Su, G. A. M. Mersal, R. Ma, S. M. El-Bahy, M. Huang, Q. Yuan, B. Cui and D. Hu, Flexible barium

- titanate@polydopamine/polyvinylidene fluoride/polymethyl methacrylate nanocomposite films with high performance energy storage, *Adv Compos Hybrid Ma*, 2022, **5**, 2106-2115.
123. B. Li, M. Guo, X. Chen and Y. Miao, Hydrothermally synthesized N and S co-doped mesoporous carbon microspheres from poplar powder for supercapacitors with enhanced performance, *Adv Compos Hybrid Ma*, 2022, **5**, 2306-2316.
  124. Y. Wen, Y. Zhao, L. Lu, S. J. Zhang and B. Xu, Electrochemical Performance of Zn-Al Double Layered Hydroxide for Supercapacitor Application, *3rd Annual International Workshop on Materials Science and Engineering (Iwmse2017)*, 2017, **250**, 012055.
  125. B. R. Wiston, P. Prabhakaran and M. Ashok, Bimetallic NiFe hydroxide coated onto commercial graphite foil as efficient supercapacitor electrode, *J Energy Storage*, 2022, **50**, 104226.
  126. Q. Xiao, Y. Yuan, J. Zhu, Z. Shi, Z. Li and J. Zhu, Carbonate doped nickel-cobalt layered double hydroxide for high performance asymmetric supercapacitors, *J Alloy Compd*, 2022, **916**, 165391.
  127. G. Wang, Y. Li, T. Zhao and Z. Jin, Phosphatized mild-prepared-NiCo LDHs cabbage-like spheres exhibit excellent performance as a supercapacitor electrode, *New J Chem*, 2021, **45**, 251-261.
  128. Z. Wang, K. Yin, Y. Zhang, K. Sun, L. Xie, M. Cong, S. Cao, Y. Lei, X. Li and R. Fan, Two-dimensional  $\text{Ti}_3\text{C}_2\text{T}_x$ /carbonized wood metacomposites with weakly negative permittivity, *Adv Compos Hybrid Ma*, 2022, **5**, 2369-2377.
  129. Y. Li, B. Huang, X. Zhao and Z. Luo, Zeolitic imidazolate framework-L-assisted synthesis of inorganic and organic anion-intercalated hetero-trimetallic layered double hydroxide sheets as advanced electrode materials for aqueous asymmetric super-capacitor battery, *J Power Sources*,

- 2022, **527**, 231149.
130. J. Wang, Z. Wang, N. Liu, C. Liu, J. Yan, C. C. Li, J. Cui, J. Liu, X. Hu and Y. Wu, Al doped Ni-Co layered double hydroxides with surface-sulphuration for highly stable flexible supercapacitors, *J Colloid Interface Sci*, 2022, **615**, 173-183.
  131. W. Zhang, H. Fan, Q. Liu, N. Ta, Y. Pu, X. Chen, Y. Sui, E. Wang and P. Cao, Nickel-rich NiCo LDHs supported on hollow carbon shells for hybrid supercapacitors, *Electrochim Acta*, 2021, **395**, 139167.
  132. L. Wan, Y. M. Wang, C. Du, J. Chen, M. J. Xie, Y. P. Wu and Y. Zhang, NiAlP@Cobalt substituted nickel carbonate hydroxide heterostructure engineered for enhanced supercapacitor performance, *J Colloid Interf Sci*, 2022, **609**, 1-11.
  133. F. B. M. Ahmed, D. Khalafallah, M. Zhi and Z. Hong, Porous nanoframes of sulfurized NiAl layered double hydroxides and ternary bismuth cerium sulfide for supercapacitor electrodes, *Adv Compos Hybrid Ma*, 2022, **5**, 2500-2514.
  134. F. Z. Janani, N. Taoufik, H. Khiar, W. Boumya, A. Elhalil, M. Sadiq, A. V. Puga and N. Barka, Nanostructured layered double hydroxides based photocatalysts: Insight on synthesis methods, application in water decontamination/splitting and antibacterial activity, *Surf Interfaces*, 2021, **25**, 101263.
  135. C. Y. Li, Y. J. Zhou, X. Li, H. Q. Wang, P. W. Huo and X. K. Wang, Ni doping Co<sub>2</sub>Al ternary layered double hydroxides for improving electrochemical performance of high-performance hybrid supercapacitors, *Appl Surf Sci*, 2021, **536**, 147780.



136. D. A. Reddy, K. A. J. Reddy, M. Gopannagari, Y. Kim, A. P. Rangappa, D. P. Kumar and T. K. Kim, Exposure of NiFe-LDH active sites by cation-exchange to promote photoelectrochemical water splitting performance, *Appl Surf Sci*, 2021, **570**, 151134.
137. R. Aladpoosh and M. Montazer, Functionalization of cellulose fibers alongside growth of 2D LDH platelets through urea hydrolysis inspired Taro wettability, *Carbohydr Polym*, 2022, **275**, 118584.
138. Nikhil, G. P. Ji and R. Prakash, Hydrothermal synthesis of Zn-Mg-based layered double hydroxide coatings for the corrosion protection of copper in chloride and hydroxide media, *Int J Min Met Mater*, 2021, **28**, 1991-2000.
139. Z. Q. Liu, Y. X. Zhong, Y. L. Qiu, L. Cui, W. R. Yang, J. M. Razal, C. J. Barrow and J. Q. Liu, Multilayered and hierarchical structured NiCo double hydroxide nanosheets generated on porous MgCo<sub>2</sub>O<sub>4</sub> nanowire arrays for high performance supercapacitors, *Appl Surf Sci*, 2021, **546**, 149133.
140. Z. Meng, W. Yan, M. Zou, H. Miao, F. Ma, A. B. Patil, R. Yu, X. Yang Liu and N. Lin, Tailoring NiCoAl layered double hydroxide nanosheets for assembly of high-performance asymmetric supercapacitors, *J Colloid Interface Sci*, 2021, **583**, 722-733.
141. C. Lai, Y. Guo, H. Zhao, H. Song, X. Qu, M. Huang, S. W. Hong and K. Lee, High-performance double “ion-buffering reservoirs” of asymmetric supercapacitors enabled by battery-type hierarchical porous sandwich-like Co<sub>3</sub>O<sub>4</sub> and 3D graphene aerogels, *Adv Compos Hybrid Ma*, 2022, **5**, 2557-2574.
142. Y. Li, X. Yan, W. Zhang, W. Zhou, Y. Zhu, M. Zhang, W. Zhu and X. Cheng, Hierarchical micro-nano structure based NiCoAl-LDH nanosheets reinforced by NiCo<sub>2</sub>S<sub>4</sub> on carbon cloth for

- asymmetric supercapacitor, *J Electroanal Chem*, 2022, **905**, 115982.
143. T. T. Nguyen, D. Mohapatra, D. R. Kumar, M. Baynosa, S. Sahoo, J. Lee and J.-J. Shim, Direct growth of nickel cobalt layered double hydroxide on nickel foam via redox reaction between nitrate ion and ethanol for hybrid supercapacitors, *Electrochim Acta*, 2021, **367**, 137226.
  144. Y. Xue, X. Liu, L. Han, Z. Xie, L. Liu, Y. Li, Y. Hua, C. Wang, X. Zhao and X. Liu, Fabrication of hierarchical NiCo<sub>2</sub>S<sub>4</sub> nanotubes@NiMn-LDH nanosheets core-shell hybrid arrays on Ni foam for high-performance asymmetric supercapacitors, *J Alloy Compd*, 2022, **900**, 163495.
  145. W. Yan, Y. Zhang, T. Zeng, Y. Zhang, Q. Wan and N. Yang, A high-performance asymmetric supercapacitor using composite electrodes of layered double hydroxides and holey reduced graphene oxide, *J Energy Storage*, 2022, **52**, 104899.
  146. X. Wang, Y. Sun, W. Zhang, J. Liu and X. Wu, Hierarchical Cu<sub>0.92</sub>Co<sub>2.08</sub>O<sub>4</sub>@NiCo-layered double hydroxide nanoarchitecture for asymmetric flexible storage device, *Mater Today Sustain*, 2022, **17**, 100097.
  147. H. Fu, A. Zhang, F. Jin, H. Guo and J. Liu, Ternary NiCeCo-Layered Double Hydroxides Grown on CuBr<sub>2</sub>@ZIF-67 Nanowire Arrays for High-Performance Supercapacitors, *ACS Appl Mater Interfaces*, 2022, **14**, 16165-16177.
  148. L. Wang and N. Zhou, Construction of sulfide nanoparticles on hydrangea-like nickel-cobalt hydroxide for enhanced pseudocapacitance, *J Energy Storage*, 2022, **53**, 105097.
  149. G. Liu, G. Wang, X. Guo, X. Hao and Z. Jin, Toiless sulfuration route to enhance the supercapacitor performance of nanoflower-like NiAl-layered double hydroxide, *J Electroanal Chem*, 2022, **916**,

- 116368.
150. G. Liu, G. Wang, X. Guo, X. Hao, K. Wang and Z. Jin, Toilless selenylation route to enhance the supercapacitor conductive performance of nanoflower-like NiAl-layered double hydroxide, *J Energy Storage*, 2022, **52**, 104968.
  151. Y. Liu, C. Yu, H. Che, Z. Guo, J. Mu, X. Zhang and A. Liu, Ag nanoparticles-decorated CoAl-layered double hydroxide flower-like hollow microspheres for enhanced energy storage performance, *J Colloid Interface Sci*, 2021, **581**, 485-495.
  152. S. Islam, M. M. Mia, S. S. Shah, S. Naher, M. N. Shaikh, M. A. Aziz and A. J. S. Ahammad, Recent Advancements in Electrochemical Deposition of Metal-Based Electrode Materials for Electrochemical Supercapacitors, *Chem Rec*, 2022, **22**, e202200013.
  153. F. C. Yao, W. H. Xie, C. Ma, D. D. Wang, Z. M. El-Bahy, M. H. Helal, H. Liu, A. Du, Z. H. Guo and H. B. Gu, Superb electromagnetic shielding polymer nanocomposites filled with 3-dimensional p-phenylenediamine/aniline copolymer nanofibers@copper foam hybrid nanofillers, *Compos Part B-Eng*, 2022, **245**, 110236.
  154. J. Liu, Z. Wang, Q. Liu, S. R. Li, D. C. Wang and Z. F. Zheng, Rational design of freestanding and high-performance thick electrode from carbon foam modified with polypyrrole/polydopamine for supercapacitors, *Chem Eng J*, 2022, **447**, 137562.
  155. J. El Nady, A. Shokry, M. Khalil, S. Ebrahim, A. M. Elshaer and M. Anas, One-step electrodeposition of a polypyrrole/NiO nanocomposite as a supercapacitor electrode, *Sci Rep*, 2022, **12**, 3611.

156. A. L. Chen, C. Y. Wang, O. A. A. Ali, S. F. Mahmoud, Y. T. Shi, Y. X. Ji, H. Algadi, S. M. El-Bahy, M. A. Huang, Z. H. Guo, D. P. Cui and H. G. Wei, MXene@nitrogen-doped carbon films for supercapacitor and piezoresistive sensing applications, *Compos Part A-Appl S*, 2022, **163**, 107174.
157. S. Normohammadi, F. Bahmani, L. Fotouhi and M. Khoshfetrat, Electrodeposited nickel nanocone/NiMoO<sub>4</sub> nanocomposite designed as superior electrode materials for high performance supercapacitor, *Int J Hydrogen Energ*, 2022, **47**, 5220-5229.
158. M. Y. Lian, J. X. Sun, D. W. Jiang, M. J. Xu, Z. J. Wu, B. B. Xu, H. Algadi, M. N. Huang and Z. H. Guo, Waterwheel-inspired high-performance hybrid electromagnetic-triboelectric nanogenerators based on fluid pipeline energy harvesting for power supply systems and data monitoring, *Nanotechnology*, 2023, **34**, 025401.
159. S. L. Gao, X. H. Zhao, Q. Fu, T. C. Zhang, J. Zhu, F. H. Hou, J. Ni, C. J. Zhu, T. T. Li, Y. L. Wang, V. Murugadoss, G. A. M. Mersal, M. M. Ibrahim, Z. M. El-Bahy, M. N. Huang and Z. H. Guo, Highly transmitted silver nanowires-SWCNTs conductive flexible film by nested density structure and aluminum-doped zinc oxide capping layer for flexible amorphous silicon solar cells, *J Mater Sci Technol*, 2022, **126**, 152-160.
160. E. Samuel, A. Aldalbahi, M. El-Newehy, H. El-Hamshary and S. S. Yoon, Flexible and freestanding manganese/iron oxide carbon nanofibers for supercapacitor electrodes, *Ceram Int*, 2022, **48**, 18374-18383.
161. X. Huang, R. Sun, Y. Li, J. Jiang, W. X. Mingjing Li, Yunyun Wang, and J. T. Haishan Cong, Sheng Han, Two-step electrodeposition synthesis of heterogeneous NiCo-layered double

- hydroxides@MoO<sub>3</sub> nanocomposites on nickel foam with high performance for hybrid supercapacitors, *Electrochim Acta*, 2022, **403**, 139680.
162. H. B. Zhang, Y. Lv, X. Y. Wu, J. X. Guo and D. Z. Jia, Electrodeposition synthesis of high performance MoO<sub>3-x</sub>@Ni-Co layered double hydroxide hierarchical nanorod arrays for flexible solid-state supercapacitors, *Chem Eng J*, 2022, **431**, 133233.
  163. K. M. Amin, K. Krois, F. Muench, B. J. M. Etzold and W. Ensinger, Hierarchical pipe cactus-like Ni/NiCo-LDH core-shell nanotube networks as a self-supported battery-type electrode for supercapacitors with high volumetric energy density, *J Mater Chem A*, 2022, **10**, 12473-12488.
  164. N. Zhao, Y. Feng, H. Zhao, H. Fan, S. Tian and B. Hu, Simple electrodeposition of 3D NiCoFe-layered double hydroxide nanosheet assembled nanospheres/nanoflowers on carbon cloth for high performance hybrid supercapacitors, *J Alloy Compd*, 2022, **901**, 163566.
  165. L. Wang and X. Chen, NiCo layered double hydroxide on three-dimensional modified graphite paper for high-performance supercapacitors, *J Alloy Compd*, 2022, **907**, 164411.
  166. T. Wang, K. Liu, Z. Gao, Z. Zeng, R. Mao, G. Zhu, J. Ni, X. Xu, R. Jia and S. Han, Oxygen vacancy-rich flower-like nickel cobalt layered double hydroxides for supercapacitors with ultrahigh capacity, *Ceram Int*, 2022, **48**, 19798-19805.
  167. Y. Wang, Z. Wang, X. Zheng, X. Teng, L. Xu, Y. Yuan, X. Liu, A. Fu, Y. Li and H. Li, Core-sheath heterostructure of MnCo<sub>2</sub>O<sub>4</sub> nanowires wrapped by NiCo-layered double hydroxide as cathode material for high-performance quasi-solid-state asymmetric supercapacitors, *J Alloy Compd*, 2022, **904**, 164047.

168. L. Wan, L. Chen, M. Xie, J. Chen, Y. Zhang and C. Du, Hierarchical FeCoSe<sub>2</sub>@NiCo-layered double hydroxide nanosheet arrays with boosted performance for hybrid supercapacitors, *J Alloy Compd*, 2022, **901**, 163567.
169. S. Ban, J. Xie, Y. J. Wang, B. Jing, B. Liu and H. J. Zhou, Insight into the Nanoscale Mechanism of Rapid H<sub>2</sub>O Transport within a Graphene Oxide Membrane: Impact of Oxygen Functional Group Clustering, *ACS Appl Mater Inter*, 2016, **8**, 321-332.
170. Y. L. Zhang, K. P. Ruan and J. W. Gu, Flexible Sandwich-Structured Electromagnetic Interference Shielding Nanocomposite Films with Excellent Thermal Conductivities, *Small*, 2021, **17**, 2101951.
171. B. Kirubasankar, M. Narayanasamy, J. Yang, M. Y. Han, W. H. Zhu, Y. J. Su, S. Angaiah and C. Yan, Construction of heterogeneous 2D layered MoS<sub>2</sub>/MXene nanohybrid anode material via interstratification process and its synergetic effect for asymmetric supercapacitors, *Appl Surf Sci*, 2020, **534**, 147644.
172. F. Q. Qi, L. Wang, Y. L. Zhang, Z. L. Ma, H. Qiu and J. W. Gu, Robust Ti<sub>3</sub>C<sub>2</sub>T<sub>x</sub> MXene/starch derived carbon foam composites for superior EMI shielding and thermal insulation, *Mater Today Phys*, 2021, **21**, 100512.
173. C. B. Liang, H. Qiu, P. Song, X. T. Shi, J. Kong and J. W. Gu, Ultra-light MXene aerogel/wood-derived porous carbon composites with wall-like "mortar/brick" structures for electromagnetic interference shielding, *Sci Bull*, 2020, **65**, 616-622.
174. L. Wang, L. X. Chen, P. Song, C. B. Liang, Y. J. Lu, H. Qiu, Y. L. Zhang, J. Kong and J. W. Gu, Fabrication on the annealed Ti<sub>3</sub>C<sub>2</sub>T<sub>x</sub> MXene/Epoxy nanocomposites for electromagnetic

- interference shielding application, *Compos Part B-Eng*, 2019, **171**, 111-118.
175. B. Dai, Y. Ma, F. Dong, J. Yu, M. Ma, H. K. Thabet, S. M. El-Bahy, M. M. Ibrahim, M. Huang, I. Seok, G. Roymahapatra, N. Naik, B. B. Xu, J. Ding and T. Li, Overview of MXene and conducting polymer matrix composites for electromagnetic wave absorption, *Adv Compos Hybrid Ma*, 2022, **5**, 704-754.
  176. W. Luo, Y. Ma, T. Li, H. K. Thabet, C. Hou, M. M. Ibrahim, S. M. El-Bahy, B. B. Xu and Z. Guo, Overview of MXene/conducting polymer composites for supercapacitors, *J Energy Storage*, 2022, **52**, 105008.
  177. Y. L. Zhang, Y. Yan, H. Qiu, Z. L. Ma, K. P. Ruan and J. W. Gu, A mini-review of MXene porous films: Preparation, mechanism and application, *J Mater Sci Technol*, 2022, **103**, 42-49.
  178. P. Song, B. Liu, C. B. Liang, K. P. Ruan, H. Qiu, Z. L. Ma, Y. Q. Guo and J. W. Gu, Lightweight, Flexible Cellulose-Derived Carbon Aerogel@Reduced Graphene Oxide/PDMS Composites with Outstanding EMI Shielding Performances and Excellent Thermal Conductivities, *Nano-Micro Lett*, 2021, **13**, 91.
  179. C. B. Liang, H. Qiu, Y. Y. Han, H. B. Gu, P. Song, L. Wang, J. Kong, D. P. Cao and J. W. Gu, Superior electromagnetic interference shielding 3D graphene nanoplatelets/reduced graphene oxide foam/epoxy nanocomposites with high thermal conductivity, *J Mater Chem C*, 2019, **7**, 2725-2733.
  180. Z. Zhao, X. Wu, C. Luo, Y. Wang and W. Chen, Rational design of  $\text{Ti}_3\text{C}_2\text{Cl}_2$  MXenes nanodots-interspersed MXene@NiAl-layered double hydroxides for enhanced pseudocapacitor storage, *J Colloid Interface Sci*, 2022, **609**, 393-402.



181. X. Wu, B. Huang, Q. Wang and Y. Wang, High energy density of two-dimensional MXene/NiCo-LDHs interstratification assembly electrode: Understanding the role of interlayer ions and hydration, *Chem Eng J*, 2020, **380**, 122456.
182. N. S. Padalkar, S. V. Sadavar, R. B. Shinde, A. S. Patil, U. M. Patil, D. S. Dhawale, R. N. Bulakhe, H. Kim, H. Im, A. Vinu, C. D. Lokhande and J. L. Gunjekar, Layer-by-layer nanohybrids of Ni-Cr-LDH intercalated with 0D polyoxotungstate for highly efficient hybrid supercapacitor, *J Colloid Interface Sci*, 2022, **616**, 548-559.
183. X. Wang, F. Wu, J. Fan, A. Tian, Y. Cheng and S. Yang, High specific surface area NiTiAl layered double hydroxide derived via alkali etching for high performance supercapacitor electrode, *J Alloy Compd*, 2021, **888**, 161502.
184. M. Wang, Y. Feng, Y. Zhang, S. Li, M. Wu, L. Xue, J. Zhao, W. Zhang, M. Ge, Y. Lai and J. Mi, Ion regulation of hollow nickel cobalt layered double hydroxide nanocages derived from ZIF-67 for High-Performance supercapacitors, *Appl Surf Sci*, 2022, **596**, 153582.
185. X. Chu, F. Meng, H. Yang, W. Zhang, T. Qin, Z. Wang, S. Molin, P. Jasinski and W. Zheng, Cu-Doped Layered Double Hydroxide Constructs the Performance-Enhanced Supercapacitor Via Band Gap Reduction and Defect Triggering, *ACS Appl Energ Mater*, 2022, **5**, 2192-2201.
186. M. Xu, Y. Huang, R. Chen, Q. Huang, Y. Yang, L. Zhong, J. Ren and X. Wang, Green conversion of Ganoderma lucidum residues to electrode materials for supercapacitors, *Adv Compos Hybrid Ma*, 2021, **4**, 1270-1280.
187. F. Liu, Y. Zhao, H. Hou, Y. Zhao, Z. Wang and Z. Huang, Synthesis of silicon-based nanosheets

- decorated with Pd/Li particles with enhanced hydrogen storage properties, *Adv Compos Hybrid Ma*, 2021, **4**, 1343-1353.
188. M. Pathak and C. S. Rout, Hierarchical NiCo<sub>2</sub>S<sub>4</sub> nanostructures anchored on nanocarbons and Ti<sub>3</sub>C<sub>2</sub>T<sub>x</sub> MXene for high-performance flexible solid-state asymmetric supercapacitors, *Adv Compos Hybrid Ma*, 2022, **5**, 1404-1422.
  189. Z. Sun, K. Qu, J. Li, S. Yang, B. Yuan, Z. Huang and Z. Guo, Self-template biomass-derived nitrogen and oxygen co-doped porous carbon for symmetrical supercapacitor and dye adsorption, *Adv Compos Hybrid Ma*, 2021, **4**, 1413-1424.
  190. Y. H. Zhao, K. X. Liu, H. Hou and L. Q. Chen, Role of interfacial energy anisotropy in dendrite orientation in Al-Zn alloys: A phase field study, *Mater Design*, 2022, **216**, 110555.
  191. T. Z. Xin, S. Tang, F. Ji, L. Q. Cui, B. B. He, X. Lin, X. L. Tian, H. Hou, Y. H. Zhao and M. Ferry, Phase transformations in an ultralight BCC Mg alloy during anisothermal ageing, *Acta Mater*, 2022, **239**, 118248.
  192. J. C. Cai, V. Murugadoss, J. Y. Jiang, X. Gao, Z. P. Lin, M. A. Huang, J. Guo, S. A. Alsareii, H. Algadi and M. Kathiresan, Waterborne polyurethane and its nanocomposites: a mini-review for anti-corrosion coating, flame retardancy, and biomedical applications, *Adv Compos Hybrid Ma*, 2022, **5**, 641-650.
  193. Y. Lian, Y. Zheng, D. Wang, Y. Bai, H. Yan, Z. Wang, J. Zhao and H. Zhang, Ultrafast and stable ion/electron transport of MnNb<sub>2</sub>O<sub>6</sub> in LIC/SC via interface protection and lattice defects, *J Colloid Interf Sci*, 2022, **606**, 77-86.

194. S. L. Huo, W. Ni, X. Song, M. T. Zhang, H. Wang and K. X. Li, Insight from the synergistic effect of dopant and defect interplay in carbons for high-performance capacitive deionization, *Sep Purif Technol*, 2022, **281**, 119807.
195. G. S. S. Mamaril, M. D. G. de Luna, K. Bindumadhavan, D. C. Ong, J. A. I. Pimentel and R. A. Doong, Nitrogen and fluorine co-doped 3-dimensional reduced graphene oxide architectures as high-performance electrode material for capacitive deionization of copper ions, *Sep Purif Technol*, 2021, **272**, 117559.
196. Y. F. Zhang, J. J. Zheng, J. J. Nan, C. J. Gai, Q. Shao, V. Murugadoss, S. Maganti, N. Naik, H. Algadi, M. A. Huang, B. B. Xu and Z. H. Guo, Influence of mass ratio and calcination temperature on physical and photoelectrochemical properties of ZnFe-layered double oxide/cobalt oxide heterojunction semiconductor for dye degradation applications, *Particuology*, 2023, **74**, 141-155.
197. D. Pan, G. Yang, H. M. Abo-Dief, J. W. Dong, F. M. Su, C. T. Liu, Y. F. Li, B. B. Xu, V. Murugadoss, N. Naik, S. M. El-Bahy, Z. M. El-Bahy, M. A. Huang and Z. H. Guo, Vertically Aligned Silicon Carbide Nanowires/ Boron Nitride Cellulose Aerogel Networks Enhanced Thermal Conductivity and Electromagnetic Absorbing of Epoxy Composites, *Nano-Micro Lett*, 2022, **14**, 118.
198. Y. Feng, Y. C. Li, X. M. Ye, Z. M. Li, W. S. Wang, T. Liu, I. H. El Azab, G. A. M. Mersal, M. M. Ibrahim, Z. M. El-Bahy, M. N. Huang and Z. H. Guo, Synthesis and characterization of 2,5-furandicarboxylic acid poly(butanediol sebacate-butanediol) terephthalate (PBSeT) segment copolyesters with excellent water vapor barrier and good mechanical properties, *J Mater Sci*, 2022, **57**, 10997-11012.

199. L. Suryanti, S. E. I. Suryani, Hartatiek, Nasikhudin, J. Utomo, A. Taufiq, R. Suryana, Z. Aspanut and M. Diantoro, The effect of  $\text{Mn}_2\text{O}_3$  nanoparticles on its specific capacitance of symmetric supercapacitors FC-ZnO-x( $\text{Mn}_2\text{O}_3$ ), *7th International Conference of Advanced Materials Science and Technology (ICAMST)*, 2019, **44**, 3355-3360.
200. E. Taer, A. Putri, R. Farma, Awitdrus, R. Taslim, Apriwandi, Agustino and D. A. Yusra, The effect of potassium iodide (KI) addition to aqueous-based electrolyte (sulfuric acid/ $\text{H}_2\text{SO}_4$ ) for increase the performance of supercapacitor cells, *7th International Conference of Advanced Materials Science and Technology (ICAMST)*, 2019, **44**, 3241-3244.
201. Y. Zhao, F. Liu, Z. Zhao, P. Bai, Y. Ma, A. Alhadhrami, G. A. M. Mersal, Z. Lin, M. M. Ibrahim and Z. M. El-Bahy, Direct ink printing reduced graphene oxide/ $\text{KCu}_7\text{S}_4$  electrodes for high-performance supercapacitors, *Adv Compos Hybrid Ma*, 2022, **5**, 1516-1526.
202. Y. Zhao, F. Liu, K. Zhu, S. Maganti, Z. Zhao and P. Bai, Three-dimensional printing of the copper sulfate hybrid composites for supercapacitor electrodes with ultra-high areal and volumetric capacitances, *Adv Compos Hybrid Ma*, 2022, **5**, 1537-1547.
203. R. Xue, H. Guo, W. Yang, S.-L. Huang and G.-Y. Yang, Cooperation between covalent organic frameworks (COFs) and metal organic frameworks (MOFs): application of COFs-MOFs hybrids, *Adv Compos Hybrid Ma*, 2022, **5**, 1595-1611.
204. M. Lian, Y. Huang, Y. Liu, D. Jiang, Z. Wu, B. Li, Q. Xu, V. Murugadoss, Q. Jiang, M. Huang and Z. Guo, An overview of regenerable wood-based composites: preparation and applications for flame retardancy, enhanced mechanical properties, biomimicry, and transparency energy saving, *Adv*

- Compos Hybrid Ma*, 2022, **5**, 1612-1657.
205. Q. Ma, X. Han, J. Cui, Y. Zhang and W. He, Ni embedded carbon nanofibers/ Ni-Al LDHs with multicomponent synergy for hybrid supercapacitor electrodes, *Colloid Surface A*, 2022, **649**, 129270.
  206. H. Lv, H. Rao, Z. Liu, Z. Zhou, Y. Zhao, H. Wei and Z. Chen, NiAl layered double hydroxides with enhanced interlayer spacing via ion-exchange as ultra-high performance supercapacitors electrode materials, *J Energy Storage*, 2022, **52**, 104940.
  207. H. Deng, T. Liu, W. Liao and D. Yang, Double metal ions synergistic effect in the Ni-doped Co(OH)(BA) nanobelts for enhanced supercapacitor performance, *J Phys Chem Solids*, 2022, **164**, 110641.
  208. O. Saber, S. A. Ansari, A. Osama and M. Osama, One-Dimensional Nanoscale Si/Co Based on Layered Double Hydroxides towards Electrochemical Supercapacitor Electrodes, *Nanomaterials-Basel*, 2022, **12**, 1404.
  209. A. Mahmood, B. Zhao, M. S. Javed, D. He, W. C. Cheong, D. Han and L. Niu, Unprecedented Dual Role of Polyaniline for Enhanced Pseudocapacitance of Cobalt-Iron Layered Double Hydroxide, *Macromol Rapid Commun*, 2022, **43**, e2100905.
  210. X. Y. Deng, H. Y. Qin, X. Y. Liu, S. Zhu, J. J. Li, L. Y. Ma and N. Q. Zhao, Hierarchically porous trimetallic hydroxide arrays for aqueous energy storage and oxygen evolution with enhanced redox kinetics, *J Alloy Compd*, 2022, **918**, 165650.
  211. X.-A. Liu, J. Wang, D. Tang, Z. Tong, H. Ji and H.-Y. Qu, A forest geotexture-inspired ZnO@Ni/Co layered double hydroxide-based device with superior electrochromic and energy storage

- performance, *J Mater Chem A*, 2022, **10**, 12643-12655.
212. G. Zhou, X. Gao, S. Wen, X. Wu, L. Zhang, T. Wang, P. Zhao, J. Yin and W. Zhu, Magnesium-regulated oxygen vacancies of cobalt-nickel layered double hydroxide nanosheets for ultrahigh performance asymmetric supercapacitors, *J Colloid Interface Sci*, 2022, **612**, 772-781.
  213. X. Wang, Y. Cheng, X. Qiao, D. Zhang, Y. Xia, J. Fan, C. Huang and S. Yang, High-loading and high-performance NiMn layered double hydroxide nanosheets supported on nickel foam for supercapacitor via sodium dodecyl sulfonate intercalation, *J Energy Storage*, 2022, **52**, 104834.
  214. Z. Li, M. Yao, Z. Hu, L. Zhang, S. Gou, H. Feng, Y. Yang and X. Lu, g-C<sub>3</sub>N<sub>4</sub> promoted NiFe-LDH self-assemble high performance supercapacitor composites, *J Alloy Compd*, 2022, **919**, 165805.
  215. H. Wu, X. Zhang, J. Xue, H. Zhang, L. Yang and S. Li, Engineering active sites on hierarchical ZnNi layered double hydroxide architectures with rich Zn vacancies boosting battery-type supercapacitor performances, *Electrochim Acta*, 2021, **374**, 137932.
  216. G. Lei, D. Chen, Q. Li, H. Liu, Q. Shi and C. Li, NiCo-layered double hydroxide with cation vacancy defects for high-performance supercapacitors, *Electrochim Acta*, 2022, **413**, 140143.
  217. Y. Caihong, B. Zhang, X. Xie, C. Li, Y. Xu, H. Wang and L. Wang, Three-dimensional independent CoZnAl-LDH nanosheets via asymmetric etching of Zn/Al dual ions for high-performance supercapacitors, *J Alloy Compd*, 2021, **861**, 157933.
  218. L. Zhong, Z. Yan, H. Wang and L. Wang, Hydrazine Hydrate Induced Three-Dimensional Interconnected Porous Flower-like 3D-NiCo-SDBS-LDH Microspheres for High-Performance Supercapacitor, *Materials*, 2022, **15**, 1405.

219. J. B. Kim, S. H. Koo, I. H. Kim, J. T. Kim, J. G. Kim, B. Jayaraman, J. Lim and S. O. Kim, Characteristic dual-domain composite structure of reduced graphene oxide and its application to higher specific capacitance, *Chem Eng J*, 2022, **446**, 137390.
220. J. J. Ban, X. H. Wen, H. H. Lei, G. Q. Cao, X. H. Liu, C. Y. Niu, G. S. Shao and J. H. Hu, In-plane grain boundary induced defect state in hierarchical NiCo-LDH and effect on battery-type charge storage, *Nano Res*, 2022, DOI: <https://doi.org/10.1007/s12274-022-4485-1>.
221. N. Kim, T. H. Gu, D. Shin, X. Jin, H. Shin, M. G. Kim, H. Kim and S. J. Hwang, Lattice Engineering to Simultaneously Control the Defect/Stacking Structures of Layered Double Hydroxide Nanosheets to Optimize Their Energy Functionalities, *ACS Nano*, 2021, **15**, 8306-8318.
222. H. Zhang, Y. Bai, H. Chen, J. Wu, C. M. Li, X. Su and L. Zhang, Oxygen-defect-rich 3D porous cobalt-gallium layered double hydroxide for high-performance supercapacitor application, *J Colloid Interface Sci*, 2022, **608**, 1837-1845.
223. S. V. Sadavar, N. S. Padalkar, R. B. Shinde, A. S. Patil, U. M. Patil, V. V. Magdum, Y. M. Chitare, S. P. Kulkarni, S. B. Kale, R. N. Bulakhe, D. S. Bhange, S. T. Kochuveedu and J. L. Gunjekar, Lattice engineering exfoliation-restacking route for 2D layered double hydroxide hybridized with 0D polyoxotungstate anions: Cathode for hybrid asymmetric supercapacitors, *Energy Storage Mater*, 2022, **48**, 101-113.
224. S. D. D. Raut, N. M. M. Shinde, B. G. G. Ghule, S. Kim, J. J. J. Pak, Q. X. Xia and R. S. S. Mane, Room-temperature solution-processed sharp-edged nanoshapes of molybdenum oxide for supercapacitor and electrocatalysis applications, *Chem Eng J*, 2022, **433**, 133627.



225. C. Ding, N. Zhu, X. Wang, A. Alhadhrami, M. H. H. Mahmoud, M. M. Ibrahim, Q. Huang, C. Liu, M. Huang and J. Wang, Experimental study on the burning behaviors of 21700 lithium-ion batteries with high specific energy after different immersion duration, *Adv Compos Hybrid Ma*, 2022, **5**, 2575-2588.
226. J. Z. Feng, X. Q. Zhang, Y. T. Xu, H. Y. Ma, Y. Xue, L. J. Su, J. W. Lang, Y. Tang, S. R. Yang and X. B. Yan, Regulating the electrolyte ion types and exposed crystal facets for pseudocapacitive energy storage of transition metal nitrides, *Energy Storage Mater*, 2022, **46**, 278-288.
227. A. Helal, S. S. Shah, M. Usman, M. Y. Khan, M. A. Aziz and M. M. Rahman, Potential Applications of Nickel-Based Metal-Organic Frameworks and their Derivatives, *Chem Rec*, 2022, **22**, e202200055.
228. D. Luo, Y. Yong, J. Hou, W. Guo, H. Liu, X. Zhao, J. Xiang, N. ZongZong, Y. Han and M. Yan, Construction of Hierarchical  $\text{NiCo}_2\text{O}_4@\text{NiFe-LDH}$  Core - Shell Heterostructure for High - performance Positive Electrode for Supercapacitor, *Chemnanomat*, 2022, **8**, e202200086.
229. H. Kuang, H. Zhang, X. Liu, Y. Chen, W. Zhang, H. Chen and Q. Ling, Microwave-assisted synthesis of NiCo-LDH/graphene nanoscrolls composite for supercapacitor, *Carbon*, 2022, **190**, 57-67.
230. Q. Ma, S. Wang, X. Han, J. Cui, G. Jia, Y. Zhang and W. He, Construction of three-dimensional (3D) vertical nanosheets electrode with electrochemical capacity applied to microsupercapattery, *Vacuum*, 2022, **198**, 110914.
231. P. Zhang, X. Deng, W. Li, Z. Ma and X. Wang, Electrochemical-induced surface reconstruction to

- NiFe-LDHs-based heterostructure as novel positive electrode for supercapacitors with enhanced performance in neutral electrolyte, *Chem Eng J*, 2022, **449**, 137886.
232. L. Luo, Y. L. Zhou, W. Yan, G. B. Du, M. Z. Fan and W. G. Zhao, Construction of advanced zeolitic imidazolate framework derived cobalt sulfide/MXene composites as high-performance electrodes for supercapacitors, *J Colloid Interf Sci*, 2022, **615**, 282-292.
  233. A. G. El-Deen, M. K. Abdel-Sattar and N. K. Allam, High-performance solid-state supercapacitor based on Ni-Co layered double hydroxide@Co<sub>3</sub>O<sub>4</sub> nanocubes and spongy graphene electrodes, *Appl Surf Sci*, 2022, **587**, 152548.
  234. L. Liao, K. Zheng, Y. Zhang, X. Li, D. Jiang and J. Liu, Self-templated pseudomorphic transformation of ZIF into layered double hydroxides for improved supercapacitive performance, *J Colloid Interface Sci*, 2022, **622**, 309-318.
  235. M. Chen, J. Chen, X. Tan, W. Yang, H. Zou and S. Chen, Facile self-assembly of sandwich-like MXene/graphene oxide/nickel-manganese layered double hydroxide nanocomposite for high performance supercapacitor, *J Energy Storage*, 2021, **44**, 103456.
  236. X. Zhu, X. Li, H. Tao and M. Li, Preparation of Co<sub>2</sub>Al layered double hydroxide nanosheet/Co<sub>2</sub>Mn bimetallic hydroxide nanoneedle nanocomposites on nickel foam for supercapacitors, *J Alloy Compd*, 2021, **851**, 156868.
  237. Z. Ma, L. Fan, F. Jing, J. Zhao, Z. Liu, Q. Li, J. Li, Y. Fan, H. Dong, X. Qin and G. Shao, MnO<sub>2</sub> Nanowires@NiCo-LDH Nanosheet Core-Shell Heterostructure: A Slow Irreversible Transition of Hydrotalcite Phase for High-Performance Pseudocapacitance Electrode, *ACS Appl Energ Mater*,

- 2021, **4**, 3983-3992.
238. X. Chen, M. He, Y. Zhou, G. He, C. Meng, Q. Cheng and F. Li, Design of hierarchical double-layer NiCo/NiMn-layered double hydroxide nanosheet arrays on Ni foam as electrodes for supercapacitors, *Mater Today Chem*, 2021, **21**, 100507.
  239. H. Xiong, L. Liu, L. Fang, F. Wu, S. Zhang, H. Luo, C. Tong, B. Hu and M. Zhou, 3D self-supporting heterostructure NiCo-LDH/ZnO/CC electrode for flexible high-performance supercapacitor, *J Alloy Compd*, 2021, **857**, 158275.
  240. Z. Zhou, J. Tie, H. Yang, G. Cheng, M. Sun and L. Yu, 3D hierarchical NiCo<sub>2</sub>S<sub>4</sub>/Ni-Co LDH architecture for high-performance supercapacitor, *J Mater Sci-Mater El*, 2021, **32**, 3843-3853.
  241. H. Wang, T. Shu, C. X. Lin, F. Sun, Z. Y. Wang, B. Lin, F. X. Wei, K. X. Yao, J. Q. Qi and Y. W. Sui, Hierarchical construction of Co<sub>3</sub>S<sub>4</sub> nanosheet coated by 2D multi-layer MoS<sub>2</sub> as an electrode for high performance supercapacitor, *Appl Surf Sci*, 2022, **578**, 151897.
  242. Y. Q. Guo, H. Qiu, K. P. Ruan, S. S. Wang, Y. L. Zhang and J. W. Gu, Flexible and insulating silicone rubber composites with sandwich structure for thermal management and electromagnetic interference shielding, *Compos Sci Technol*, 2022, **219**, 109253.
  243. Q. S. Zhu, Y. Zhao, B. J. Miao, H. M. Abo-Dief, M. C. Qu, R. A. Pashameah, B. Bin Xu, M. A. Huang, H. Algadi, X. H. Liu and Z. H. Guo, Hydrothermally synthesized ZnO-RGO-PPy for water-borne epoxy nanocomposite coating with anticorrosive reinforcement, *Prog Org Coat*, 2022, **172**, 107153.
  244. D. Kumar, A. Joshi, G. Singh and R. K. Sharma, Polyoxometalate/ZIF-67 composite with exposed

- active sites as aqueous supercapacitor electrode, *Chem Eng J*, 2022, **431**, 134085.
245. K. Li, Z. Hu, R. Zhao, J. Zhou, C. Jing, Q. Sun, J. Rao, K. Yao, B. Dong, X. Liu, H. Li, Y. Zhang and J. Ji, A multidimensional rational design of nickel-iron sulfide and carbon nanotubes on diatomite via synergistic modulation strategy for supercapacitors, *J Colloid Interface Sci*, 2021, **603**, 799-809.
246. A. Rajapriya, S. Keerthana, C. Viswanathan and N. Ponpandian, Three dimensional integrated architecture of Sr Fe LDH on hierarchical NiS framework as a flexible electrode for efficient energy storage and conversion applications, *J Energy Storage*, 2022, **53**, 105091.
247. P. C. Lohani, A. P. Tiwari, K. Chhetri, A. Muthurasu, B. Dahal, S. H. Chae, T. H. Ko, J. Y. Lee, Y. S. Chung and H. Y. Kim, Polypyrrole Nanotunnels with Luminal and Abluminal Layered Double Hydroxide Nanosheets Grown on a Carbon Cloth for Energy Storage Applications, *ACS Appl Mater Interfaces*, 2022, **14**, 23285-23296.
248. Z. H. Wang, Z. Q. Liu, L. Wang, K. Zhao, X. L. Sun, D. D. Jia and J. Q. Liu, Construction of Core-Shell Heterostructured Nanoarrays of Cu(OH)(2)@NiFe-Layered Double Hydroxide through Facile Potentiostatic Electrodeposition for Highly Efficient Supercapacitors, *Chemelectrochem*, 2022, **9**, e202101711.
249. W. Cao, C. Xiong, Y. Liu, F. Xu, W. Zhao, Q. Xia, G. Du and N. Chen, Novel fabrication strategy of nanostructured NiCo-LDHs monolithic supercapacitor electrodes via inducing electrochemical in situ growth on etched nickel foams, *J Alloy Compd*, 2022, **902**, 163679.
250. A. Emin, X. Song, Y. Du, Y. Chen, M. Yang, S. Zou, Y. Fu, J. Li, Y. Li and D. He, One-step

- electrodeposited Co and Mn layered double hydroxides on Ni foam for high-performance aqueous asymmetric supercapacitors, *J Energy Storage*, 2022, **50**, 104667.
251. Y. Lu, J. Guo, Z. He, Z. Gao and Y.-Y. Song, Direct access to NiCo-LDH nanosheets by electrochemical-scanning-mediated hydrolysis for photothermally enhanced energy storage capacity, *Energy Storage Mater*, 2022, **48**, 487-496.
  252. J. Wang, M. Li, Y. Zhai, F. Wang, X. Zhang, H. Lv, T. Yu and W. Zhang, Construction of three-dimensional nanocube-on-sheet arrays electrode derived from Prussian blue analogue with high electrochemical performance, *Appl Surf Sci*, 2021, **556**, 149789.
  253. H. Li, S. Lin, H. Li, Z. Wu, Q. Chen, L. Zhu, C. Li, X. Zhu and Y. Sun, Magneto-Electrodeposition of 3D Cross-Linked NiCo-LDH for Flexible High-Performance Supercapacitors, *Small Methods*, 2022, **6**, e2101320.
  254. G. Nagaraju, S. Chandra Sekhar, L. Krishna Bharat and J. S. Yu, Wearable Fabrics with Self-Branched Bimetallic Layered Double Hydroxide Coaxial Nanostructures for Hybrid Supercapacitors, *ACS Nano*, 2017, **11**, 10860-10874.
  255. Z. Liu, H. Zhou, F. Zeng, L. Hu, X. Wu, X. Song, C. Jiang and X. Zhang, All-Printed High-Performance Flexible Supercapacitors Using Hierarchical Porous Nickel-Cobalt Hydroxide Inks, *ACS Appl Energ Mater*, 2022, **5**, 9418-9428.